THÈSE DE DOCTORAT
DE L'UNIVERSITÉ DE LILLE

LABORATOIRE DE MÉCANIQUE, MULTIPHYSIQUE ET MULTIECHELLE (UMR9013, CNRS)

Présentée par

Liping ZHU

pour obtenir le grade de

DOCTEUR DE L'UNIVERSITÉ DE LILLE

Domaine

GÉNIE CIVIL

Sujet de la thèse

Utilisation de la simulation moléculaire pour mieux évaluer la déformation et la rupture des roches riches en argile

(Application of molecular dynamics simulation to better assess deformation and failure processes of clay-rich rocks)

Soutenue le 08 Décembre 2021 devant le jury composé de :

Mr. Djimédo KONDO, Professeur	Sorbonne Université	*president du jury*
Mme. Béatrice LEDESERT, Professeur	CY Cergy Paris Université	*Rapporteur*
Mr. Quy-Dong TO, Professeur	Université Gustave EIFFEL	*Rapporteur*
Mr. Minh-Ngoc VU, Docteur	ANDRA	*Examinateur*
Mr. Jianfu SHAO, Professeur	Université de Lille	*Examinateur*
Mr. Wanqing SHEN, MCF-HDR	Université de Lille	*Directeur de thèse*

LAMCUBE - ED - UNIVERSITÉ DE LILLE

Abstract

Understanding the mechanical characteristics of clay-based materials is critical in earth sciences and a variety of industrial applications. Clay, as the main component in these heterogeneous materials, plays a significant role in the mechanical behavior of such materials. Through the Molecular Dynamics (MD) simulation, the present thesis is devoted to investigating the mechanical behaviors of swelling clay minerals at atomic scale by putting the emphasis on the influences of water content, loading path, crystal structure anisotropy and mean stress. The thesis is composed of three parts.

The first part mainly focuses on the mechanical properties of dry Na-montmorillonite (MMT) which is subjected to triaxial compression and extension loading with different constant mean stresses. A series of Molecular Dynamics (MD) simulations have been carried out respectively in the parallel and perpendicular directions to crystal layers. The effects of loading path, mean stress and anisotropy on mechanical properties of dry MMT at atomic scale are fully studied and discussed.

The second part investigates the influences of water content on the physical and mechanical properties under triaxial compression with a constant mean stress. At first, the swelling property is characterized by the relationship between inter-layer distance and the extent of hydration. Secondly, the stress-strain relationships are obtained for different water contents. In addition, the micro-structure and inter-layer connection of the dry, one-, two-, three-layer hydrated MMT systems between initial and failure states have been analyzed in-depth. At last, the key mechanisms triggering their failure at the atomic scale are identified and analyzed.

The third part is devoted to describing the creep deformation of MMT. Through the MD simulation, three representative creep stages have been clearly characterized. The effects of applied stress level, deviatoric stress, the temperature and microstructure orientation on the time dependent responses of MMT have been investigated.

Keywords: Clays, clayey rocks, mechanical behavior, creep, atomistic approaches, molecular dynamics

Résumé

La compréhension des caractéristiques mécaniques des matériaux à base d'argile est essentielle en sciences de la terre et dans diverses applications industrielles. L'argile, en tant que composant principal de ces matériaux hétérogènes, joue un rôle important dans le comportement mécanique de ces matériaux. A travers la simulation de la Dynamique Moléculaire (DM), la présente thèse est consacrée à l'étude des comportements mécaniques des minéraux argileux gonflants à l'échelle atomique en mettant l'accent sur les influences de la teneur en eau, du chemin de chargement, de l'anisotropie et de la contrainte moyenne. La thèse est composée de trois parties principales.

La première partie se concentre essentiellement sur les propriétés mécaniques de la Na-montmorillonite sèche (MMT) qui est soumise à un chargement triaxial de compression et d'extension avec différentes contraintes moyennes constantes. Une série de simulations de dynamique moléculaire a été réalisée respectivement dans les directions parallèle et perpendiculaire aux couches cristallines. Les effets de la trajectoire de chargement, de la contrainte moyenne et de l'anisotropie sur les propriétés mécaniques de la MMT sèche à l'échelle atomique sont étudiés et analysées en détail.

La deuxième partie étudie les influences de la teneur en eau sur les propriétés physiques et mécaniques sous compression triaxiale avec une contrainte moyenne constante. Dans un premier temps, la propriété de gonflement est caractérisée par la relation entre la distance inter-couches et le degré d'hydratation. Puis, la relation contrainte-déformation est obtenue. De plus, la microstructure et la connexion inter couche des systèmes MMT hydratés à une, deux ou trois couches entre l'état initial et l'état de défaillance ont été entièrement analysées. Enfin, les mécanismes essentiels déclenchant leur rupture à l'échelle atomique sont caractérisés et analysés.

La troisième partie est consacrée à la description des déformations de fluage de la MMT. Grâce à la simulation MD, les trois phases caractéristiques de fluage one été clairement identifiées. Les effets du niveau de contrainte appliqué, Tension de dérive, de la température et des orientations du chargement sur les réponses dépendantes du temps de la MMT ont été étudiés.

Mots clés: Argiles, roches argileuses, comportement mécanique, fluage, approches atomistiques, dynamique moléculaire

Ackonwledgements

Finally, when I start to write this part, it means I'm coming to the end of my doctoral career, look back at these three years, I have to exclaim that what an amazing time. Except for the wonderful memories during this period, my heart is filled with gratitude at this moment.

First of all, I am deeply grateful to my supervisor, Mr. Wanqing Shen who always tells me I am doing well when I do not believe in myself, help me to solve problems when I was in trouble. I am deeply impressed by his rigorous academic attitude and appreciatively for his patient guidance. Without his precious support and encouragement during this three years, this thesis would undoubtedly never have achieved fruition.

Secondly, I would like to express my most sincere gratitude to Professor Jianfu SHAO. During the past three years, I have felt the erudition and preciseness of scientific researchers and the wisdom and gentleness of elders from his patient guidance. He always works so hard and try his best to guide and help each student, he let me deeply realize that action is the most effective education. All in all, it is my great honor to be his student, what I have learned from him will benefit me all my life.

Thirdly, great thanks to all the members of the research group in LaMcube, they selflessly provide their help and support during my stay in France. The period of study and company with them is one of my best memories in the past, I will cherish this wonderful time. Wish everyone all the best.

Fourthly, I want to express my great thanks to my parents for their unconditional trust, encouragement and support when I was growing up. My father has three words benefit me a lot; reflect on yourself several times a day; be more self-critical. Right and wrong is a relative question. My mother is always kind to others. Their influence on me made me become a person who is optimistic, positive and capable of creating happiness.

Finally, I want to thank my husband, Yutian Ke. What can I say, it is so luckly to meet you in my beautiful age. It is unbelievable that we have almost the same cognition and ideas when we talk. You always say, stay true to why you started, this is your belief and so am I. Everything we've been through together has been a wonderful experience, I look forward to spending the rest of my life with you.

Liping ZHU

Contents

Contents i

General Introduction 1

I State of the Art 5

1 Introduction . . . 5

1.1 Mineralogy and micro-structure . . . 6

1.2 Motivation . . . 7

2 Basic mechanical behavior of clay-based materials . . . 8

2.1 Basic mechanical properties of claystone . . . 9

2.2 Thermal effects on the hydro-mechanical properties . . . 13

2.3 Influences of water content on the mechanical properties . . . 15

2.4 Loading path influences on the mechanical properties . . . 17

3 Principles of Molecular dynamics (MD) simulations . . . 20

3.1 Introduction . . . 20

3.2 Force field (the potential function for atoms interaction) . . . 21

3.3 Statistical Ensemble . . . 24

3.4 Integral algorithm for Newton equations of motion . . . 25

3.5 Boundary condition . . . 28

3.6 Advantage of molecular dynamics simulation . . . 29

4 Application of molecular dynamics simulation . . . 30

4.1 Atomic structure of montmorillonite . . . 31

4.2 Swelling property of clay minerals . . . 32

4.3 Interlayer structure of clay minerals . . . 33

4.4 Diffusion of interlayer cations and water . . . 34

4.5 Adsorption of clay minerals . . . 35

4.6 Elastic properties of clay minerals at microscale . . . 36

4.7 Deformation characteristics and failure mechanism of clay minerals . 38

II Assessment of deformation and failure of dry clay-rich rocks in compression and extension 43

1 Introduction . . . 43

2 Computational method . . . 46
2.1 Crystal structure . . . 46
2.2 Force filed . . . 47
2.3 MD simulation procedure . . . 50
3 Basic mechanical behavior and discussions . . . 51
3.1 Basic stress-strain response . . . 51
3.2 Effect of loading path . . . 53
3.3 Effect of loading orientation . . . 54
3.4 Effect of mean stress . . . 56
3.5 Effect of crystal model size . . . 59
3.6 Effect of temperature . . . 61
4 Further discussion on deformation and failure properties . . . 62
4.1 Analysis of failure stresses at atomistic scale . . . 62
4.2 Deformation and failure process at atomistic scale . . . 63
5 Conclusions . . . 67

III Effect of water content on mechanical property of claystone in compression 71

1 Introduction . . . 71
2 Models and methods . . . 74
2.1 Crystal structure . . . 74
2.2 Force filed . . . 76
2.3 MD simulation procedure . . . 77
3 Results and discussion . . . 78
3.1 Swelling property . . . 78
3.2 Stress-strain response of compression in z-axis . . . 79
3.3 Structural deformation characteristics . . . 80
3.4 Radial distribution function of cations . . . 83
3.5 Hydrogen bond network . . . 86
3.6 Energy evolution . . . 88
4 Conclusions . . . 92

IV Molecular dynamics study on creep deformation of montmorillonite 95

1 Introduction . . . 95
2 Computational method . . . 96
2.1 Crystal structure . . . 96

2.2 Force field 97
2.3 MD simulation procedure 98
3 Results and discussion 99
3.1 Conventional uniaxial and triaxial compression 99
3.2 Triaxial creep 100
3.3 Uniaxial creep 107
4 Conclusions 110

V Conclusions and Perspectives **113**
1 Conclusions 113
2 Perspectives 116

Bibliography **119**

General Introduction

Clayey rocks have been widely investigated in geological issues and engineering practices. For instance, the Callovo–Oxfordian (COx) claystone in Bure has been selected as the potential host rock for the deep underground radioactive waste disposal in France due to their low permeability and self-sealing ability as well as the absence of major fractures. Shale, a clay-rich sedimentary rock, is frequently encountered in petroleum engineering as a sealing formation of conventional reservoirs or in the inorganic phase of oil and gas shale rocks. Besides, swelling clay also works as an buffer backfill material together with the waste canister to constraint the radioactive wastes. Drilling through a shale layer, fracturing a shale to enhance its permeability and the long-term security requirement for the underground disposal of radioactive waste demand an comprehensive understanding of the strength and deformation characteristics of these materials. In addition, clayey rocks are always accompanied by complex underground environments, like underground water, heat generated by decay of radioactive waste resulting in an inevitable coupling mechanism between mechanical behavior and surroundings. Based on this, extensive mechanical tests corresponding to the disturb to host rock during construction and operation of repository, such as uniaxial and triaxial compression, triaxial extension and so on, have been widely performed for exploring the thermo-hydro-mechanical characteristics of such rocks in the close field (Armand et al., 2013; Bossart et al., 2017; Liu and Shao, 2016a; Menaceur et al., 2015; Tian et al., 2014; Yu et al., 2014; Zhang and Rothfuchs, 2004; Zhang, 2018).

Macroscopic mechanical behaviors of clayey rocks are controlled by the local mechanical properties of constituents and their interactions at the different scales. In particular, clay particles play a great role on macroscopic deformation and failure process of clayey rocks because clay forms the matrix and is softer with respect to the mineral inclusions in these heterogeneous materials. For instance, macroscopic plastic deformation is mainly driven by the local deformation mechanisms of clay particles and aggregates at the nanometer and micrometer scales (Bornert et al., 2010; Wang et al., 2015a). It is assumed that macroscopic time-dependent deformation of clayey rocks is also related to the local motion of clay particles (Armand et al., 2017; Liu et al., 2018c). Further, the macroscopic mechanical properties of clayey rocks are sensitive to its water content which almost owe to the strong water absorption and significant expansion upon hydration of swelling clay minerals. Meanwhile, the structure analysis at atomic scale have shown the clay particles are formed by the stacking of charged clay layers and the interlayer space between clay

layers are filled with cations and a variable amount of adsorbed water molecules which is the origin of sensitivity of mechanical properties to water content. In addition, the layered structure of clay crystals at the atomic scale can be one of the reasons for strongly anisotropic mechanical behaviors of clayey rocks (Liu et al., 2015b; Niandou et al., 1997). Therefore, the study on mechanical behaviors of clay particles at nanoscale is the critical route to deeply understand the motion of the atoms causing the deformation and failure of clayey rocks during loading. However, it is quite difficult to perform direct experimental measurement at such small scales in view of identifying those mechanisms. In this context, molecular dynamics simulations (MD) have been rapidly developed and widely used in modeling the clay-rich materials at atomic scales.

MD is firstly developed to focus on the structure distribution, diffusion of water molecules or cation ions between layers and swelling property in relation to water of clay minerals. Afterward, it has been gradually applied to the study of mechanical behaviors, such as elastic property, failure mechanism and obtained plenty of deeply insights for better understand the macro behaviors. A series of comparison between experimental and calculated results have been conducted and proved MD is an effective method in analyzing the mechanical mechanism of clay-rich materials at atomic scale (Teich-McGoldrick et al., 2012). However, MD simulations were performed on crystal samples subjected to very simple loading paths in most previous researches, such as uniaxial compression or tension (Hantal et al., 2014), shear(Hantal et al., 2014), triaxial compression with constant confining stress (Wu and Firoozabadi, 2020). According to the available researches, the deformation characteristics and failure mechanism strongly depend on the loading path and most geological materials can also be subjected to other types of loading paths which have already widely considered in the macroscopic experiments (Liu et al., 2019b). In accordance with macroscopic laboratory tests, both of the triaxial compression, extension with constant mean stress, creep test are applied respectively on the dry and hydrated Na-montmorillonite (Na-MMT) crystal, the most common and abundant swelling clay mineral in clayey rocks, for deeply understanding of the basic mechanical behaviors in our research.

The objective of our study is to analyze the basic mechanical properties, deformation characteristics, failure mechanism of Na-MMT under different loading path at atomic scale instead of fitting with the conclusions of macroscopic experiment. In addition, the influences of various factors on mechanical properties are also investigated, such as saturation, temperature, anisotropy and so on. Therefore, this thesis is composed of five chapters:

Chapter I reviews the physical and mechanical properties of clay and clayey rocks at

macroscopic laboratory experiments, the previous researches have shown that the mechanical response is strongly dependent on the mineralogical composition, sensitive to microstructural changes induced by loading path. These scientific issues require the atomic exploration which can not be obtained directly through the laboratory test due to the small size and a rare presence in nature. Based on this, the molecular dynamics simulation develops rapidly in recent years and provides the possibility for studying these problems. This is our motivation to investigate the mechanical properties of clay minerals by molecular dynamics (MD). Then, we briefly introduce the development and applications of MD simulation in clayeyh rocks. Finally, molecular dynamics simulations addressing the mechanical properties of such materials are highlighted.

Chapter II mainly focuses on the mechanical behaviors of dry Na-montmorillonite (MMT) to explore the influence of loading path, mean stress, anisotropy of internal structure, temperature on mechanical properties. More precisely, we have loaded the dry Na-MMT model with loading path of triaxial compression and extension. Triaxial compression means one principal stress is increased from initial in-situ stress state while two others are decreased so that the mean stress remains constant. Extension, one compressive principal stress is relaxed and two other ones are increased by keeping the mean stress at a constant value. The comparison between these loading paths allow studying the effect of third stress invariant (or Lode's angle) on mechanical behavior. Besides, a series of MD simulations are performed for these two loading paths with different mean stress of 5 GPa, 10 GPa, 15 GPa and respectively applied in the parallel and perpendicular directions to crystal layers. The stress-strain relationship under various conditions is obtained finally which has shown the exact tendency to macroscopic experiments. The effects of loading path, mean stress and anisotropy on mechanical strength and failure mechanism of dry Na-MMT at atomic scale are analyzed. Besides, the failure strength in the p-q plane in the parallel and perpendicular directions under compression and extension is compared, acquiring the influence of Lode's angle on failure surface and the coefficient related to friction angle and cohesion.

Chapter III studies the effects of hydration on the physical and mechanical properties under triaxial compression with the constant mean stress of 0.5 GPa at room temperature. The hydration extent is characterized by adsorbed respectively four (one-layer hydrated state), eight (two-layer hydrated state), twelve (three-layer hydrated state) water molecules in the interlayer for each unit cell. Then, the swelling curves through the relationship between the interlayer space and the number of water molecules is calculated. Our conclusions show a great agreement well with the experimental and calculated results

from other researches which prove the rationality of our model. Subsequently, the mechanical loading is applied to the models under different water content. Then, the relationship of stress-strain and stress-volumetric strain are obtained. The mechanical strength of two-layer hydrated state is higher than the one-layer hydrated state and the peak axial strain is bigger than the three-layer hydrated state and the two-layer hydrated state also shows the most obvious volumetric compression which are not consistent with macroscopic experimental performance. For our extraordinary conclusion, it is tried to be explained from a structural point of view, the key mechanism triggering their failure is obtained, the arrangement of water molecules in the two-layer hydration state is more orderly and directional, it can resist external loading by rotating more freely, thus reducing structural damage.

Chapter V conducts a series of creep test on the Na-MMT at dry and two-layer hydrated state by molecular dynamics simulation. At first, we focus on the influences of deviatoric stresses level which are selected based on the short-term strength under uniaxial and triaxial compression with the confining pressure of 5 GPa. Therefore, the applied axial stress level applied in our work ranges from 18 to 25 GPa for triaxial creep and it is 12.4 GPa to 18.5 GPa under uniaxial creep. The creep properties under different loading conditions are thus obtained. Finally, the effects of temperature and water content on the curve behaviors are studied and the whole creep curves including primary stage, steady stage and tertiary creep stage are successfully obtained.

Chapter VI generalizes the conclusions based on the main findings of the present study. Also, some perspectives on future work are given closely related to the problems raised throughout the research to well further the study of synthetic clayey rocks.

Chapter I

State of the Art

1 Introduction

As one of abundant existence and wide distribution geomaterials in nature, clayey rocks and clay are generally related to various geological issues and engineering practices. For example, the building of large size tunnels in rocks like clay shale, often involves the operational challenges linked with the stability of the tunnel heading and of the face (Bonini et al., 2009). Besides, shale rocks are the primary reservoir or cap layers in unconventional hydrocarbon exploration. For the underground storage of high-level radioactive wastes, clayey rocks have been generally considered as an ideal candidate host rock in many areas worldwide such as France, Swiss, Belgium and Sweden (Armand et al., 2016). In addition, clay is also selected as the buffer backfill material due to their low permeability property, swelling self-heal and extremely great cation exchange ability (Cui et al., 2012). The short and long-term security requirement in so many engineering applications demand extensively investigation of mechanical properties of clay-based materials to assess their stability. Therefore, the experimental and numerically measures have been largely taken to characterize the strength and deformation features of such engineering materials. Particularly, various mechanical tests on Callovo-Oxfordian (COx) claystone which has been taken from the in-situ rock of underground research laboratory at Bure in France have been performed in our group and obtained greatly valuable conclusions. These accomplishments have helped to build a database and contribute to a key and macro understanding of the basic mechanical behavior of such clay-based materials.

In this chapter, we firstly introduces our motivation for choosing molecular dynamics (MD) simulation to study the mechanical properties. The second part present the previous researches of the mechanical properties of such materials. Finally, the overview of

molecular dynamics simulation using in such materials are summarized.

1.1 Mineralogy and micro-structure

Numerous mineralogical studies have found that the clayey rock at mesoscopic scale is made up of the clay matrix containing mineral inclusions, mostly quartz and calcite grains (Robinet et al., 2015). The SEM image of the micro-structure of claystone is shown in Fig. I .1(a). The clay matrix is usually a combination of a variety of clay minerals, like illite, kaolinite, smectite, chlorite, illite/smectite, while it's proportion and categories varies greatly from sample to sample. For instance, the mineralogical characteristics of Callovo-Oxfordian claystone extracted from the Underground Research Laboratory (URL) at Bure in France is affected by the depth due to geological sedimentary cycles. The component analysis of samples taken from depths of 422 m to 504 m has shown that the clay mineral concentration is about 45–50%.

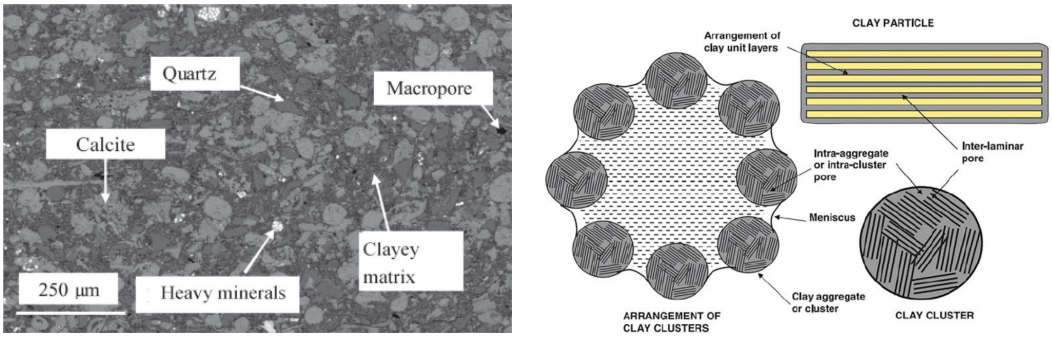

(a) Mineral composition of the COx claystone by SEM image (Robinet, 2008)

(b) Schematic sketch of clay mineral (Ni et al., 2020)

Figure I .1: Microstructure of clay matrix

In the upper part, micas and mixed-layer illite/smectite dominate, whereas in the lower part it transits to mixed-layer illite/smectite associated with kaolinite (Armand et al., 2013; Gaucher et al., 2004; Robinet et al., 2015; Song et al., 2017; Zhang et al., 2021a). The further study has indicated that their relative proportions of illite and smectite are great differences, the illite/smectite includes 70% illite and 30% smectite in the transition unit while consists of 22% illite and 78% smectite in the clay-rich zone (Chuanrui et al., 2021). Certainly, the clay phase is also possible dominated by kaolinite and illite(Hu et al., 2014a; Lebon and Mouroux, 1999; Zhang et al., 2018). Further analysis at a smaller scale shows that the clay matrix itself is composed of clay particles (solid phase) and pores between

such particles, the pores among particles are intra-aggregate pores. The clay particles are formed by stacking the negatively charged layers, the interlayer space between clay layers are the smallest pores in the clay matrix named interlamellar pore which are filled with a variable amount of adsorbed water molecules and with cations that ensure electroneutrality of the system. The diagram of clay mineral is shown in Fig. I .1(b).

1.2 Motivation

Macroscopic mechanical behavior of clayey rocks is determined by microstructure, mineral composition and their interactions at the different scales. Particularly, clay minerals play a key role on mechanical strength and deformation mechanism of clayey rocks. For instance, macroscopic plastic deformation of clayey rocks is mainly caused by the local deformation mechanisms of clay particles and aggregates at the nanometer and micrometer scales (Bornert et al., 2010; Wang et al., 2015a). Besides, the local motion of clay particles is thought to play a role in macroscopic time-dependent deformation of clayey rocks (Armand et al., 2017; Liu et al., 2018c). Further, as the mechanical behavior of clay particles at the atomistic and microscopic scales depends on water content in inter-layer space and inter-particle voids, the macroscopic mechanical behavior of clayey rocks is also strongly sensitive to water saturation degree (Chiarelli et al., 2003; Liu and Shao, 2016b; Vales et al., 2004; Zeng et al., 2019; Zhang et al., 2012). The molecular motion is also influenced by temperature leading to the thermal effect on macroscopic mechanical properties (Liu et al., 2019a; Zhang, 2018). Moreover, the layered structure of clay crystals at the nanometer scale can be one of origins for strongly anisotropic mechanical behaviors of clayey rocks (Armand et al., 2017; Liu et al., 2015b; Niandou et al., 1997; Zhang et al., 2019). Therefore, the characterization of mechanical behaviors of clayey rocks should be based on multi-scale approaches in order to properly take into account influences of mineralogical compositions and multi-scale heterogeneity. Understanding the atomistic size deformation and failure mechanisms of clay particles is indispensable. However, it is very challenging to conduct direct experimental test at such small scale. In this context, molecular dynamics simulations (MD) have been rapidly developed and widely used in modeling the clay-rich materials at nano scale.

According to the previous researches of mineralogical characteristic and mechanical behaviors, Clay minerals, as the main and lowest strength component, almost determines the mechanical behavior of clayey rocks. Meanwhile, the specific sensitivity to water and favorable swelling self-healing property of montmorillonite(MMT) is one of the key factors for the selection of claystone as the host rock and clay as the buffer backfill material for

disposal of high-level radioactive waste. Therefore, we choose the Na-MMT as our first object for exploring the failure mechanism and deformation process at atomic scale. The emphasis in this work is only focused on studying deformation and failure properties of one of principal constituent (clay minerals) of clayey rocks at the atomistic scale and the effects of various factors influencing mechanical behaviors of Na-MMT particles such as stress state, hydration and temperature, loading path and orientation as well as mean stress, instead of matching the stress-strain relationship of macroscopic test data. The results obtained from MD simulations can be used for the first step of multi-scale bottom-up modeling of clayey rocks.

2 Basic mechanical behavior of clay-based materials

Clayey rocks, as a potential geological barrier for underground radioactive waste disposal, are extensively investigated in many underground research laboratories (URLs) world-widely, such as France, Switzerland and so on. Due to the repository's security requires complete understanding of the thermo-hydro-mechanical behaviors and responses to dynamic situations (Bossart et al., 2017; Menaceur et al., 2015; Yu et al., 2014). A large number of experimental investigations have been conducted to explore the short- and long-term thermo-hydro-mechanical performance of the clay host rock, such as mini compression, micro indentation, uniaxial and triaxial compression and extension tests. In addition, plenty of tests have been devoted to investigate the effects of water content, mineral composition, structural anisotropy and temperature on mechanical behaviors of the COx claystone. These accomplishments have led to the understanding of the fundamental mechanical behavior of such materials. In this section, we will give an exhaustive review of previous studies with various important aspects concerning the barrier functions of the clay host rocks, including:

- Basic mechanical properties of claystone.
- Thermal effects on the hydro-mechanical behaviors and properties.
- Water content influences on the mechanical properties and behaviors.
- The influence of loading path on strength and deformation.

2.1 Basic mechanical properties of claystone

2.1.1 Short-term behavior

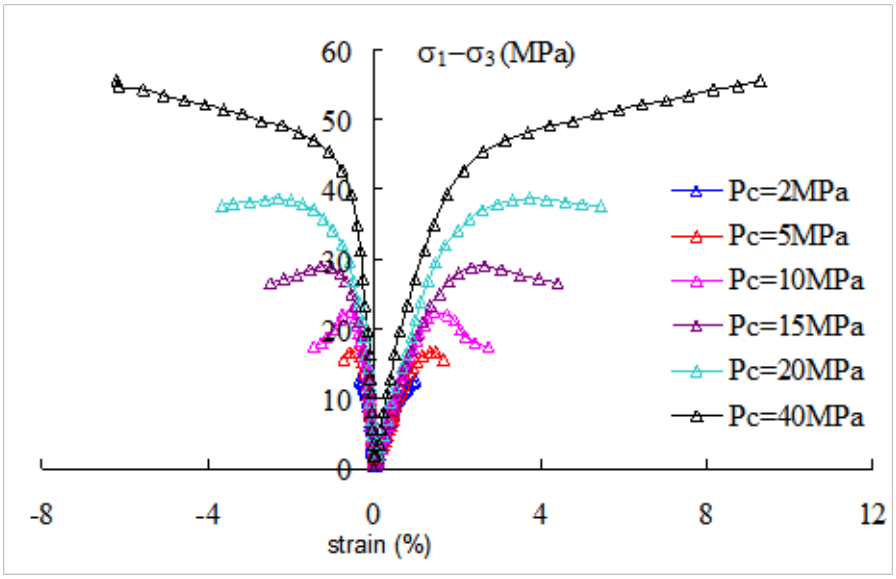

Figure I .2: Stress-strain relationship with different confining stresses (EST30446) (Hu et al., 2014b)

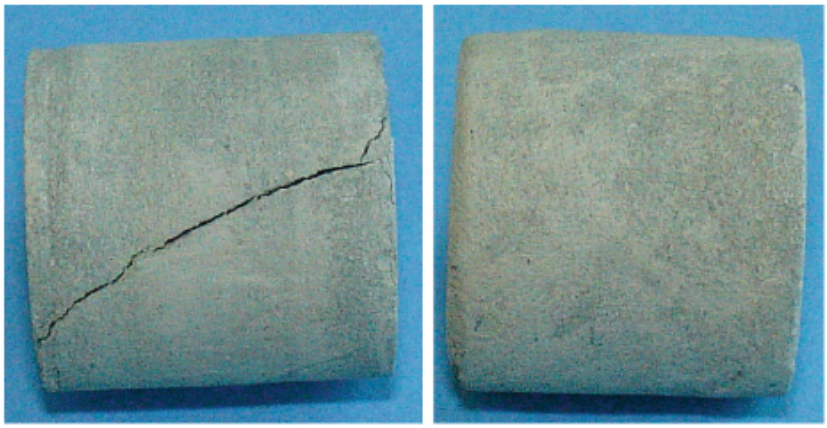

Figure I .3: Failure patern with confining stress of 2 MPa and 40 MPa (Hu et al., 2014b)

In laboratory experiments, the triaxial tests with coupled gas permeability measurement are the common methods to investigate the short-term mechanical behaviors of the clayey rocks through measurements of deformation and strength (Armand et al., 2013;

Liu and Shao, 2016a; Tian et al., 2014; Zhang and Rothfuchs, 2004; Zhang, 2018). The differential stress is loading by adopting the constant axial compression at a rate ranging from 10^{-6}/s to 10^{-8}/s and the lateral confining stress ranges from 2 MPa to 40 MPa. The typical stress-strain behavior of COX claystone in drained with different confining stresses for comparing the influence of confining stress is shown in Fig. I .2, the axial strain is described by hollow circle, black square is the radial strain, red triangle is the volumetric strain and σ_1-σ_3 expresses the deviatoric stress. Compressive stresses and strains are given a positive sign, while tensile stresses and strains are given a negative sign. The basic mechanical behavior of claystone can be expressed from the following stages: it starts with a linear axial compression, radial extension, it means the elastic phase. Then, the curves start a nonlinear region, these nonlinear inelastic strains are caused by frictional sliding along fracture surfaces and are intimately related to the initiation and growth of microcracks. However, the detail mechanical response of claystone with different confining stresses shows significant difference which indicates that the stress-strain is strongly dependent on the confining stress. Under low confining stress, the stress-strain curves start with a nonlinear phase at the beginning of deviatoric loading which is mainly caused by the progressive closure of initial bedding planes and microcracks in the axial direction. With the increase of the confining stress, because the original microcracks are nearly closed during the application of confining force, such a nonlinear phase vanishes. In addition, under low confining stress, sample failure is characterized by a rapid peak stress caused by the coalescence of cracks, resulting in sample splitting. This peak stress state is substantially less noticeable and even disappears with higher confining stress. The emergence of shear enhanced compaction bands is usually accompanied with sample failure. With increasing of confining stress, there is a distinct transition from brittle to ductile behavior. Meanwhile, for the volumetric strain, there is a clear transition from compressibility to dilatancy but this phenomenon is also affected by the confining stress. Under low confining stress, this shift occurs significantly sooner than higher confining stress. Physically, the normal opening of microcracks caused by frictional sliding over rough crack surfaces may be related to volumetric dilatancy in brittle rocks under compressive loads. This matches experimental data on dilatancy effects on clayey rocks that have been published (Naumann et al., 2007; Wong et al., 1997).

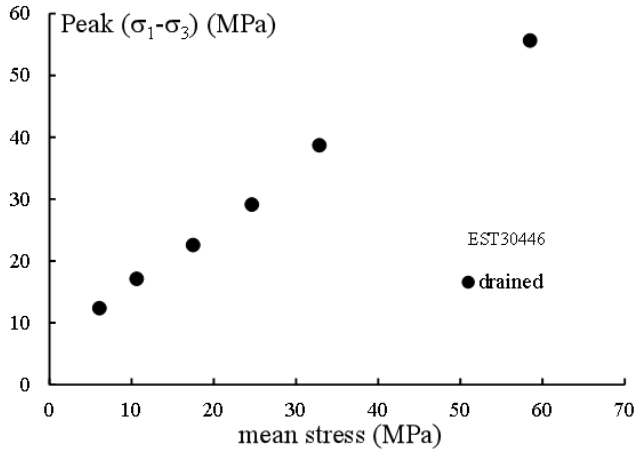

Figure I .4: Failure surface of claystone in drained triaxial compression tests (EST30446, perpendicular, saturated samples,) (Hu et al., 2014b)

The peak stress of claystone under different confining stress is plotted in Fig. I .4, as function of mean stress under drained conditions, it can be approximated as a quasi-linear relation. According to the classic linear Mohr–Coulomb criterion (Hoek et al., 2002). the relationship between the shear strength and mean stress can be defined by the equation:

$$q = \eta p + \mu \tag{I .1}$$

where q is the peak stress at failure. p is the mean stress of claystone. η and μ are parameters related to internal friction angle(ϕ) and cohesion(c) respectively which can be calculated according to the following equation(Hoek and Brown, 1997):

$$\eta = \frac{6\sin\phi}{3-\sin\phi} \tag{I .2}$$

$$\mu = \frac{6c\cos\phi}{3-\sin\phi} \tag{I .3}$$

2.1.2 long-term behavior

The long-term performance of host rock strongly depends on time-related deformation and failure process. This key issue is generally investigated by triaxial creep experiments, the creep property of claystone has been published in the past years (Armand et al., 2013; Belmokhtar et al., 2017; Liu et al., 2018a; Zhang, 2018; Zhang et al., 2019). At the beginning, the creep strains rate of COx claystone have proven to be the order of 10^{-10} to 10^{-11} when it is loaded with a relative low deviatoric stress like 10 MPa (Vales et al., 2002). In addition, the underground environments, like temperature, saturation degree, has a

significant influences on the creep deformation of claystone (Gasc-Barbier et al., 2004), it is also controlled by the deviatoric stress level as well as structural anisotropy(Liu et al., 2015a). Further, there are some researches have devoted to explore and obtain the stress threshold below which creep strains keep stable through multi-step creep tests (Fabre and Pellet, 2006; Liu et al., 2017, 2018b; Yang et al., 2011) and been proven by one-step creep test (Liu et al., 2015a).

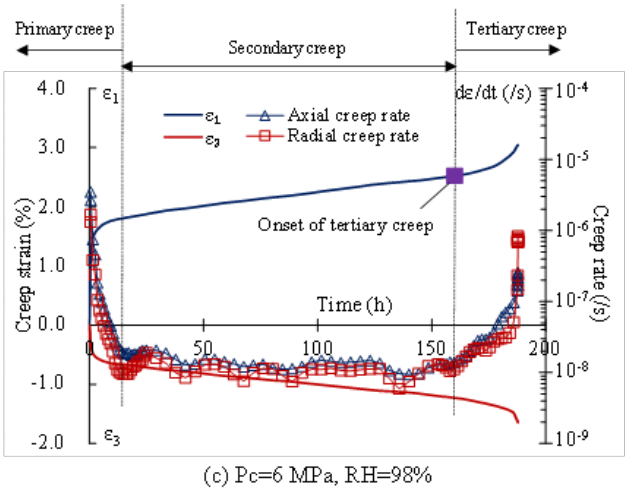

Figure I .5: Creep strain rate and onset of tertiary creep of claystone with RH of 98%and confining pressures of 6 MPa (EST50330) (Liu et al., 2018a).

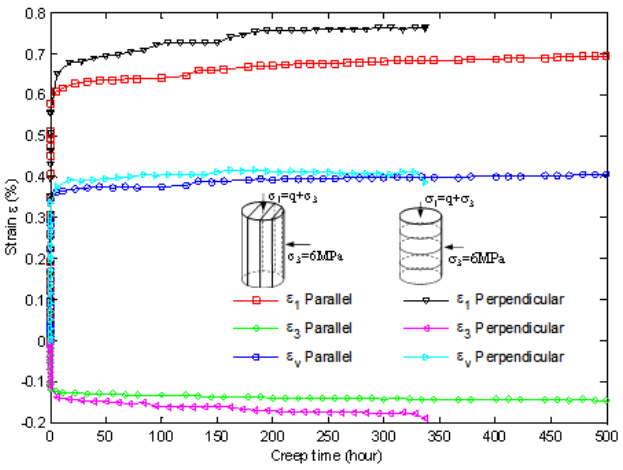

Figure I .6: Comparisons of creep strains in triaxial compression between parallel and perpendicular samples with deviatoric stress of q_{peak}=82% (EST30442-13) (Liu et al., 2015a)

Even so, it is still challenging to study the tertiary creep test for claystone by one step creep test due to the time cost, the question of whether or not there is a creep rate threshold past which tertiary creep can occur remains unanswered. Based on this, Liu et al. (2018a) explored systematically the effects of relative humidity, mineral compositions, anisotropy and confining stress on the creep behaviors of claystone by the triaxial compression. The complete creep curves, including primary, steady and tertiary creep stage are obtained(Fig. I .5). It is also concluded that confining stress increases creep strain rate. The clay minerals especially the smectite plays an crucially role in increasing the creep strain at a certain relative humidity. Further, at high deviatoric stress levels, failure due to acceleration creep was also observed. More valuable is to characterize the threshold of tertiary creep onset under certain specific conditions.

2.2 Thermal effects on the hydro-mechanical properties

The radioactive materials produce heat resulting in a high temperature underground environment which is unfavorable to the stability of underground disposal repository. Therefore, the temperature change becomes a crucial issue in the geological disposal of radioactive (Menaceur et al., 2015, 2016; Monfared et al., 2014; Zhang et al., 2017).

Studies have published the changes in hydro-mechanical responses due to temperature elevation (Belmokhtar et al., 2017; Liu et al., 2019b; Menaceur et al., 2015; Zhang et al., 2007), including thermally-induced expansion, changes in pore pressure, temperature related deformation and strength characteristics, creep behavior and damage over time (Belmokhtar et al., 2017). Further, Zhang (2018) revealed that thermal impact on the strength of a claystone differs from saturated to unsaturated states and from drained to undrained conditions. As the temperature increases, the claystone becomes more ductile and weaker under the saturated and undrained conditions, the decrease of strength induced by temperature is probably caused by the pore pressure increase which reduces the effective mean stress. while heating a claystone in drained can increase the strength significantly. Recently, Liu et al. (2019b) studied thermal effect on peak strain and strength of claystone under triaxial compression with constant mean stress in detail, it concluded the increase of temperature induces a degradation of shear strength and the rise of peak axial and radial strain of the COx claystone, as presented respectively in the Fig. I .7 .

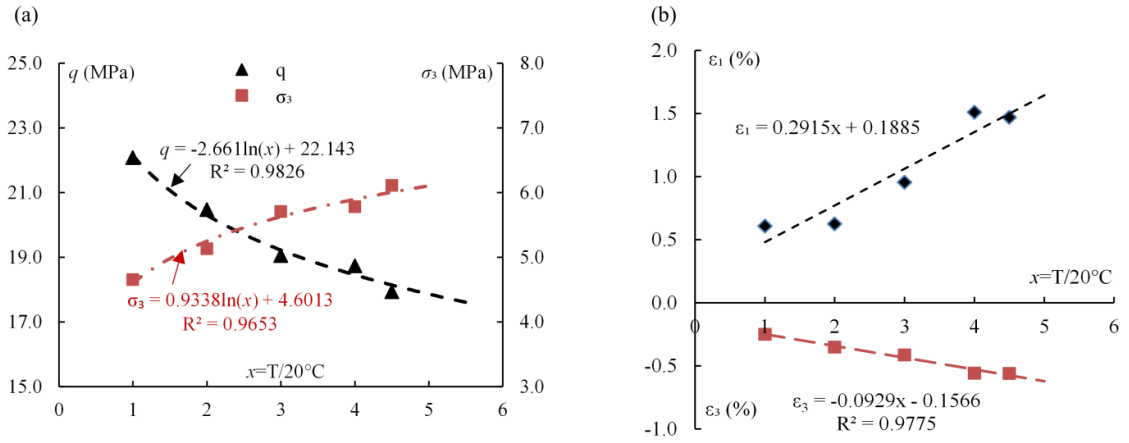

Figure I .7: Thermal effect on peak stress and strain in triaxial compression with constant mean stress (EST52616 and EST28540)

Tian et al. (2014) performed a laboratory test to investigate physical and mechanical behavior of claystone exposed to high temperatures up to 1000°C, showing that the color changes from gray to reddish brown (Fig. I .8), and the deformation modulus and compressive strength first increases (up to 800°C) and then decreases (at 1000°C). Temperature also alters the microstructure and rheological properties of the claystone. Gasc-Barbier et al. (2004); Zhang et al. (2013, 2007) investigated the temperature influences on the long-term behavior of claystone. The creep rate increases with increasing temperature, which also depends on deviatoric stress, confining pressure, loading history, etc.

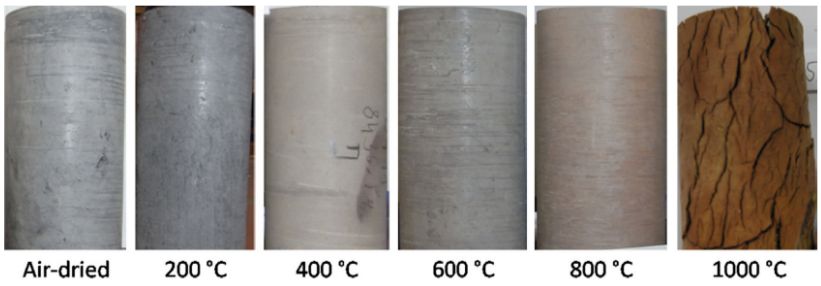

Figure I .8: Meuse/Haute-Marne URL long-term monitoring results of temperature and pore pressure (Wileveau and Bernier, 2008)

Since the thermal expansion coefficient of water is significantly higher than that of the solid grains, thermal pore pressure often occurs in low permeability COx claystone, which was investigated by performing undrained heating test (Braun et al., 2016; Mohajerani

et al., 2012; Monfared et al., 2011) and in-situ experiments. In addition, (Wileveau and Bernier, 2008) obtained the long-term in-situ monitoring results of temperature and pore pressure in Meuse/Haute-Marne URL of Bure in France (Fig. I .9), indicating that the variation of pore pressure shows a good agreement with the changes of temperature.

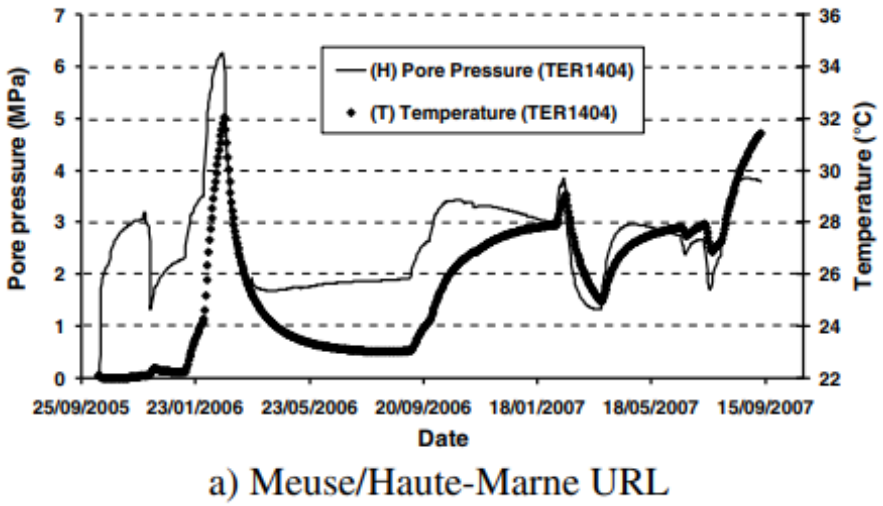

Figure I .9: Meuse/Haute-Marne URL long-term monitoring results of temperature and pore pressure (Wileveau and Bernier, 2008).

2.3 Influences of water content on the mechanical properties

Due to the presence of clay minerals, the mechanical behavior of COx claystone is very sensitive to water saturation. A fairly large number of laboratory tests have been carried out by Andra's various partners. The results obtained are sometimes scattered but confirm some general trends. However, the desaturation or resaturation procedures used in these assays are often the cause of sample degradation. Therefore, interpretations made on the influences of water content may be biased. By way of example, Fig. I .10 shows the stress-strain curves from triaxial compression tests on samples balanced at different values of relative humidity. From these curves, the values of the initial elastic (parallel) modulus and the deviatoric stress at the peak are calculated and can be observed that the elastic modulus and the tensile strength decrease significantly with increasing water saturation. In addition, the deformations (axial and radial) at the peak also increase with relative humidity.

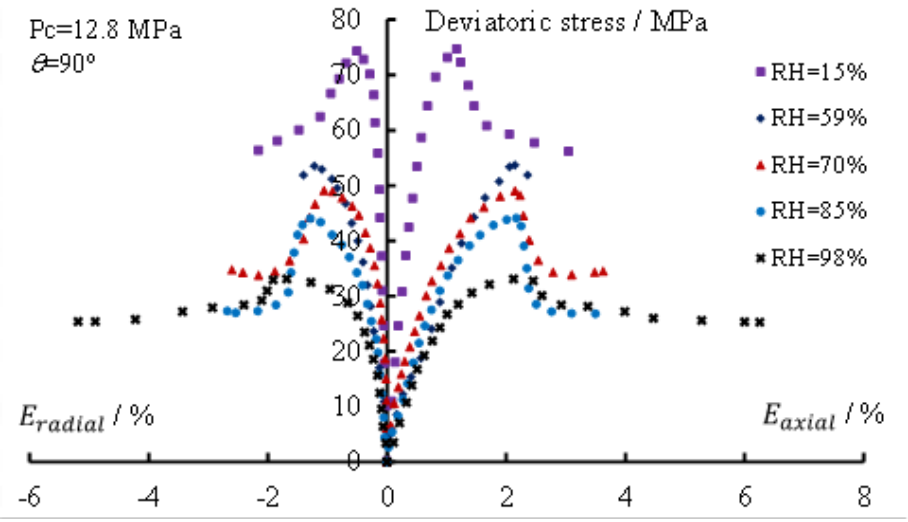

Figure I .10: Stress strain curves of triaxial compression tests with a confining pressure of 12.8 MPa on samples at different relative humidity and cored in the perpendicular direction (90 °, EST42443)(Liu and Shao, 2016a)

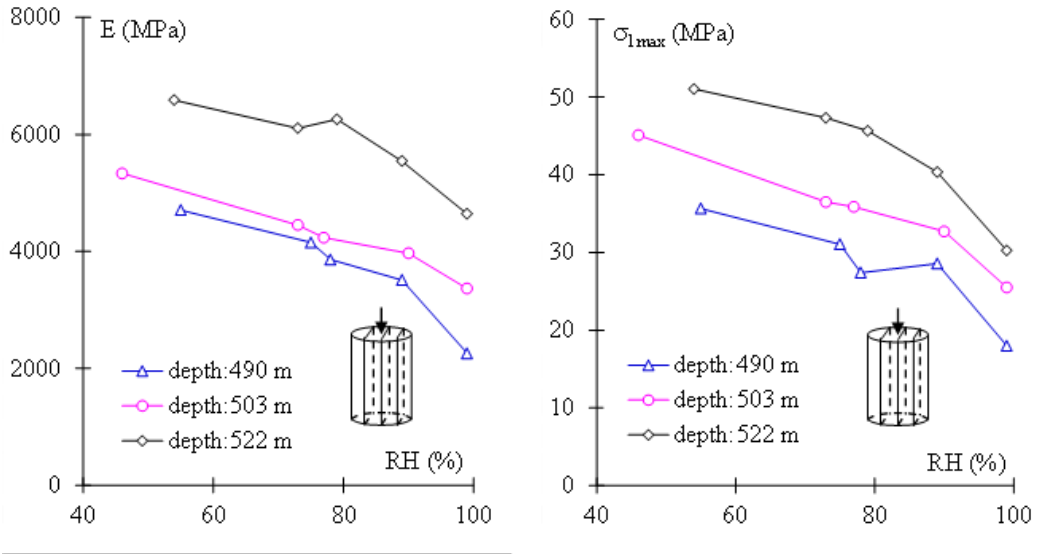

(a) Evolution of axial elastic modulush (Zhang et al., 2012).

(b) Compressive strength as a function of relative humidity during mini-compression tests on samples from three different depths (Zhang et al., 2012)

Figure I .11: Mechanical property of claystone under different relative humidity

This shows that the plastic strain before the peak is greater for samples with high water saturation. The post-peak softening becomes less abrupt. There is therefore a clear transition from brittle behavior to ductile behavior. Similar results were obtained in uniaxial mini-compression tests on samples cored in the parallel direction, as shown in Fig. I .11. These effects of relative humidity on the mechanical strength and deformability of Cox claystone can be partially explained by the microscopic observations obtained using the environmental scanning electron microscope (ESEM). At high humidity levels, there is a large opening of the pores and significant swelling of the Illite / Smectite minerals due to the presence of water. As a result, the material exhibits a more ductile behavior, undergoes much greater deformation and exhibits lower mechanical strength, Show in Fig. I .12

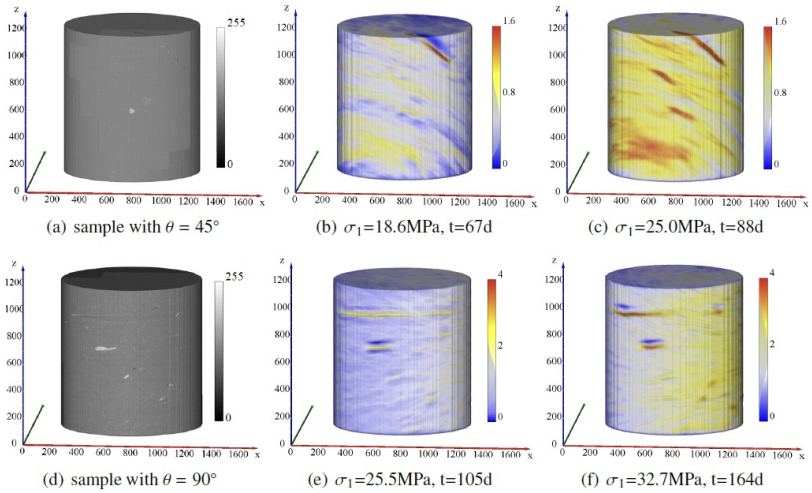

Figure I .12: Variations in peak deviatoric stress, axial elastic modulus and axial peak strain as a function of relative humidity (triaxial compression on samples cored in the perpendicular direction) (Shi et al., 2021).

2.4 Loading path influences on the mechanical properties

The knowledge of mechanical properties of clay-rich rocks derived from laboratory tests strongly depends on the measurement methods. For instance, micro/nano-indentation (Hu et al., 2014a; Zhang et al., 2014a), dehydration and hydration at different constant applied stress levels (Yang et al., 2013a; Zhang et al., 2007), specific unconfined tests(Espitia et al., 2019; Huang et al., 2014), uniaxial creep test (Fabre and Pellet, 2006; Liu et al., 2015a), uniaxial compression (Espitia and Caicedo, 2020; Yang et al., 2011, 2013a). However, the widely used loading paths for studying the mechanical properties of clay-rich rocks are the

various deviatoric shear (Liu et al., 2019b; Menaceur et al., 2016; Sarout and Guéguen, 2008; Sarout et al., 2007; Yang et al., 2013a; Zhang and Laurich, 2020; Zhang et al., 2014a) for corresponding to the disturb of the construction and storage of the disposal repository. At the beginning, the common shear test is the conventional triaxial compression with constant confining pressure which means the axial increase while the radial stress keep constant(CTC). Then, (Liu et al., 2019b) explored the mechanical property of claystone under the lateral decompression test (LD) which means the axial stress increases while the radial stress decreases to keep the constant mean stress, the stress-strain curves between a CTC test at confining pressure of 12 MPa and an LD test at mean stress of 12 MPa is shown in Fig. I .13. Subsequently, (Zhang et al., 2019) performed the deviatoric test on claystone under more complex four different loading path in the coring orientation of $\aleph = 0°$, $30°$, $45°$, $60°$ and $90°$ to explore the influences of loading path and anisotropy. The similar but further research was subsequently published by (Zhang and Laurich, 2020), aiming to investigate the effects of loading paths and water saturation on the deformation and strength behavior of the OPA sandy facies with a large number of samples. The relationship between shear strength and mean stress under various loading path for samples with different saturation degree is shown in Fig. I .14(a) and Fig. I .14(b). Combined with the above studies, the published deviatoric stress testing mainly are mainly as follows:

- LD: Compression under constant mean stress by increasing axial stress and decreasing radial stress at the same time.
- TCS/CTC: Compression by increasing axial stress and keeping constant radial stress.
- TCD: Cyclic axial compression and constant radial stress.
- TEA/TES: Extension by increasing radial stress at constant axial stress.
- TEM: Extension at constant mean stress by simultaneously increasing radial stress and decreasing axial stress.

Form these researches, it can be obtained the stress-strain behavior is qualitatively independent of loading path, it shows the obvious elastoplastic characteristic. However, the quantities of the deformation, strength and volumetric strain are different. On the whole, the volumetric strain in the CTC test is essentially compressive, while that in the LD test clearly shows a dilatancy, the failure strength under LD is lower than that under CTC, triaxial compression is higher than that under extension. The corresponding strength increases with the increase of mean stress, their strength behavior of the claystone can

be expressed by the Mohr-Coulomb failure model. In addition, the mechanical strength decreases with the increase of water saturation.

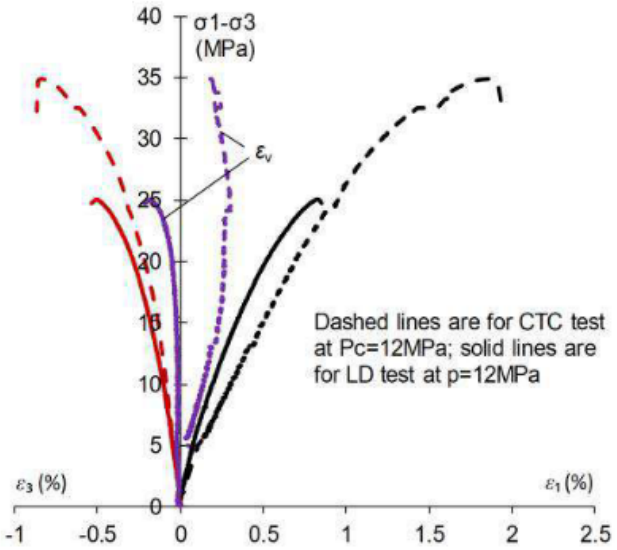

Figure I .13: Comparison of stress–strain curves between a CTC test at confining pressure of 12 MPa and an LD test at mean stress of 12 MPa (EST52616 and EST28540)(Liu et al., 2019b).

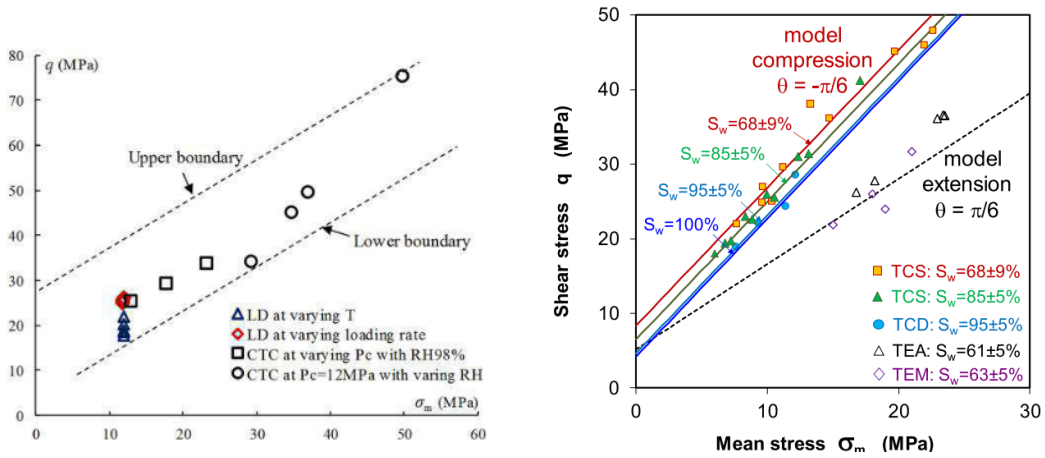

(a) Comparisons of failure stress in the p−q plane between CTC and LD tests(EST52616, EST28540)(Liu et al., 2019b)

(b) Shear strength of claystone under different loading path(Zhang and Laurich, 2020)

Figure I .14: Comparisons of failure stress in the p−q plane

3 Principles of Molecular dynamics (MD) simulations

3.1 Introduction

Molecular dynamics simulation is a method of an integration of Newton' equations of motion in the system over time. In contrast to statistical mechanics, the movement of particles with time is deterministic in MD. The basic idea is shown in the Fig. I .15, it consists of the following steps:

- Build atomic model with the information of initial position firstly.
- Given a random initial velocity for each atom, which follows the Boltzmann distribution. The atoms start to move under the provided interatomic potential (Force Field) which is determined by the relative positions among atoms, the force acting on atoms is the negative gradient of interaction energy.
- Based on above information, the new positions and velocities of atoms after a small time interval (time step) can be obtained according to the Newton' law of motion. The above steps are repeated for a long period and then generated the trajectories of atoms at the microscopic level.
- Finally, Statistical mechanics is used to translate the microscopic information into macroscopic measurable such as pressure, temperature, heat capacity, and stress tensor.

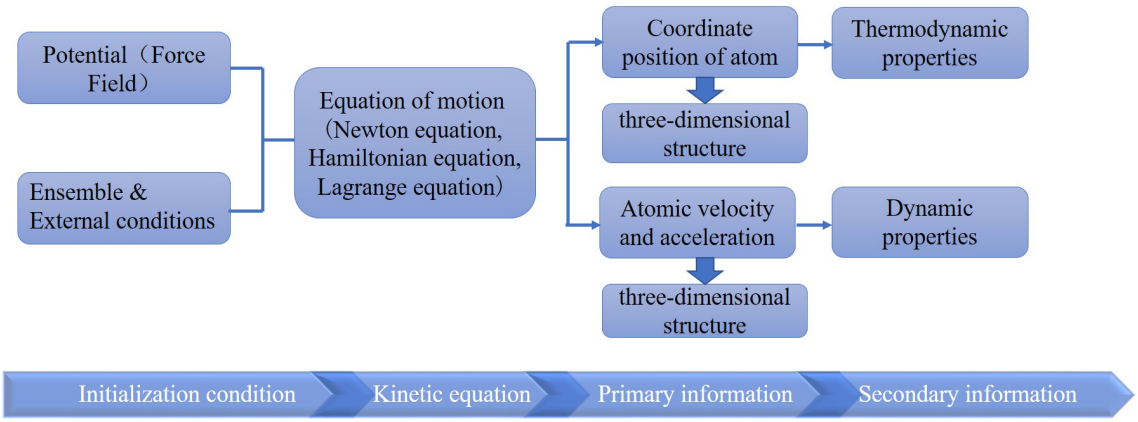

Figure I .15: General idea of molecular dynamics simulation

3.2 Force field (the potential function for atoms interaction)

The correctness of the description of inter-particle interaction potential determines the quality of MD simulation outcomes. This decision is heavily influenced by the application of molecular dynamics to different materials. The potentials means when the atoms are adjacent within a specified distance, They can interact each other, including the attraction and repulsion. This interaction is so called force field. Atoms eventually move to the lowest energy at equilibrium state following the the Newton' equations of motion. The force acting on the atoms is related to the negative gradient of potential corresponding to position expressed in eq. I .4.

$$f = -\frac{\partial U(\boldsymbol{r}_1, \boldsymbol{r}_2, ...\boldsymbol{r}_N)}{\partial \boldsymbol{r}(i)} \tag{I .4}$$

where u is the potential. Potential for a specific systems are obtained by fitting experimental data or calculated data from first-principles methods. Recently, significant progress has been made in the development of potential, it can be roughly divided into two categories: inter-molecular interaction and intra-molecular interaction.

3.2.1 inter-molecular interaction

The inter-molecular interactions are mainly non-bond pair potential which include van der Waals and Coulomb interaction, expressed by eq. I .5.

$$E = E_{Vdw} + E_{Coulomb} \tag{I .5}$$

The Van der Waals interaction between two particles arises from a balance between repulsive and attractive forces. At short distances between two atoms, repulsion predominates while the attraction arise to main interactions at long distances. The most common method to describe Van der Waals interaction is the Lennard-Jones potential (12-6 potential), shown in eq. I .6 and I .7, where 6 power term is the attraction energy and the 12 power term describes the repulsive force.

$$E_{Vdw} = \sum_{i \neq j} D_{0,ij}[(R_{0,ij}/r_{ij})^{12} - 2(R_{0,ij}/r_{ij})^{6}] \tag{I .6}$$

$$\left\{ \begin{array}{l} R_{0,ij} = 1/2(R_{0,i} + R_{0,j}) \\ \\ D_{0,ij} = (D_{0,i} * D_{0,j})1/2 \end{array} \right\} \tag{I .7}$$

Where $R_{0,i}, R_{0,j}$ represent the distance at which the potential energy for atom i and atom j respectively is zero and the $D_{0,i}, D_{0,j}$ represent the minimum Lennard-Jones potential energy for atom i and atom j respectively.

The Fig. I .16 is the schematic of the Lennard-Jones pair potential, it can be obtained as the distance between atoms approaches infinity, the potential energy between atoms approaches zero. When the atoms are very close, the Pauli repulsion due to overlapping electron clouds takes place, and the arbitrary 12 power term describes this increase in repulsion. At equilibrium atomic distance, repulsion is equal to attraction corresponding to the energy is minimized.

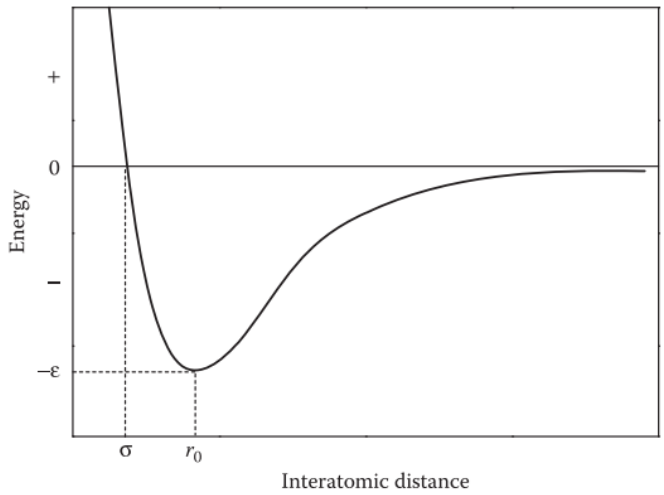

Figure I .16: Schematic representation of the Lennard-Jones pair potential (Lee, 2016)

The electrostatic interaction between two atoms is calculated by the Coulomb's law, shown in the eq. I .8. In the Coulombic energy, e is the charge of an electron, ϵ_0 is the dielectric permittivity of a vacuum ($8.85419 \times 10^{12} F/m$) and q_i and q_j are the atomic partial charges, which can be derived from quantum mechanics calculations.

$$E_{Coul} = e^2/4\pi\epsilon_0 \sum_{i \neq j} q_i q_j / r_{ij} \tag{I .8}$$

3.2.2 Intra-molecular interaction

Describing intra-molecular interactions is far more complicated than inter-molecular interactions, because molecules are always connected by covalent bonds. Molecules interact through bond, angle, dihedral and other spatial structure. Various force fields have been proposed to describe these complex short-range interactions. It mainly includes the following items(eq. I .9)

$$E = E_{bond} + E_{angle} + E_{torsion} + E_{oop} + E_{cross} \tag{I .9}$$

Where:

– E_{bond} describes the bond energy between two atoms which is related to the bond length caused by the bond motion of elongation and contraction. The simplest and most common expression of this interaction is pure harmonic potentials, shown in the eq. I .10

$$E_{bond} = \sum_{bonds} \frac{1}{2} k_b \left(b - b_0\right)^2 \tag{I .10}$$

where b is the bond length. This is almost identical with expressing the motion of spring with string constant k. Although the description is simple, it can be good enough to solve many problems where we are always close to equilibrium. However, harmonic potentials also has its inevitable disadvantage, it can not describe the bond breakage reasonably resulting in the failure-related characteristics that do not correspond to the actual situation. Therefore, it only describes the elastic region accurately. Further, the Morse potential have been improved in this respect, it is expressed in eq. I .11, it means the interaction between the atoms approaches zero as the distance approaches infinity. It is still not accurate, because covalent bonds break completely at certain times.

$$E_{morse} = D_e(1 - e^{-a(r-r_e)}) \tag{I .11}$$

where D_e is the well depth, r is the distance between the atoms, r_c is the equilibrium bond distance.

– E_{angle} describes the bond angle energy, such as three-body potential. The simplest way to describe angular motion is still the harmonic potential, in eq. I .12.

$$E_{angle-bend} = k_2(\theta_{ijk} - \theta_0)^2 \tag{I .12}$$

where k_2 is a force constant, θ_{ijk} denotes the bond angle and θ_0 is the equilibrium bond angle.

– $E_{torsion}$ describes the torsion which is the rotation of two sections of a molecule relative to one other generates energy. The simplest application of this potential energy is used to express the rotation of two parts of the ethane molecule C_2H_6 around the central C-C bond. The most common calculation method is shown in eq. I .13

$$E_{torsion} = V_1 \left(1 + cos\left(\phi\right)\right) + V_2 \left(1 + cos\left(2\phi\right)\right) + V_3 \left(1 + cos\left(3\phi\right)\right) \tag{I .13}$$

The first part is related to dipole-dipole interactions, the second term is to bond conjugation and the third part is to steric energy.

– E_{oop} describes out-of-plane interactions, i.e. When one component of a molecule is out of plane with another, the energy changes. The common functional form is simple, in eq. I .14

$$E_{oop} = \sum_{x} H_{\chi}\chi^2 \tag{I .14}$$

Where χ is the displacement out of the plane.

– E_{cross} are terms that cross over into the other interaction terms, containing the items mentioned above. For example, They can be used to describe relationships between two displacements, an angle, and a torsion.

3.3 Statistical Ensemble

In statistical physics, ensemble generally refers to a collection of various possible states of a system under certain state conditions. It represents a large number of independent systems with identical properties and structures in various motion states. This concept was first formally proposed by Gibbs (1878). All the characteristics and properties of the various microscopic physical states of the system at a specific moment of equilibrium can usually be accurately obtained through mathematical analysis. Therefore, many different microscopic configurations of a big system result in the same macroscopic qualities, meaning that knowing the exact specific motion of every particle in a system is not required to forecast its features. Simply averaging over a huge number of similar systems, each in a distinct microscopic configuration, is sufficient. Ensemble averages can be used to express macroscopic measurable quantities. Statistical ensembles are usually characterized by fixed values of thermodynamic variables. In molecular dynamics research, the most commonly used ensembles are as follows: Microcanonical ensemble (NVE), Canonical ensemble (NVT), Isothermal-Isobaric ensemble (NPT), Grand canonical ensemble (VTμ).

- Microcanonical ensemble (NVE) describes a collection with the constant energy (E), number of particles (N), and volume (V).

- Canonical ensemble (NVT) represents a collection of all possible states of a system which keeps constant temperature through the energy exchange with thermostats. The macroscopic properties of the canonical ensemble are determined by the three parameters of the system: thermodynamic temperature (T), number of particles (N) and volume (V).

- Isothermal-Isobaric ensemble (NPT) is one of the most important ensembles which keep the constant particles (N), pressure (P) and temperature (T). It is widely used to simulate the experimental environment with constant pressure and temperature.
- Grand canonical ensemble (VTμ) is characterized by fixing the volume (V), temperature (T) and chemical potential (μ).

3.4 Integral algorithm for Newton equations of motion

3.4.1 Newton equations of motion

For a system composed of N atoms, the force acting on the i atom comes from the negative gradient of the sum of its interaction potential with other (N-1) atoms. According to the previous chapter, the motion of atoms follows Newton's law of motion. Therefore, the equation of motion is related to the change of energy versus position over time, it can be expressed in eq. I .15.

$$F = ma = m\frac{dv}{dt} = m\frac{d^2r}{dt^2} = m\frac{dp}{dt} \tag{I .15}$$

Where **a** is acceleration, **v** is velocity, t is time, **t** is position, **p** is momentum.

It can be concluded the force acting on the atoms can be obtained by deriving the potential energy relating to the relative position among atoms at a given time. Atoms in the system begin to move when given initial velocity and position information, after a time-step, the set of atomic velocity and position can be collected, this process is repeated indefinitely to produce a series of equations of motion. The calculation process is shown in the Fig. I .17

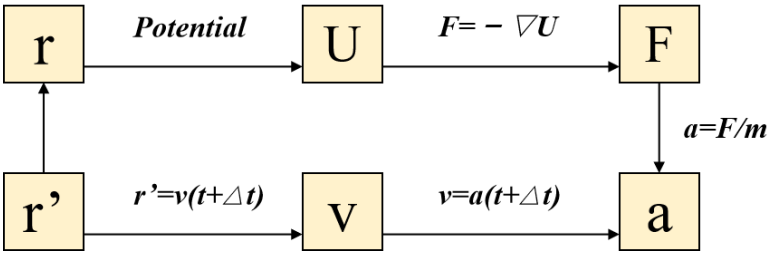

Figure I .17: The diagram of the calculation of Molecular Dynamic simulation

Based on the above process, a large number of equations of motion will be generated which have no analytical solutions due to the complexity of the function. They must be solved numerically. Therefore, a great deal of numerical solutions have been developed to integrate these equations of motion, as listed below:

- Verlet algorithm (Verlet, 1967)
- Velocity Verlet (Swope et al., 1982)
- Leap-frog algorithm (Van Gunsteren and Berendsen, 1988)
- Beeman's algorithm (Beeman, 1976)
- Symplectic reversible integrators (Tuckerman et al., 1992)

In the simulation, the selection of the integration algorithm is mainly considered from the following aspects:

(1) It can calculated fast and accurately.

(2) It allows to choose a long enough integration time-step.

(3) It should be as near to the classical trajectory as possible.

(4) It must comply with recognized conservation principles for energy and momentum, as well as the time-reversible property.

(5) It should have a simple enough form and be easy to implement in computer programs.

3.4.2 Verlet algorithm

The Verlet algorithm is proposed by Verlet (1967), it is derived from the two Taylor expansion for the position of next step and last step in time respectively, they are expands to the third term and expressed by eq. I .16 and I .17.

$$r(t+\Delta t) = r(t) + v(t)\Delta t + \frac{1}{2}a(t)\Delta t^2 + \frac{d^3r(t)}{3!dt^3}\Delta t^3 \tag{I .16}$$

$$r(t-\Delta t) = r(t) - v(t)\Delta t + \frac{1}{2}a\left(t\right)\Delta t^2 - \frac{d^3r\left(t\right)}{3!dt^3}\Delta t^3 \tag{I .17}$$

Add the above two equations (eq. I .16 and I .17) forming the new displacement expression at next step, in eq. I .18

$$r\left(t+\Delta t\right) = 2r\left(t\right) - r\left(t-\Delta t\right) + a\left(t\right)\Delta t^2 \tag{I .18}$$

It is worth noting that the Verlet algorithm makes the position at $t+\Delta t$ correlate with the position at $t-\Delta t$ resulting in there are two integration time-steps during movement. Therefore, the initial position and velocity are not enough to start the calculation. In addition, the velocity at t does not occur in eq. I .18, the velocity at time t can be expressed with the position at $t+\Delta t$ and $t-\Delta t$, shown in eq. I .19. Therefore, In order to

prevent the position at time $t-\Delta t$ from appearing in the calculation, it can be equivalently replaced by the velocity at time t and the position at time $t+\Delta t$.

$$v\left(t\right)=\frac{r\left(t+\Delta t\right)-r\left(t-\Delta t\right)}{2\Delta t} \tag{I .19}$$

The verlet algorithm is simple and only require the velocity, position at time t and the position at $t+\Delta t$. It is also accurately except for ignoring the higher order terms in Taylor's expansion.

3.4.3 Velocity Verlet

Velocity algorithm is another calculation method that is frequently used in molecular dynamics simulation, including in our work. Compared with the verlet algorithm, its improvement lies in the application of physical quantity (velocity, position, acceleration) at time $t+\Delta t/2$, expressed in eq. I .20 and I .21

$$v\left(t+\frac{\Delta t}{2}\right)=v\left(t\right)+\frac{1}{2!}a\left(t\right)\Delta t \tag{I .20}$$

$$r\left(t+\Delta t\right)=r\left(t\right)+v\left(t\right)\Delta t+\frac{1}{2!}a\left(t\right)\Delta t^{2}=r\left(t\right)+v\left(t+\frac{\Delta t}{2}\right)\Delta t \tag{I .21}$$

It can be seen the velocity at time $t+\Delta t/2$ is calculated through the velocity and acceleration at time t, the displacement at time $t+\Delta t/2$ is expressed through the position, velocity and acceleration at time t. Meanwhile, the acceleration at time $t+\Delta t$ can be calculated by Newton's law of motion or potential (eq. I .22).

$$a\left(t+\Delta t\right)=-\left(\frac{1}{m}\right)\frac{dU\left[r\left(t+\Delta t\right)\right]}{dr}=\frac{F\left(t+\Delta t\right)}{m} \tag{I .22}$$

The velocity at time $t+\Delta t/2$ can be expressed by the velocity at time t and the average acceleration at time t and $t+\Delta t/2$. According to eq. I .20 and eq. I .22, it gets converted to the relationship with the velocity at time $t+\Delta t/2$ and the force at time $t+\Delta t$. shown in eq. I .24

$$v\left(t+\Delta t\right)=v\left(t\right)+\frac{a\left(t\right)+a\left(t+\Delta t\right)}{2}\Delta t=v\left(t+\frac{\Delta t}{2}\right)+\frac{1}{2}a\left(t+\Delta t\right)\Delta t \tag{I .23}$$

$$v\left(t+\Delta t\right)=v\left(t+\frac{\Delta t}{2}\right)+\frac{1}{2}\Delta t\frac{F(t+\Delta t)}{m} \tag{I .24}$$

Finally, full synchronization of the positions, forces and velocities is obtained. This algorithm is widely used because it is simple and easy to implement, also has relatively high accuracy which is not influenced by the time-step.

3.5 Boundary condition

Limited by calculation methods, the time required for molecular dynamics calculations tends to increase exponentially as the number of atoms increases. At present, the computing power of ordinary super-computing can only reach the order of one million, while the number of atoms in the real system often exceeds that of the analog system by several orders of magnitude. It is very important to choose a reasonable boundary condition in the MD simulation process. Because a suitable boundary condition can obtain some macroscopic properties by constructing a model as small as possible, which not only greatly improves the computational efficiency, but also can reduce the cost of calculation.

Periodic boundary conditions (PBC), presented by Born and Von Kármán (1967) is one of the commonly used boundary conditions. It's main idea is to replace the macroscopic system with a periodic box of cells. In virtue of periodic boundary conditions, the central cell seems to be repeated infinitely around it which means the atoms in the initial cell uniformly can be arrange as ghost atoms along the periodic direction. The model eventually was extended over the entire space. In this way, although we have only established a small part of the model, but the model system we used to calculate is actually close to infinity which is more realistic. When dealing with the atoms on the boundary, the interaction force between the real atoms and other ghost atoms in the initial cell is calculated. The basic schematic structure is shown in Fig. I .18

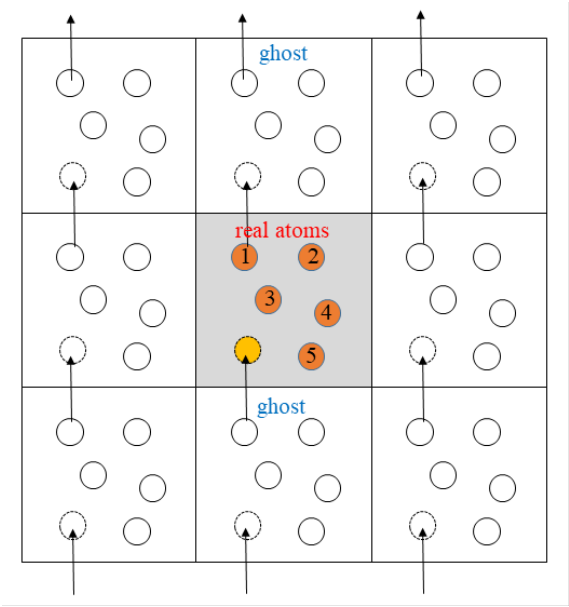

Figure I .18: Periodic boundary conditions

Non-periodic boundary conditions means the above-mentioned periodic replication on the boundary is not adopted, which are usually widely used in the study of nano-sized materials. For example, the normal boundary of two-dimensional materials and the non-axial boundary of nanowires can be used to explore the size effect of nanomaterials or physical and chemical phenomena. There are also multiple settings for periodic boundaries. It can be roughly divided into: flexible boundary conditions, free boundary conditions and fixed boundary conditions.

The following two factors are generally considered for selecting boundary conditions. On the one hand, in order to effectively reduce the computational workload, the size of system in the simulation needs to be reduced as much as possible. At the same time, for achieving the goal of maximization and avoid interference due to dynamics, the model size as large as possible in the simulation is required for statistically accurate and reliable. On the other hand, it is necessary to proceed from the actual physical nature, taking into account the coupling of volume changes, stress balance, and strain characteristics with reality.

3.6 Advantage of molecular dynamics simulation

Comparison to the macro constitutive modeling the molecular dynamics shows many advantages:

- At first, the model is specific, the only input in the modeling is the interatomic/intermolecular interaction, there are no any assumptions are made about the processes/mechanism.

- Besides, comparing to the Monte Carlo, the movement of atoms is specific because it need not follow Newton's equations of motion which can avoid randomness and closer to the reality.

- Besides, MD can provide a detailed molecular/atomic-level information for deep understanding under a various of processing conditions, the motion among atoms can be intuitively observed may lead to the discover new physics/mechanisms.

4 Application of molecular dynamics simulation in physical mechanical properties of clay minerals

Molecular dynamics simulation is a rapidly developing method with the improvements in computer performance and the deep exploration of scientific issues in recent years. It offers the possibility for computing thermodynamic equilibrium and dynamical properties of clay minerals at nanoscale. In the MD simulation, we build firstly the atomic system based on the experiment results like large volume of powder X-ray, neutron diffraction data, X-ray absorption and X-ray reflectivity, which can be regarded as a collection of particles. The particles interact with each other leading to their movement which obey the Newton's equation of motion. The goal is to compute the atom's trajectories numerically by involving the interaction model. We balance the system until the properties of the system no longer change with time, and then capture our desirable properties according to the trajectory of atoms.

4.1 Atomic structure of montmorillonite

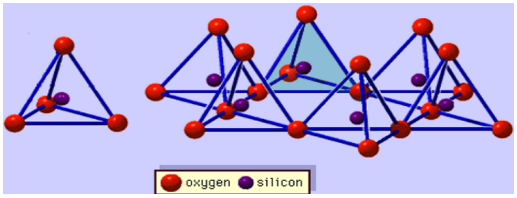

(a) Silicon tetrahedron sheet (Zheng, 2009)

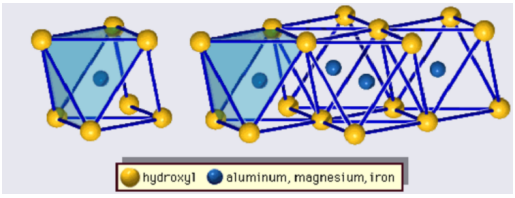

(b) Oxychloride octahedron sheet (Zheng, 2009)

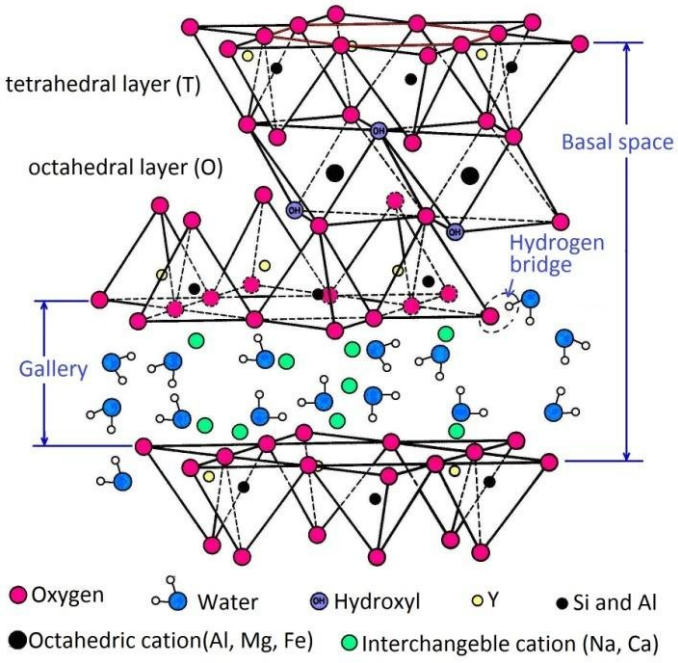

(c) tetrahedron-Octahedral-tetrahedron (Gutiérrez, 2010)

Figure I .19: Diagrammatic sketch of the montmorillonite structure

Montmorillonite, the most common clay minerals and main component in clay-rich rocks, is the typical 2:1 clay of smectite group composed of two types of structural in sheets and layers. The terahedral sheet, shown in Fig. I .19(a), is made up of silicon-oxygen terahedra that are joined by sharing three corners with neighboring tetrahedra to form a hexagonal network. Each tetrahedron's remaining fourth corner connects to an adjacent octahedral sheet. The octahedral sheet usually consists of closely packed oxygen and hydroxyl molecules in which aluminum, magnesium, iron atoms are arranged in octahedral coordination shown in Fig. I .19(b). Then, the octahedral sheet is sandwiched by two tetrahedrals sheets to form a layer which is usually negatively charged because of

isomorphous substitution, it means the displacement of octahedral aluminum and tetrahedral silicon. In general, one out of every eight octahedral metal atoms is replaced by magnesium and so on. In the tetrahedral sheets, one thirty-second of the silicon atoms is replaced by iron, magnesium and aluminium. The nearest sites can not be substituted at same time according to Loewenstein's rule. The interlayer space between two neighbouring layers is filled with different number of water molecules forming the complicated hydrogen network which is one of the main linkage of clay layers. Besides, there are also cations to ensure the electric neutrality of systems and connect the clay layers through the Coulomb and van der Waals forces. The common monovalent counterions are Na^+, K^+, Li^+ or Ca^{2+}, Mg^{2+} of dyadic. The diagrammatic sketch of the montmorillonite structure shown in Fig. I .19(c).

4.2 Swelling property of clay minerals

The application of MD simulations to clay minerals begins with the problems related to hydration. An typical example to calculate the swelling behavior of Na-MMT is published by (Cygan et al., 2004), where a small supercell was used to model the expansion of the clay mineral layers with increasing number of interlayer water molecules. The swelling curve, presented in Fig. I .20, is characterized by the basal spacing as a function of water molecules which is well agreement with the experiment data (Fu et al., 1990). It has proven that the water molecules can form hydrated-layers step by step, the one-layer hydrate is stabilized at a basal spacing of approximately 12 A° with 3 water molecules between interlayer for unit cell. The stabilization will be broken and the layer spacing continues to expand with the introduction of water molecules until two-layer hydrate is formed. Finally, the simulations suggest a slight stabilization of a three-layer hydrate. There are only two layers of water molecules can be found in the experiment, but for the Wyoming MMT composition the layer structures continue to expand with higher water contents due to the decrease of the Coulombic interactions and the enhancement of the relatively strong hydration of the interlayer cations in the virtual world (Boek et al., 1995b; Shroll and Smith, 1999; Underwood and Bourg, 2020; Yeh and Hummer, 2004).

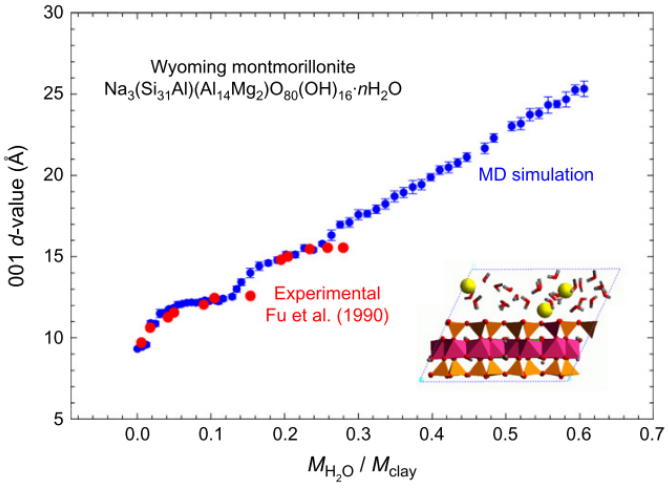

Figure I .20: Swelling curve for the hydration of Na-MMT (Cygan et al., 2004). Experimental data from (Fu et al., 1990)

4.3 Interlayer structure of clay minerals

The layer and interlayer structure have also attracted much attentions of researchers for better understand the atomic structure and interlayer connection. It can be obtained by the equilibrium structure of trajectory file which can store atomic positions and velocities for time steps associated with MD simulation. The existing researches have provided the relative atomic density profiles of hydrated Na-MMT models shown in Fig. I .21 which represents the two-layer hydrated system. The layered clay mineral structure is clearly identified by the dominant peaks for the oxygen atoms of tetrahedron and octahedron. The relatively diffuse behavior of water in the interlayer region is represented by two broad oxygen of water peaks. Interlayer Na occurs primarily in the central region of the interlayer space fully coordinated by water. The atomic profile structure reported by different publications is not always same. For example, (Greathouse and Cygan, 2013) have presented that not all interlayer cations are hydrated, there are still some Na^+ exhibit near the tetrahedral layer having Al substitution which is influenced by many factors like water model and so on.

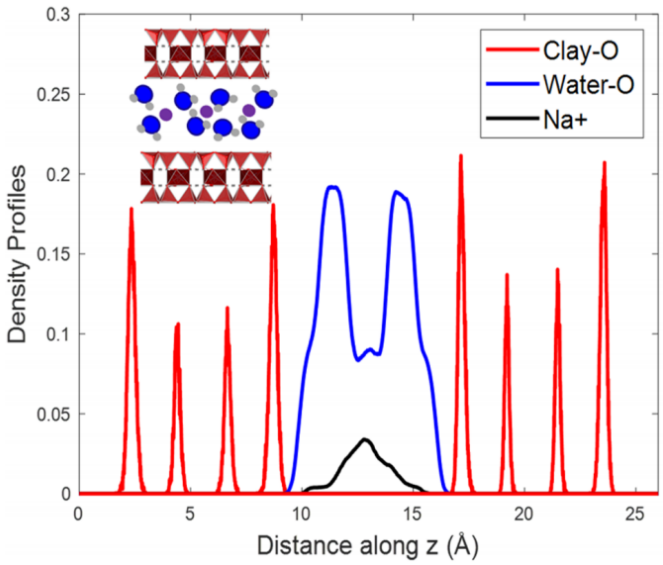

Figure I .21: Atomic density profiles of a two-layer hydrated Na-MMT at equilibrated state(Subramanian et al., 2020)

4.4 Diffusion of interlayer cations and water

The molecular dynamics simulation is also widely used to investigate the diffusion processes and other dynamics behavior. Comparing to Monte Carlo (MC), MD provides a deterministic method for studying the evolution of a molecular system. The diffusion of interlayer containing the cations and water molecules can be described by the mean square displacement (MSD) of species as a function of simulation time which is obtained by analyzing the motion of atoms. A large amount of relevant literature has been published, the typical result has shown in Fig. I .22 and Fig. I .23 where Fig. I .22 shows the atomic construction at initial state and the position of Na^+ and water molecules after one million time steps of simulation in an isothermal-isobaric ensemble (NPT) ensemble which means the constant number of particles, pressure and temperature. The obvious diffusion of interlayer atoms occurs. Fig. I .23 shows the relationship between mean square displacement and time. Diffusion rates are calculated using the Einstein relation for diffusion in a planar geometry, which is typical of the interlayer space of clay minerals (Frenkel and Smit, 2001), and the slope of the MSD vs time plot. It can be obtained that the diffusion rate of interlayer water of Na-MMT is much slower than bulk water, it is about 5 times. Moreover, the Na^+ is about 10 times slower than the interlayer water. The similar conclusions are respectively reported by neutron scattering experiments (Malikova et al., 2010) and modeling approaches (Bourg and Sposito, 2010; Rotenberg et al., 2007).

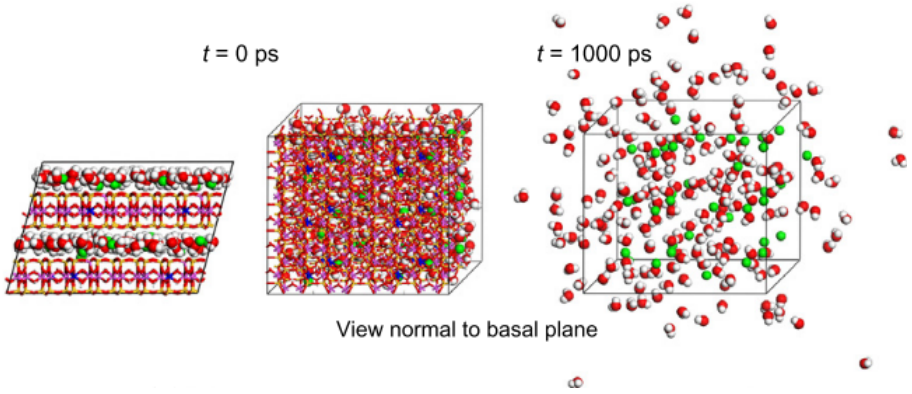

Figure I .22: Snapshots from MD simulation of Na-MMT(Greathouse and Cygan, 2013)

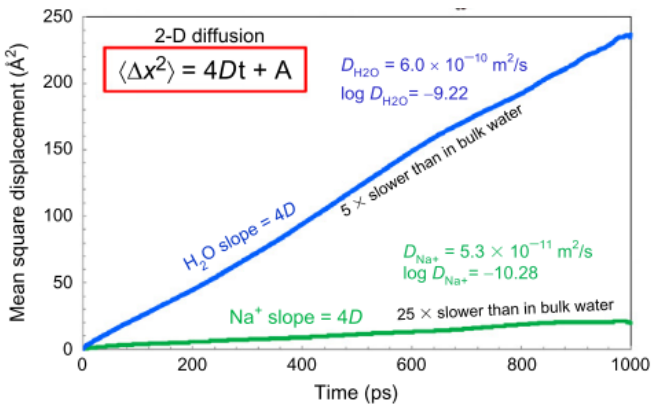

Figure I .23: The relationship between mean square displacement for water oxygen and Na^+ vs time (Greathouse and Cygan, 2013)

4.5 Adsorption of clay minerals

Recently, The adsorption of clay materials to various substances related to environmental problems was extensively investigated by MD simulations. Particularly, (Lammers et al., 2017) study the adsorption of Phthalate Esters on Smectite Clay Surfaces, a simulation snapshot of the system after adsorption containing water molecules, calcium ions, chloride ions, and phthalate molecules is shown in Fig. I .24. The adsorption and desorption of ions onto the MMT surface might be considered an equilibrium process, resulting in trends in equilibrium partition coefficients (K_D). The clay−water partition coefficients predicted by molecular dynamics simulation are greatly agree with the experimental results reported K_{oc} (organic carbon-normalized partition coefficients) value for phthalate partitioning to organic carbon in natural soil systems (Liu et al., 2013; Yang et al., 2013b;

Zhao et al., 2004). The predicted partition coefficients, furthermore, exhibit a strong correlation with K_{ow} (octanol-water partitioning coefficient) similar to trends relating K_{oc} and K_{ow} for various hydrophobic chemicals. These findings support that smectite clay minerals have a strong affinity for certain organic contaminants. The similar methods were used to investigate the adsorption of cesium on illite nanoparticles (Lammers et al., 2017), of per- and polyfluoroalkyl substances (PFASs) on smectite clay (Willemsen and Bourg, 2021). It is also used to study the structure and dynamics of water near an external muscovite surface (Wang et al., 2005), the equilibrium partitioning of aqueous cations and anions near the basal surfaces of kaolinite pore (Vasconcelos et al., 2007), the formation of electrical double layers near external smectite surfaces (Bourg and Sposito, 2011; Tournassat et al., 2009).

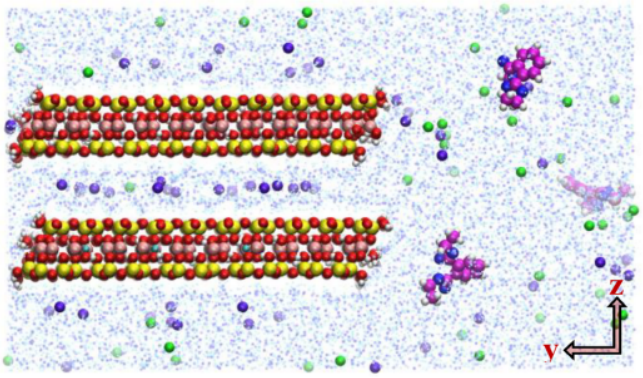

Figure I .24: Simulation snapshot of two clay sheets in a system containing water molecules (small light blue spheres), calcium ions (purple spheres), chloride ions (green spheres), and phthalate molecules (magenta, dark blue, and white spheres)(Willemsen et al., 2019)

4.6 Elastic properties of clay minerals at microscale

The rapidly development of molecular dynamics simulation strongly depend on the massively parallel supercomputers, which is used to calculate increasingly larger and more complex simulation cells. It is not rare to study the clay minerals system containing millions of atoms (Willemsen et al., 2019), this is the foundation for the study of mechanical properties of clay minerals in molecular dynamics simulation, which provide the insights at nanoscale for a deeper understanding of macroscopic deformation and failure.

Works on the mechanical properties of clay minerals with MD have been reported in stages. At the very beginning, most of the studies have focused on the elastic property of

clay minerals at dry state (Manevitch and Rutledge, 2004; SEO et al., 1999). Afterward, the elastic property of more complex systems and different conditions has been published systematically with the development of Clayff force field (Cygan et al., 2004) which takes the advantage of complete freedom and high precision description for clay minerals system. (Zhang et al., 2021b) has studied the mechanical behavior of kaolinite under uniaxial tensile and compression, the stress-strain curves along three different directions are shown in Fig. I .25. The stress-strain curves in x and y direction presents three phases, a short linear phase at the beginning of loading, it can be treated as the elastic behavior of kaolinite, the linear phase is followed by a nonlinear one until the peak stress is reached. After the peak, the stress decreases rapidly to a low values which can be treated as the failure phase. Then, the stress vibrates around a small value and eventually approaches zero. The stress-strain relationship in z direction is quite different, after the first peak, stress lowers slightly before gradually increasing to nearly the same peak stress as the first, followed by a sudden drop and remaining at a constant level of stress which illustrates the obvious anisotropy along in-plane and longitudinal orientations. In addition, the elastic constant of kaolinite are caculated and compared to the the results from theory and experiment. More precisely, the overall Young$'$ modulus obtained by MD is 72.6 GPa which has not still reported yet. However, the bulk and shear modulus of kaolinite obtained by MD are 63.96 GPa and 27.69 GPa respectively, the bulk modulus caculated by first principles is in the range of 23GPa to 67.8GPa. Shear modulus reported by first principles ranges from 19.7GPa to 36.1GPa. In addition, the Poisson's ratio is 0.311, which is very close to the experiment (Katahara, 1996) and simulated results (Sato et al., 2005; Scholtzová and Tunega, 2020; Wang et al., 2001; Weck et al., 2015; Zhao et al., 2020). These comparisons of datas provide the strong evidence for the reliability of molecular dynamics simulation. Meanwhile, the molecular dynamics simulation is also used to study the effects of different factors on elastcic characteristic of clay minerals, such as values of stress and temperature (Brochard et al., 2017; Carrier et al., 2014; Ebrahimi et al., 2012), extent of hydration (Mazo et al., 2008a,b; Suter et al., 2007), types of inter-layer cation (Carrier et al., 2014), stress orientations (Mazo et al., 2008a,b; Suter et al., 2007), different contents of CO_2 and H_2O (Zhang et al., 2015). The results show that the effect of external factors on mechanical behavior of clay minerals have obvious anisotropy due to inherent structural differences. For example, the out-of-plane coefficients were very sensitive to both temperature and water content. On the other hand, the in-plane coefficients to temperature is relatively independent. Moreover, the decrease of the in-plane coefficients with water content could be entirely explained by the change of geometry of the system due to the swelling of the

interlayer space. It's worth noting that the influences of interlayer cation on the elastic properties of montmorillonite show clearly size effect. At nano scale, the differences in elastic properties of MMT with different cations are only in the driest states (Carrier et al., 2014) while it is highly dependent on the nature of the cation at the mesoscale (Schramm and Kwak, 1982; Shomer and Mingelgrin, 1978).

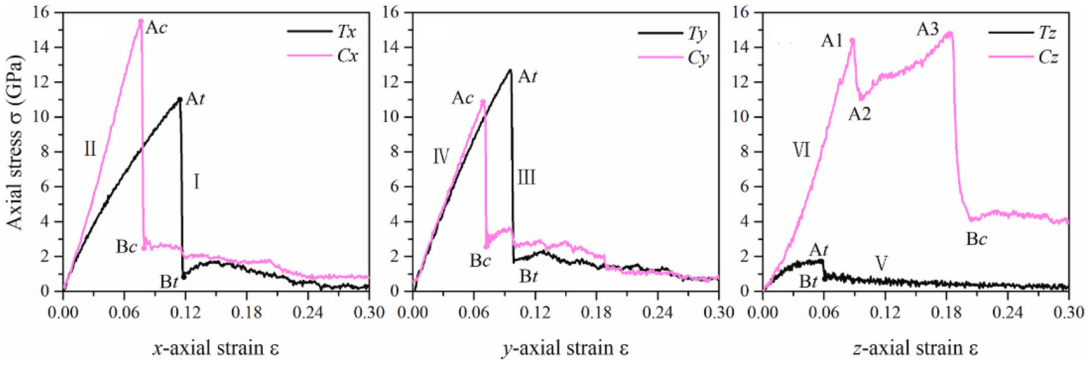

Figure I .25: Stress-strain curves under unixial tensile and unixial compression)(Zhang et al., 2021b)

4.7 Deformation characteristics and failure mechanism of clay minerals at microscale

Nowadays, deformation characteristics and failure mechanism of clay minerals and clay-based composite materials at nano scale have been paid more and more attention for deeper understanding of the macroscopic experimental phenomenons by molecular dynamics simulation and plenty of valuable insights have been obtained. At the very beginning, (Zartman et al., 2010) had roughly observed that sliding of the layers, in-plane kinks, and cation intrusion into the layers as potential failure mechanisms equal to amorphization on the macroscale. The failure strength under triaxial (uniform) stress calculated by MD is much higher than the results from macroscopic experiment (Faust and Knittle, 1994) mainly due to increased regularity, absence of defect, and smaller dimension of the probe, yet these values are only an upper bound for the true strength as the semi-empirical classical model is limited to bond deformation and does not allow bond breakage or bond rearrangements. Where after, in the work reported in (Hantal et al., 2014), the authors have proved that deformation occurred mostly in the interlayers instead of clay mineral layers themselves under uniaxial tension perpendicular to layers and shear along layers, the normalized spatial distribution of the local strain at 25% at tensile strain and

at 30% shear strain are shown in Fig. I .26. Under uniaxial tension, the interlayer space is expanded resulting in the rearrangement of hydrogen bond network and the connection between cation and clay layer, further, it is proven that the Coulombic force is more significant to contribute the mechanical strength during the tension process. Under shear loading, the stick-slip between clay layers become the main deformation characteristic which also leads to the change of interlayer structure, as it turns out the contribution of hydrogen bond network is significantly improved. This is totally consistent with the type of deformation. The similar results have been published by (Hantal et al., 2014), who exhibits that the failure mode of Illite are also related to the loading path, it mainly contains the low failure resistance under tension and the stick-slip failure under shear.

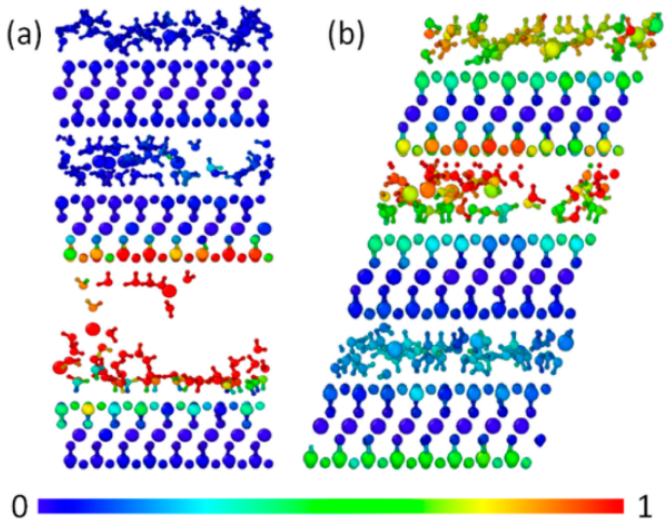

Figure I .26: (a) Normalized spatial distribution of the local strain at 25% tensile strain and (b) at 30% shear strain, with respect to the equilibrium configuration of the dye-free clay (Hantal et al., 2014).

Recently, the molecular dynamics study of mechanical properties of kaolinite under uniaxial tension and compression along three different directions by (Zhang et al., 2021b) shows that the failure mode of clay minerals is obviously anisotropic and is closely related to loading path. For tension along x and y directions, the failure mode is fractures of clay layers, the cracks generally occur where the maximum differences of atoms' displacement. Under compression, the bend and separation of clay layers becomes the main failure mode and the layers bend toward the facet of Al-O octahedral which is great agree with the recently published conclusion (Tunega and Zaoui, 2020). Along the z direction, the failure modes are quite different with other two directions, under tension, the adjacent clay layers

are easily separated just after small movements due to the weak link of hydrogen bonds but there is not obvious bend of layers. For compression, there are several stages can be observed through the changes in mode structure, the interlayer space is compressed preliminary at first, then the layer starts to slip, further compaction is until to the second failure finally. In addition, the failure strength calculated by molecular dynamics is also reported, the ultimate compressive strength is 15.49 GPa, 10.86 GPa and 14.39 GPa and the ultimate tensile strength is 11.03 GPa, 12.70 GPa and 1.81 GPa respectively in x, y, z direction, which is consistent with the value from (Yang et al., 2019), however, the atomic-scale compressive strengths of clay minerals have not yet reported by experiments and theory, so it can only be considered as a prediction.

4.7.1 Inter-facial mechanical behavior of clay minerals based material

With the deep understanding of practical engineering problems and growing requirement of high performance materials in engineering application, the composite materials, such as clay-water, bitumen-mineral, clay–bio and so on, have become a great scientific and technological interest. In general, the interface, as the weak link zone, determined the mechanical strength of composite materials. Based on this, the interface connection and interactions between two different materials have attracted the focus of researchers and been carried out numerous (Peng-Fei et al., 2021) and experiments (Liu et al., 2021; Peng-Fei et al., 2021) studies. Certainly, the molecular dynamics (MD) simulation, as the effective method to explore the interaction mechanism at atomic scale, have been successfully used to investigate the deformation and failure mechanisms occurring in the inter-facial of complex composite systems (Chatterjee et al., 2021; Delville, 1993; Gao et al., 2018, 2019; Lai et al., 2018; Liu et al., 2020b; Wang et al., 2020, 2015b, 2014). The present studies have shown the mechanical performance is strongly influenced by the inter-facial adhesion which is a common measure to characterize inter-facial properties, it's defined as the reversible work needed to pull the adsorbate off the clay surface. (Chatterjee et al., 2021) has investigated the molecular adhesion of nano-composites made up of montmorillonite clay-polysaccharide xyloglucanat with different counterions at high relative humidity. The results have been suggested that the interlayer cations play a key role in the interlayer properties, the difference is closely related to the hydration extent. The weaker hydration makes water molecules more easily displaced from the interface, which indirectly affects the adhesion of polymer to the surface. This conclusion may be extended to other nanocomposite systems as well. In addition, existing other researches suggest that surface nanostructures, mineral type, water content are also the key factors

to the interfacial adhesion and thus the mechanical properties (Gao et al., 2018, 2019; Lai et al., 2018). Although the Pull-off test predicts the interaction and debonding behavior of the interface, the nanoscale surface behavior is not only based on the adhesive, the interface frictional performance is another essential impact on controlling mechanical strength. To the best of our knowledge, although molecular dynamics is widely used to study friction properties, it is mainly focused on graphene, metal and other materials, there are relatively few studies on the clay minerals. For instance, (Yue et al., 2013) has reported that the friction coefficient is strong positive effected by the number of interfacial hydrogen bonds, a weaker interfacial hydrogen bond network would favor a lower friction through the exploration of friction properties of interface between quartz and phosphoric acid by molecular dynamics simulation, the figure of friction coefficient, hydrogen bond number as a function of temperature is shown in Fig. I .26.

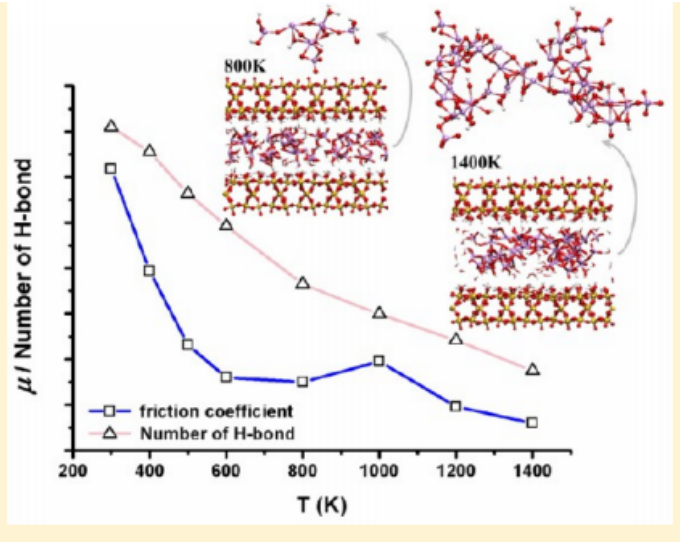

Figure I .27: (a) Normalized spatial distribution of the local strain at 25% tensile strain and (b) at 30% shear strain, with respect to the equilibrium configuration of the dye-free clay (Yue et al., 2013).

In addition, the mechanism of friction coefficient reduction varies with temperature. At relatively low temperatures, such as 300k to 600k, the friction coefficient decreases due to the accelerated molecular rotational and translation motion and the corresponding weakened hydrogen bond network. When the temperature is in the range of 800k to 1400k, the main reason for the decrease of friction coefficient is that the clustering and polymerization of the phosphoric acid molecules because of tribochemical reactions, generating a large number of water molecules in the sliding interface acting as lubricant.

Besides, recent advanced research published by (Liu et al., 2020a) has shown a result that overturned the classical law of friction, which concluded negative friction coefficient in microscale monocrystalline heterojunctions at different temperatures. The molecular dynamics simulation reveals that this is because the synergetic and nontrivial redistribution of water molecules at the interface, causing to larger density and more ordered structure of the confined subnanometer-thick water film. Therefore, the friction shows a negative dependence on normal load. Besides, the relationship between the average friction load and the sliding velocity, normal force of hydrated montmorillonite are studied by Wei et al. (2021), who concluded that a power function describes the relationship between average friction and sliding velocity.

Chapter II

Assessment of deformation and failure of dry clay-rich rocks in compression and extension

1 Introduction

Clay-rich rocks have been widely investigated in geological issues and engineering practices. For instance, shale rocks constitute the main reservoir or cap layers in unconventional hydrocarbon exploration. Hard claystone and swelling clay are used as geological and engineered barriers for the underground storage of radioactive wastes (Armand et al., 2013). Clayey rocks are characterized by complex mineralogical compositions and multi-scale structures (Abedi et al., 2016; Bennett et al., 2015; Robinet et al., 2012). At the atomistic scale, clay sheets are organized in layer crystals (particles) (Carrier et al., 2014). Clay particles are further structured in clay aggregates with inter-particles voids (Robinet et al., 2012) at nanometer scale. At micrometer scale, clay aggregates constituent a porous clay matrix. Mineral and organic grains, such as quartz, carbonate and kerogen, are embedded inside the clayey matrix.

Macroscopic mechanical behaviors of clayey rocks are controlled by the local mechanical properties of constituents and their interactions at the different scales. In particular, clay particles play a dominant role on macroscopic deformation and failure process of clay-rich rocks. For instance, macroscopic plastic deformation is mainly driven by the local deformation mechanisms of clay particles and aggregates at the nanometer and micrometer scales (Bornert et al., 2010; Wang et al., 2015a). It is assumed that macroscopic time-dependent deformation of clay-rich rocks is also related to the local motion of clay particles

(Armand et al., 2017; Liu et al., 2018c). Further, as the mechanical behavior of clay particles at the atomistic and microscopic scales depends on water content in inter-layer space and inter-particle voids, the macroscopic mechanical behavior of clay-rich rocks is also strongly sensitive to water saturation degree (Chiarelli et al., 2003; Liu and Shao, 2016b; Vales et al., 2004; Zeng et al., 2019; Zhang et al., 2012). The molecular dynamic motion is also influenced by temperature leading to the thermal effect on macroscopic mechanical properties (Liu et al., 2019a; Zhang, 2018). Moreover, the layered structure of clay crystals at the nanometer scale can be one of origins for strongly anisotropic mechanical behaviors of clay-rich rocks (Armand et al., 2017; Liu et al., 2015b; Niandou et al., 1997; Zhang et al., 2019). Therefore, the characterization of mechanical behaviors of clayey rocks should be based on multi-scale approaches in order to properly take into account influences of mineralogical compositions and multi-scale heterogeneity. Understanding of deformation and failure mechanisms of clay particles at the atomistic scale is an essential task. However, it is very difficult to perform direct experimental measurement at such small scales in view of identifying those mechanisms. Appropriate numerical calculations provide alternative solutions. In this context, molecular dynamics simulations (MD) have been rapidly developed and widely used in modeling the clay-rich materials at different scale.

MD simulations were first applied to studying hydration related swelling behavior, structure distribution, diffusion of water molecules or cation ions between layers (Boek et al., 1995b; Shroll and Smith, 1999; Underwood and Bourg, 2020; Yeh and Hummer, 2004). Afterward, works on the mechanical property of clay minerals with MD have been reported in stages. At the very beginning, most of the studies have focused on the elastic property of clay particles under different conditions, such as different values of stress and temperature (Brochard et al., 2017; Ebrahimi et al., 2012), extent of hydration (Mazo et al., 2008a,b; Suter et al., 2007), types of inter-layer cation (Carrier et al., 2014), stress orientations (Mazo et al., 2008a,b; Suter et al., 2007), different contents of CO_2 and H_2O(Zhang et al., 2015). Nowadays, the failure property and mechanism become important topics. For instance in (Zartman et al., 2010), the authors have suggested roughly that sliding of layers, in-plane kinks, and cation intrusion into layers can be the potential failure mechanisms of clay. In (Duque-Redondo et al., 2014) it has been shown that the failure was mainly due to decohesion of inter-layer space under uniaxial tension perpendicular to layers and to stick-slip between clay layers under shear loading. In the work reported in (Hantal et al., 2014), the authors have proved that the mechanical performance of clay hybrid material under uniaxial tension perpendicular to layers and

shear along layers was dependent only on the cohesion between layers, while the layers themselves do not participate in the failure mechanism. The Coulombic force was more significant when a tensile strain was applied, while the hydrogen bonding became relevant under shear loading. In (Faisal et al., 2020), it has been stated that the hierarchical structure of Na-Mt clay mineral was composed of four relevant levels: unit clay mineral layer, tactoid, aggregate, multiple aggregate. The mechanical response of Na-Mt tactoid was evaluated under compression, tension and shear. All the previous studies mentioned above have shown that the mechanical behavior of clay exhibited an anisotropic behavior because of the internal structure and the failure process was influenced by the loading path.

However, in most previous studies, MD simulations were performed on crystal samples subjected to very simple loading paths, for instance, uniaxial compression or tension, triaxial compression with constant confining stress. However, most geological materials can be subjected to other types of loading paths. From a practical point of view, for example in the case of underground cavity excavation, two loading paths are particularly relevant (Liu et al., 2019a). In the first path here called triaxial decompression, starting from initial in-situ stress state, one principal stress is increased in compression while two others are decreased the way the mean stress remains constant. In the second path called triaxial extension, one compressive principal stress is relaxed and two other ones are increased by keeping the mean stress at a constant value. The comparison between these loading paths allow studying the effect of third stress invariant (or Lode's angle) on mechanical behavior. Indeed, it has been found that mechanical behaviors of most geological materials were generally different along these two loading paths (Liu et al., 2019c). On the other hand, the influence of loading path should also be coupled with loading orientation for anisotropic materials such as clay-rich rocks. Therefore, the effects of loading path and orientation should be investigated together. To the best of our knowledge, these important features have so far not been investigated on atomistic modeling of mechanical behavior of MMT particles. In this study, we shall perform MD simulations on a typical Na-montmorillonite (NaMMT) crystal structure by considering the triaxial compression and extension with different values of mean stress. Further, the compression and extension will be applied respectively to the parallel and perpendicular directions with respect to crystal layers. The main objective here is to identify the basic mechanisms of deformation and failure at the atomistic scale and then to establish some links between microscopic (single NaMMT crystals) and macroscopic (clayey rocks) behaviors. However, there is no pretension in this study to develop a multi-scale modeling of macroscopic mechanical properties of clayey

rocks, which are influenced by complex heterogeneity (voids, mineral phases) at different scale. It is only focused at studying deformation and failure properties of one of principal constituent (clay minerals) of clayey rocks at the atomistic scale. The results obtained from MD simulations can be used for the first step of multi-scale bottom-up modeling of clayey rocks. Further, among various factors influencing mechanical behaviors of NaMMT particles such as stress state, hydration and temperature, the emphasis of the present work is put on the effects of loading path and orientation as well as mean stress. Effects of hydration and temperature on deformation and failure properties of NaMMT are investigated in other studies.

2 Computational method

Molecular dynamics (MD) is adopted here as computational method. Like most previous studies on MD simulations, atoms are considered as basic particles. The atomistic movement is described by Newton equations of motion, and the forces acting on the atoms are driven by inter-atomic potentials (force fields) which contains bonded and non-bonded interactions. In this section, the different steps of MD simulations performed in this study are first presented.

2.1 Crystal structure

The crystal structure considered here is based on the natural Wyoming MMT (Boek et al., 1995a,b; Chang et al., 1995). The unit cell formula is as follows:

$$Na_{0.75}nH_2O[Si_{7.75}Al_{0.25}][Al_{3.5}Mg_{0.5}]O_{20}(OH)_4. \quad \text{(II .1)}$$

The space group of unit cell is C2/M, monoclinic system, with a=5.23A, b=9.06A, c=9.6A, $\alpha = \gamma$=90° and β=99°. It is characterized by sheets of silica tetrahedra and alumina octahedra that coordinate to form a TOT (tetrahedron-octahedron-tetrahedron) layer. The layer is negatively charged by the aliovalent substitution of Mg^{2+} for Al^{3+} in the octahedral sheet and of Al^{3+} for Si^{4+} in the tetrahedron sheet. Specifically, one of thirty-two Si^{4+} is replaced by Al^{3+} and one of eight Al^{3+} is replaced by an Mg^{2+}. This process is called the isomorphous substitution. The negative charge is balanced by the incorporation of Na cations in the inter-layer space. The model used in this study is an 8*4*4 super-cell. The failed crystal structure is shown in Figure II .1.

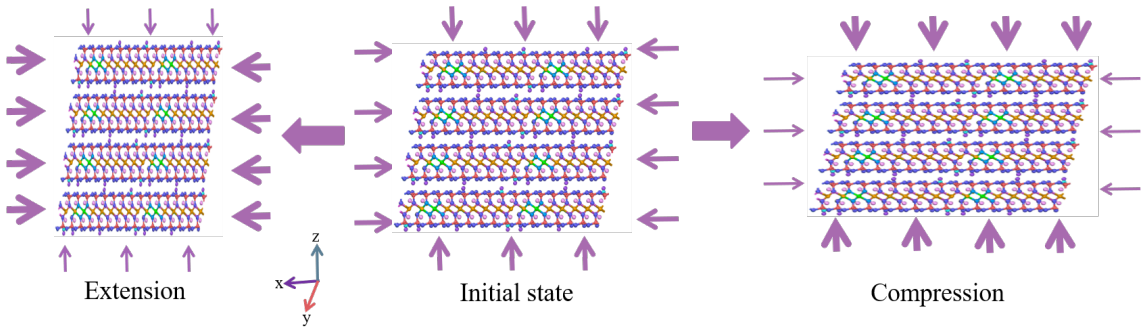

Figure II .1: Crystal structure of MMT and definition of compression and extension loading along z-axis

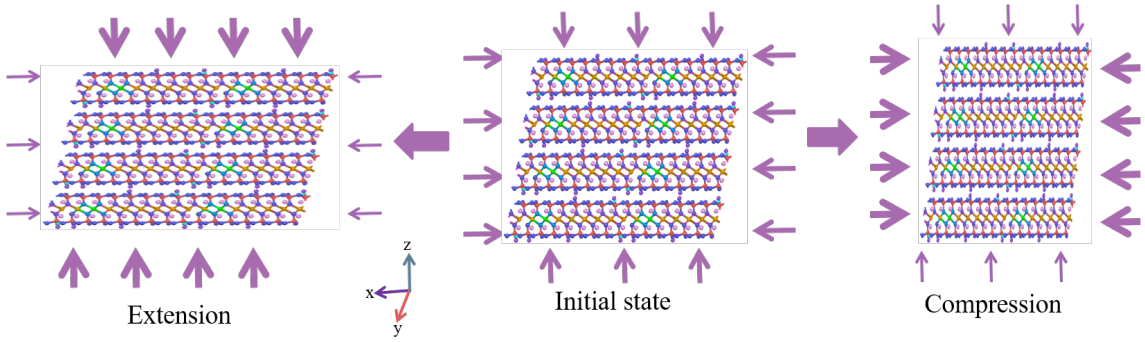

Figure II .2: Crystal structure of MMT and definition of compression and extension loading along x-axis

2.2 Force filed

The inter-atomic interactions in crystal systems are described by forces fields which are derived from energy potential functions. In the present study, the CLAYFF force field developed by (Cygan et al., 2004) is adopted. This force field is mainly based on an non-bonded description of inter-atomic interactions consisting solely of electrostatic and Lennard-Jones terms except for the O-H bond, which is constrained by a harmonic bond stretch potential. In the last few decades, the CLAYFF force field has been shown to be highly effective in modeling the crystal structure of a number of different clays (Cygan et al., 2004; Leng and Cummings, 2006; Porion et al., 2007; Suter et al., 2007; Wang et al., 2005), mobility of interlayer water (Kalinichev et al., 2007; Leng and Cummings, 2006; Porion et al., 2007; Suter et al., 2007; Wang et al., 2005) because of the huge advantage

of providing atoms with complete translation freedom. Recently, it has also widely used to study the mechanical behavior of clay and contributed to the understanding of the basic mechanical mechanisms from atomic level (Carrier et al., 2014; Cygan et al., 2004; Ebrahimi et al., 2012; Manevitch and Rutledge, 2004; Mazo et al., 2008a; Suter et al., 2007; Zhang et al., 2015). Besides, the effectiveness of CLAYFF force field in the study of mechanical properties of clay minerals was evaluated through the comparison of simulation and experimental results by some researchers (Teich-McGoldrick et al., 2012). The total potential energy (E_{total}) is composed of the Coulombic interactions (E_{Coul}), the van der Waals interactions (E_{VDW}) and the bonded interactions. The bonded terms include the bond stretch energy ($E_{bond\ strech}$) and the angle bend energy ($E_{angle\ bend}$) that is used in water and metal with hydroxyl. One gets:

$$\begin{cases} E_{total} = E_{Coul} + E_{VDW} + E_{bond-strech} + E_{angle-bend} \\ E_{Coul} = e^2/4\pi\epsilon_0 \sum_{i\neq j} q_i q_j / r_{ij} \\ E_{VDW} = \sum_{i\neq j} D_{0,ij}[(R_{0,ij}/r_{ij})^{12} - 2(R_{0,ij}/r_{ij})^6] \\ E_{bond-strech} = k_1(r_{ij} - r_0)^2 \\ E_{angle-bend} = k_2(\theta_{ijk} - \theta_0)^2 \end{cases} \quad \text{(II .2)}$$

r_{ij} is the distance between the atoms i and j. In the Coulombic energy, e is the charge of an electron, ϵ_0 is the dielectric permittivity of a vacuum ($8.85419 \times 10^{12} F/m$) and q_i and q_j are the atomic partial charges, which can be derived from quantum mechanics calculations. In the Van der Waals energy, the terms $D_{0,ij}$ and $R_{0,ij}$ are calculated by:

$$\begin{cases} R_{0,ij} = 1/2(R_{0,i} + R_{0,j}) \\ D_{0,ij} = (D_{0,i} * D_{0,j})1/2 \end{cases} \quad \text{(II .3)}$$

About the $(O-H)$ bond stretch energy, k_1 defines a force constant and r_0 represents the equilibrium bond length. Finally for the angle bend energy, k_2 is a force constant, θ_{ijk} denotes the bond angle for the mental-oxygen-hydrogen and θ_0 is the equilibrium bond angle. The values of parameters involved in the different forces are given in Tables II .1, II .2 and II .3 respectively.

Table II .1: Non-bond energy parameters for the CLAYFF force field

species	symbol	charge (e)	D_0(kcal/mol)	R_0(Å)
tetrahedral silicon	st	2.1000	1.8405×10^{-6}	3.7064
bridging oxygen	ob	-1.055	0.1554	3.5532
bridging oxygen with octahedral substitution	obos	-1.1808	0.1554	3.5532
octahedral aluminum	ao	1.5750	1.3298×10^{-6}	4.7943
hydroxyl oxygen	oh	-0.9500	0.1554	3.5532
hydroxyl hydrogen	ho	0.4250		
hydroxyl oxygen with substitution	ohs	-1.0808	0.1554	3.5532
octahedral magnesium	mgo	1.3600	9.0298×10^{-7}	5.9090
aqueous sodium ion	Na	1.0000	0.1301×10^{-6}	2.6378
bridging oxygen with tetrahedral substitution	obts	-1.1688	0.1554	3.5532
tetrahedral aluminum	at	1.5750	1.8405×10^{-6}	3.7064

Table II .2: Bond stretch energy parameters for the CLAYFF force field

species i	species j	k_1(kcal/mol Å^2)	r_0(Å)
oh	ho	554.1349	1.000
ohs	ho	554.1349	1.000

Table II .3: Angle bend energy parameters for the CLAYFF force field

species i	species j	species k	k_2(kcal/mol rad^2)	θ_0(deg)
Metal	oh	ho	30.0	109.47
Metak	ohs	ho	30.0	109.47

2.3 MD simulation procedure

A parallel molecular dynamics code Lammps (Plimpton, 1993) is used to perform simulations on the crystal structure of Na-Montmorillonite defined above. The samples are first relaxed at the desired temperature using an NVT (conserving the number of atoms, volume, and temperature) ensemble for 200 ps followed by an independent relaxation in three directions using an NPT (conserving the number of atoms, pressure, and temperature to mimic bulk behavior) ensemble for another 200 ps with zero pressure in all the directions. These relaxation steps are performed to uniformly distribute the excess free energy through the whole system.

Mechanical loads are then applied to the samples and their deformations are calculated. As mentioned above, mechanical responses of clayey rocks clearly depend on loading paths. Two representative loading paths are here considered: triaxial compression and extension, as shown in Figure II .1. For both loading paths, a hydrostatic compressive mean stress is first applied in three principal directions of the crystal sample. Then, after the stabilization of strains under the mean stress, in the compression loading, one of three principal stresses is further increased (called the axial stress and denoted as $\sigma_a > 0$) while the other others are decreased (called the radial stress and denoted as $\sigma_r < 0$) so that the value of mean stress remains unchanged $(\Delta\sigma_a + 2\Delta\sigma_r) = 0$. For the extension loading, the axial principal stress is relaxed ($\sigma_a < 0$) from the initial value while the radial stress is increased ($\sigma_r > 0$) so that the mean stress is kept constant $(\Delta\sigma_a + 2\Delta\sigma_r) = 0$. In this study, four different values of mean stress are considered, namely σ_m=5, 10, 15, 20 GPa. The increase or decrease of the axial stress is proceeded at the rate 10MPa/fs while that of the radial stress at the rate 5MPa/fs according to the Parrinello-Rahman method under the given temperature which is controlled by the Nose-Hoover thermostat. All simulations are run until failure of sample. All simulations are carried out using an MD time step of 0.01 fs. A periodic boundary condition is adopted in all directions. It is worth noticing that the values of mean stress used here are much higher than those usually considered in macroscopic tests on clayey rocks. Indeed, due to its strong order and very small inter-layer pore, the

single NaMMT crystal is much stiffer than macroscopic samples. Therefore, in order to facilitate the investigation of deformation and failure of such a single crystal, high values of stresses are generally adopted in most MD simulations, for instance on NaMMT particles (Schmidt et al., 2005; Thapa et al., 2020). Similar values are adopted in this study for mean stress. As a consequence, results obtained from MD simulations on NaMMT crystal are mainly used to investigate atomistic physical origins of some macroscopic properties and to identify links between microscopic and macroscopic behaviors.

Moreover, in order to investigate the anisotropic responses of MMT crystal, both the compression and extension paths are applied respectively the parallel (x-axis) and perpendicular (z-axis) directions to the crystal layers. The detailed description of loading paths are presented in the supplementary file. Finally, all MD simulations presented in this study are performed with a constant temperature of $T = 300K$.

3 Basic mechanical behavior and discussions

In this section, the basic mechanical behavior of NaMMT crystal samples is first presented through the results obtained from MD simulations. We shall then investigate effects of loading path, crystal structure anisotropy, mean stress on overall stress-strain responses. It is worth noticing that different types of phenomenological and micro-mechanical constitutive models have been proposed for the description of elastic-plastic and damage behaviors of clayey rocks the effects mentioned here, for instance (Hoxha et al., 2007; Shao et al., 2006; Shen et al., 2013; Shen and Shao, 2015). However, all those models are inspired or calibrated from macroscopic experimental results. As basic differences with these models, MD simulations are entirely based on the motion of crystal systems. Mechanical behaviors are predicted by solving fundamental motion equations without any a priori assumptions. On the other hand, contrary to classical constitutive models, MD modeling is at this stage devoted to engineering structure calculations but to analyze different physical mechanisms of deformation and failure at small scales.

3.1 Basic stress-strain response

As example, the stress-strain curves for a mean stress of $\sigma_m = 20GPa$ are selected and shown in Figures II .3, when the axial stress is along x-axis and z-axis respectively. By using conventional rock mechanics notation, axial (ϵ_a) and radial (ϵ_r) strains are plotted versus differential stress $q = \sigma_a - \sigma_r$.

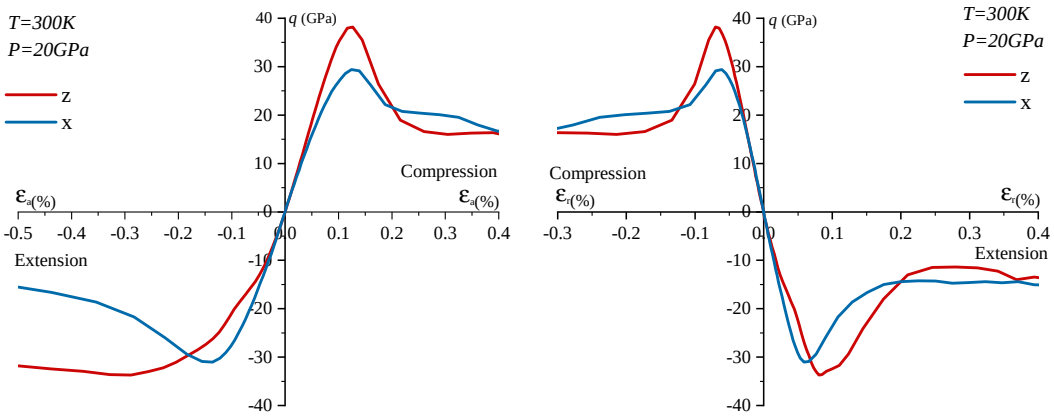

(a) Differential stress - axial strain (b) Differential stress - radial strain

Figure II .3: Typical stress-strain curves in compression and extension (T=300K, σ_m=20 GPa)

From these Figures, one can see that the basic mechanical behavior of MMT in both compression and extension is characterized by strongly nonlinear stress-strain curves. There is a short linear phase at the beginning of loading. This phase can represent the elastic behavior of MMT. The linear phase is followed by a nonlinear one with increasing axial and radial strain until the peak differential stress is reached. This nonlinear phase corresponds to plastic deformation of crystal sample. The peak differential stress characterizes the maximum mechanical strength for a given loading condition. Starting from the stress value around the peak strength, the internal crystal bonds are progressively damaged, leading to the reduction of their mechanical strength. As a consequence, one gets the material softening behavior in the post-peak regime. Moreover, the plastic deformation is inherently coupled with the damage of crystal bonds. When the strain becomes large enough, a residual strength of material can be obtained and it is due to the forces in the remaining crystal bonds. It is interesting to notice that the basic mechanical behaviors obtained at the atomistic scale are qualitatively very similar to those observed on various clayey rocks (Armand et al., 2017; Chiarelli et al., 2003; Liu and Shao, 2016b; Vales et al., 2004; Zeng et al., 2019; Zhang et al., 2012), for instance elastic and plastic deformation as well as induced damage. However, as mentioned above, the order of magnitude of stresses is much higher, while that strain is lower, at the atomistic scale than that at the macroscopic scale. Therefore, the objective here is to investigate relationships between microscopic mechanisms and macroscopic properties, but not to make quantitative comparisons. Indeed, for a same loading path, the macroscopic strength of clayey rocks is

generally significantly lower than that of MMT crystal at the atomistic scale. This difference can be basically explained by strong multi-scale heterogeneity effects. Clayey rocks are heterogeneous composites containing voids and mineral phases at different scales. In particular, inter-particular voids and interfaces should play a strong weakening effect in macroscopic strength properties. The local responses of clay minerals affect only partially the overall behaviors of clayey rocks.

3.2 Effect of loading path

For a quantitative comparison between compression and extension, the peak values of axial stress (σ_a), radial stress (σ_r) and differential stress obtained in compression and extension under 300k are given in Table II .4. It is worth noticing that the basic difference between these two loading paths lies on the value of Lode angle defined on the octahedral plane for a given value of mean stress or equivalently the third stress invariant. Indeed, the Lode angle is equal to $\theta_\sigma = -30^\circ$ for compression and $\theta_\sigma = 30^\circ$ for extension.

Table II .4: Peak values of axial stress, radial stress and differential stress in compression and extension and along x-axis and z-axis (T=300K)

	σ_m	x-axis			z-axis		
		σ_a	σ_r	q	σ_a	σ_r	q
Compression	5	22.22	-2.52	24.74	28.05	-6.41	34.46
	10	29.42	0.35	29.06	34.27	-2.03	36.30
	15	34.69	5.11	29.57	40.33	2.32	38.00
	20	39.55	10.14	29.41	45.42	7.23	38.19
Extension	5	-11.32	13.26	-24.59	-1.09	10.98	-12.06
	10	-7.74	19.03	-26.77	-0.50	20.07	-20.58
	15	-4.64	24.94	-29.58	-0.05	28.11	-28.16
	20	-0.60	30.42	-31.03	-1.77	31.91	-33.69

From the date obtained, a number of significant remarks can be drawn. When the axial stress is applied along z-axis (perpendicular to crystal layers), the absolute values

of peak differential stress are systematically higher in compression than in extension for all selected values of mean stress σ_m. However, the difference between compression and extension becomes smaller when the mean stress is higher. This means that dissymmetry of peak strength between these two loading paths is progressively attenuated by the increase of mean stress. In the three-dimensional stress space, the strength surface in the octahedral plane approaches a circular lotus when the mean stress is high enough. This kind of result agrees well with macroscopic experimental results obtained on most rocks as mentioned above. When the axial stress is parallel to x-axis, the absolute value of peak stress in compression is also higher than that in extension for three low values of mean stress. But the difference between compression and extension is significantly reduced from σ_3=5 GPa to σ_3=15 GPa. For the case of σ_3=20 GPa, the peak strength in extension even becomes higher than that in compression. This particular result will be further discussed later in relation with the failure process of MMT crystal structure. In a general way, it is worth noticing that the dependency of failure strength on loading path observed at the atomistic scale is qualitatively consistent with few macroscopic results obtained on clayey rocks samples (Liu et al., 2019a). Therefore, it seems that in spite of many other factors affecting macroscopic behaviors of clayey rocks, the stress-path dependency of their macroscopic strength have some origins at the atomistic scale.

3.3 Effect of loading orientation

Based on the peak values of stresses given in Table II .4 and the overall stress-strain responses obtained from performed calculations, the effect of loading orientation with respect to the crustal layers is here further discussed. For this purpose, we compare here the stress-strain curves between compression and extension for two values of mean stress (σ_m=20 GPa, σ_m=10 GPa), as shown in Figure II .4 and II .5.

From these results, it is found that during the short linear stage at the beginning of differential stress loading for both compression and extension paths, the mechanical behavior of MMT crystal is almost identical in the two loading orientations. It seems that the elastic properties of MMT crystal are quasi isotropic. However, one can observe important differences of mechanical responses during the plastic phase and in the post-peak regime. For compression loading, the plastic deformation is smaller but the peak strength is higher in z-axis than in x-axis. Further, the mechanical behavior in z-axis is more brittle than in x-axis in the post-peak regime by showing a faster decrease of differential stress. However, the asymptotic residual strength is almost the same for the two loading orientation. In contrary, for the extension loading, the plastic deformation

is clearly more important in z-axis than in x-axis. At the same time, the MMT shows a more ductile behavior in the post-peak regime in z-axis than in x-axis. The difference of peak differential stress between the two loading orientations depends on the values of mean stress. It seems that the peak strength in z-axis is higher than in x-axis for different values of mean stress (σ_m=10 GPa, σ_m=20 GPa).

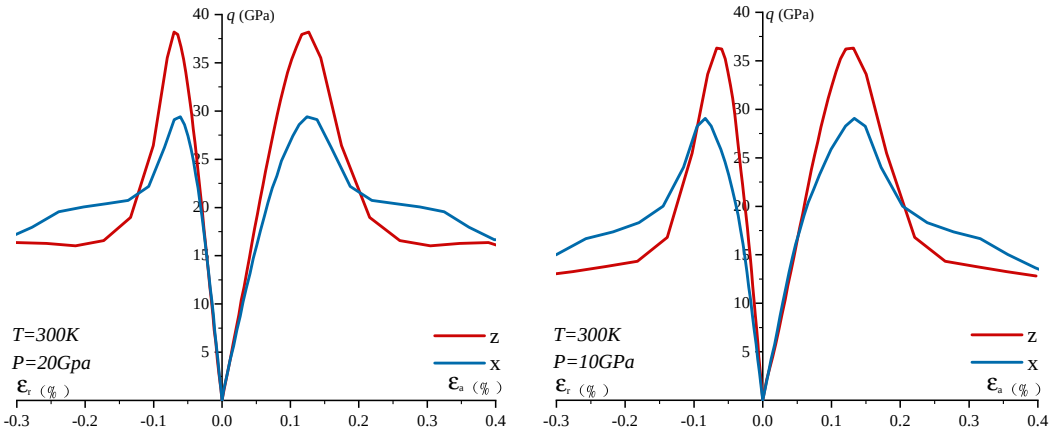

(a) Compression - axial and radial strains (b) Compression - axial and radial strains

Figure II .4: Comparison of stress-strain curves in compression between two loading orientations

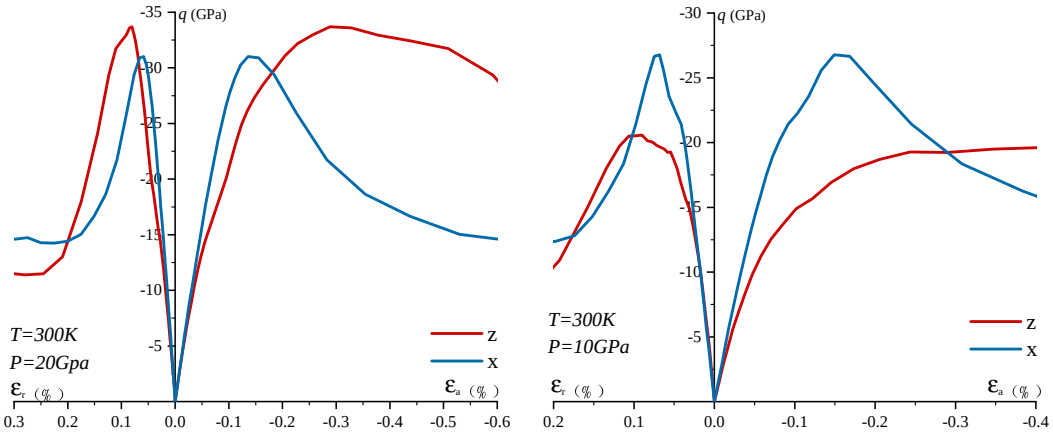

(a) Extension - axial and radial strains (b) Extension - axial and radial strains

Figure II .5: Comparison of stress-strain curves in extension between two loading orientations

It is worth noticing that z-axis is perpendicular to crystal layers while x-axis is par-

allel to them. Therefore, the difference of mechanical behavior between the two loading orientations is inherently related to different deformation and damage processes at the atomistic scale. More detailed discussions are presented in Section 4. It is interesting to point out that the strength anisotropy obtained at the atomistic scale is consistent with the macroscopic one observed in clayey rocks (Armand et al., 2017; Liu et al., 2015b; Niandou et al., 1997; Zhang et al., 2019). It seems that the macroscopic strength anisotropy of clayey rocks is partially due to the layered structures of clay particles. However, it is noticed that the microscopic anisotropy is stronger than the macroscopic one. Such a difference can be explained by the fact that clayey rocks are multi-scale poly-crystalline materials. Random distribution of clay particles and other mineral phases can attenuate the macroscopic anisotropy of materials.

3.4 Effect of mean stress

The mechanical behavior of geological materials is generally dependent on mean stress. This basic property is here verified at the atomistic scale on the MMT crystal. For this purpose, four values of mean stress are selected, ranging from 5 MPa to 20 MPa. The stress-strain curves obtained from compression and extension and in both loading orientations are here compared and presented in Figures II .6 and II .7. In a general way, little difference is observed on the initial slopes of stress-strain curves for almost all cases. That indicates that the elastic properties of the MMT crystal are almost independent on mean stress. But mean stress strongly affect plastic deformation and failure strength. For compression in x-axis, larger plastic deformation is developed and the peak strength is lower when mean stress is smaller. But the mean stress dependency of peak strength is clearly nonlinear. Indeed, the dependence of peak strength on mean stress is significantly attenuated when mean stress is higher than 10 MPa. The post-peak behavior is more brittle and the residual strength is lower when mean stress is smaller. The mechanical behavior during extension in x-axis shows a much more regular dependency on mean stress than in compression. The plastic deformation increases and the peak and residual strengths decrease when mean stress becomes smaller. The influence of mean stress on the mechanical response in compression along z-axis is qualitatively similar to that in x-axis. Among all cases, the most important effect of mean stress is found on the mechanical responses in extension along z-axis. The peak strength shows a very important increase when mean stress varies from 5 GPa to 20 GPa. Further, for the three low values of mean stress (5, 10, 15 GPa), very large axial plastic strains are obtained and one observes a typical ductile behavior. At the same time, the radial strains remain significantly smaller

than axial ones. For the case of high mean stress (20 GPa), the post-peak behavior is characterized by three different phases: a first phase of slow decrease of differential stress, a second phase with rapid decrease of differential stress, and a third phase marking the residual strength. This atomistic effect of mean stress is quite different with classical brittle-ductile transition of rocks with increasing mean stress at the macroscopic scale. It seems that mean stress can play an essential role on plastic deformation and failure process of clay crystals at the atomistic scale. Again, the dependence of mechanical behavior on mean stress of the NaMMT crystal, in particular the increase of failure strength with mean stress, is also very consistent with macroscopic results obtained on various clayey rocks (Armand et al., 2017; Chiarelli et al., 2003; Liu et al., 2019a; Zhang et al., 2019). Again, there is a clear link between the microscopic and macroscopic behaviors in terms of mean stress effects.

On the other hand, in Figures II .6 and II .7, the variations of volumetric strain are also presented. It is interesting to see that in a general way, there is a clear transition from volumetric compaction to dilation when the differential stress is increased. The volumetric dilatancy increases very quickly in the post-peak regime. There is thus a clear correlation between volumetric dilatancy and crystal structure damage. For compression in x-axis (parallel to crystal layers), the volumetric dilatancy is higher when the mean stress is lower because the expansion of inter-layer space is prevented by compressive mean stress. For extension in x-axis, the volumetric dilatancy is smaller when the mean stress is lower but its effect is less significant. For these two cases, the volumetric strain remains very small before the peak strength is reached. This is due to the fact that the deformation before the peak strength is essentially elastic and the mean stress is kept constant. For compression in z-axis (perpendicular to crystal layers), the volumetric strain is clearly compressive before the peak strength is reached and then turns into dilating in the post-peak region. This is clearly a consequence of compaction of inter-layer space along the z-axis. For extension in z-axis, nearly no volumetric compaction is obtained even before the peak strength. The volumetric dilatancy is significantly enhanced by low values of mean stress, and it is clearly correlated with the expansion of inter-layer space. Therefore, the evolution of volumetric strain of clay particle is significantly influenced by loading path and orientation as well as mean stress. These atomistic results on NaMMT particle are in good consistency with macroscopic responses of most clayey rocks, in particular under low values of mean stress (Armand et al., 2017; Chiarelli et al., 2003; Liu et al., 2019a; Zhang et al., 2019). However, the macroscopic volumetric deformation of clayey rocks is not only influenced by clay particles, but also by many other factors such compaction or expansion

of multi-scale voids, opening or closure of interfaces between mineral inclusions and clay matrix. As a consequence, it is noticed that the macroscopic volumetric dilatancy is less pronounced than that of NaMMT crystals.

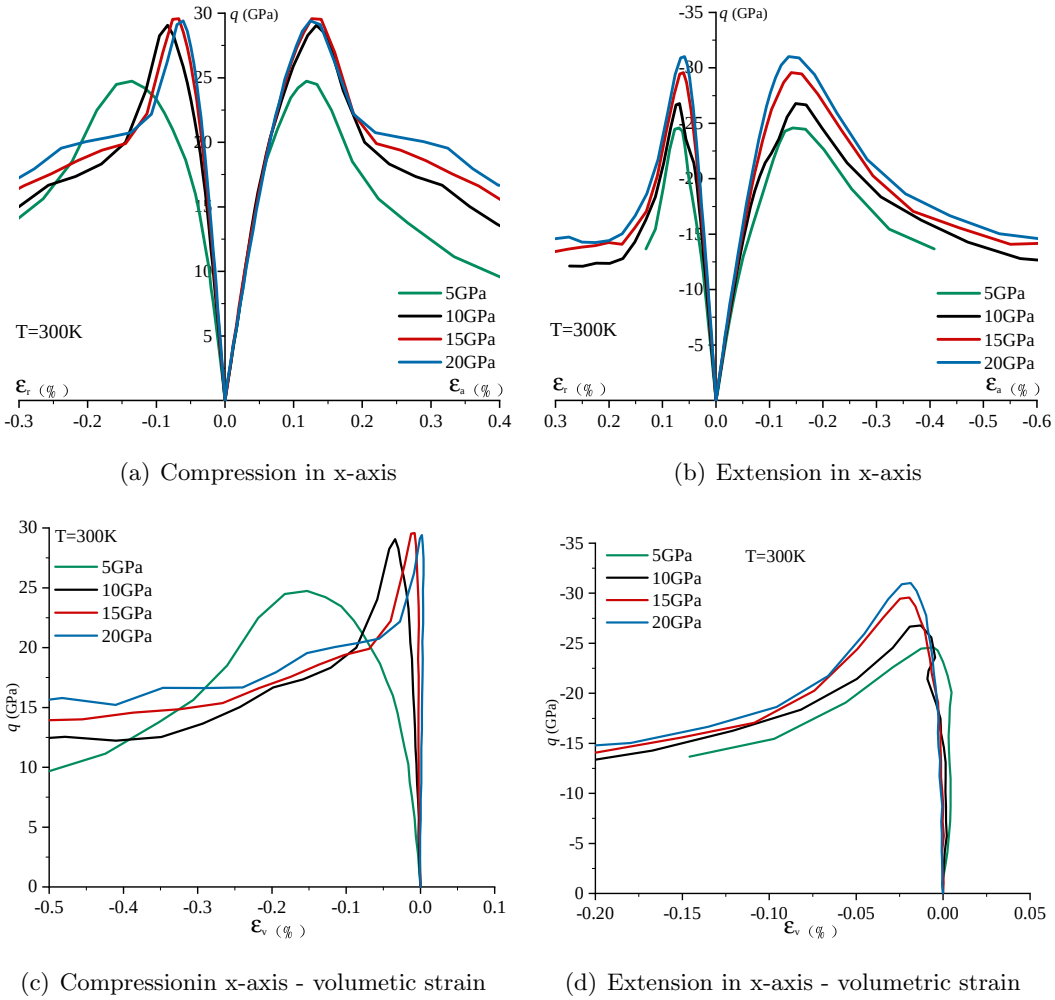

(a) Compression in x-axis

(b) Extension in x-axis

(c) Compressionin x-axis - volumetic strain

(d) Extension in x-axis - volumetric strain

Figure II .6: Comparisons of stress-strain curves in x-axis between different values of mean stress

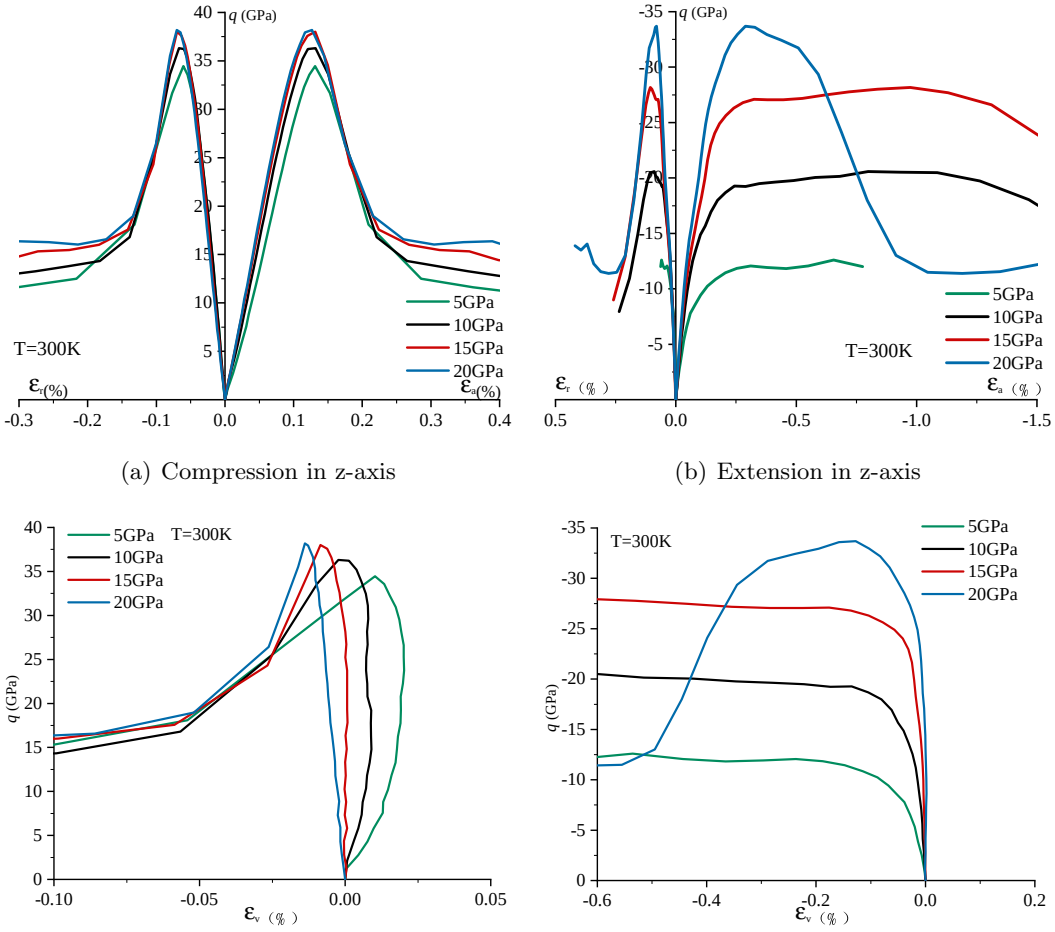

(a) Compression in z-axis

(b) Extension in z-axis

(c) Compression in z-axis - volumetrci strain

(d) Extension in z-axis - volumetric strain

Figure II .7: Comparisons of stress-strain curves in z-axis between different values of mean stress

3.5 Effect of crystal model size

Molecular dynamics studies provide a deep understanding of the properties of materials from the nanometer scale but also are limited by the system size. Previous studies have shown that some properties of materials are affected by the system size while some properties are size-independent in molecular dynamics simulations. For example, in (Yeh and Hummer, 2004), the authors have studied the system-size dependence of translation diffusion coefficients and viscosity of water and the Lennard-Jones fluid in molecular dynamics simulations under periodic boundary conditions and concluded the diffusion coefficients increased strongly as the system size was larger while the shear viscosity showed no significant system-size dependence. In (Sellan et al., 2010), the size effect of thermal

conductivity has been studied for Lennard-Jones argon and Stillinger-Weber silicon and found that there was no discernible size dependence for the simulation systems containing 4*4*4 to 8*8*8 conventional unit cells under periodic boundary conditions. There are also some studies on the mechanical properties of materials that have shown that the mechanical properties of the materials could depend on the size of the simulation system (Heino et al., 1998; Koh and Lee, 2006). The results of these previous works have shown that the mechanical parameters, such as Young's modulus, turned out to be independent of the system size or close to the theoretical bulk values for relatively large systems. However, to our best knowledge, there is still no detailed report about the size selection of clay mineral models in the molecular dynamics study of mechanical properties. In general, the super-cell of clay minerals used in MD simulations is from 4*2*2 to 16*8*8 in the previously reported studies (Carrier et al., 2014; Cygan et al., 2004; Ebrahimi et al., 2012,?; Manevitch and Rutledge, 2004; Mazo et al., 2008a,b; Suter et al., 2007; Yang et al., 2019).

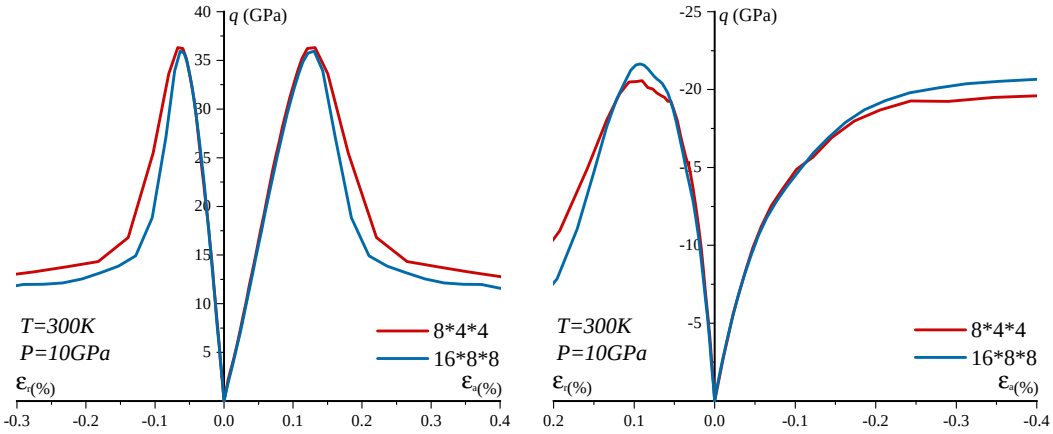

(a) Compression in z-axis (b) Extension in z-axis

Figure II .8: Stress-strain curves in z-axis for two systems of different size

In order to observe the structural changes during the system failure process more clearly, we prefer to choose a relatively small system in this study. However, it is our concern that small model may lead to errors in our quantitative results. In order to better determine the size of the system, we compare here two systems of different size of Na-MMT super-cells to capture the system size effect on the stress-strain behavior. The small system is the super-cell of 8*4*4 containing 5216 atoms and the big one is a super-cell of 16*8*8 containing 41728 atoms, which is considered as big enough to ignore the size effect. The overall stress-strain curves of two systems in the z-axis under a mean stress of 15 GPa during compression and extension are selected as example and shown in

Fig. II .8(a) and II .8(b). It is obvious to observe that the basic mechanical behavior is almost the same except a tiny difference of residual strength for the two different systems. Thus, the Na-MMT super-cell of 8*4*4 chosen in the previous simulations is considered as reasonable for the present study.

3.6 Effect of temperature

The influence of temperature on MMT mechanical behavior is now investigated. In Figures II .9 and II .10, the stress-strain curves obtained under four values of temperature and a mean stress of 20 MPa are compared for the two loading paths and in x-axis and z-axis. At first sight, the thermal effect on overall mechanical behavior is quite uniform. The increase of temperature does not affect the elastic properties, slightly enhances plastic deformation and in most cases reduces the peak differential stress. Some small quantitative differences are still observed between the loading paths and orientations. It seems that the temperature effect is more pronounced in extension than in compression. In particular, the thermal effect appears more complex for the case of extension in z-axis. The variation of peak strength with temperature is not regular while the residual strength decreases when temperature increases. Moreover, even with the large range of temperature considered here (from 300K to 1200K), it appears that the influence of temperature on the mechanical behavior of MMT crystal at the atomistic scale is less significant than on the macroscopic behavior of most clayey rocks. This is probably related to various scale effects and the presence of other minerals and pores in those rocks.

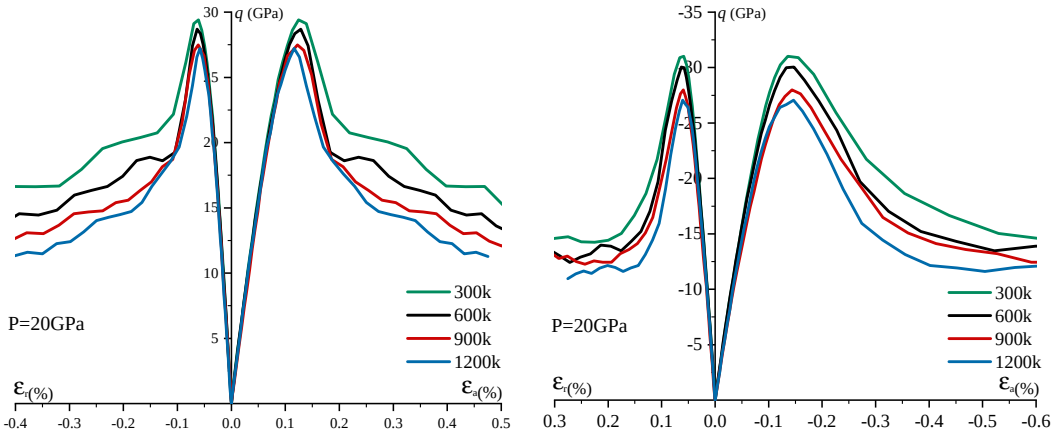

(a) Compression in x-axis

(b) Extension in x-axis

Figure II .9: Stress-strain curves in x-axis between different values of temperature

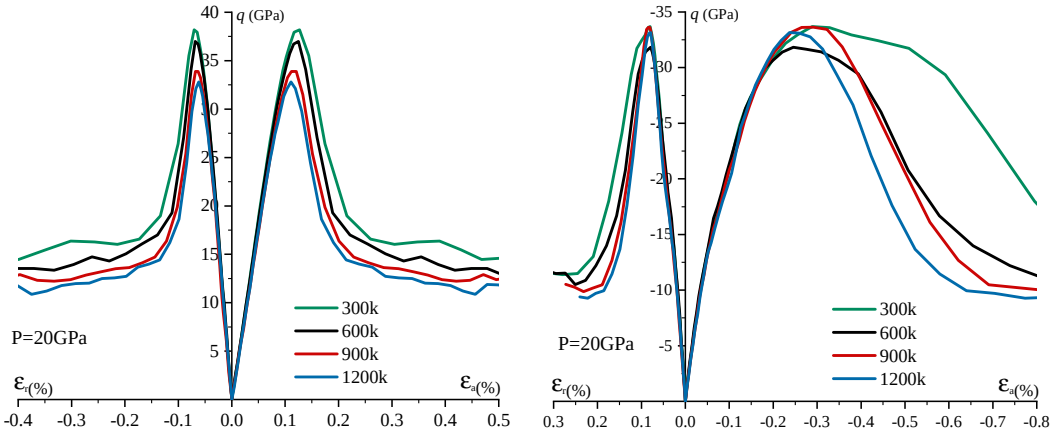

(a) Compression in z-axis

(b) Extension in z-axis

Figure II .10: Stress-strain curves in z-axis between different values of temperature

4 Further discussion on deformation and failure properties

4.1 Analysis of failure stresses at atomistic scale

The peak values of differential stress obtained from MD simulations on the MMT crystal are summarized and discussed here. In Figure II .11, the peak differential stress is plotted as mean stress for the compression and extension paths respectively in x-axis and z-axis. As a first approximation, the peak differential stress can be expressed as a linear function of mean stress. This corresponds to linear macroscopic failure criteria widely used at macroscopic scale for geological materials. It is observed that for both loading orientations, the slopes of failure stress lines in extension are higher than in compression. That means that the failure stress in extension is more sensitive to mean stress than in compression. As the slopes of failure stress lines are generally related to internal friction coefficient. It seems that the internal friction in extension is higher than that in compression. This result suggests that the failure surface (or criterion) of MMT crystal is a function of Lode's angle.

Concerning the thermal effect, as already observed above, the peak (or failure) differential stress is almost systematically smaller when temperature is higher. More precisely, for the loading in x-axis, the thermal effect is higher in extension than in compression. But for the loading in z-axis, the effect of temperature is much more important in compression than in extension for which the failure stress line is quasi independent on temperature. Furthermore, except for the case of extension in z-axis, it seems that the frictional coefficient (slope of failure stress lines) is very little affected by temperature. Therefore, the

thermal effect on failure strength is characterized by the reduction of cohesion (the value of failure stress for $\sigma_m = 0$) with increase of temperature.

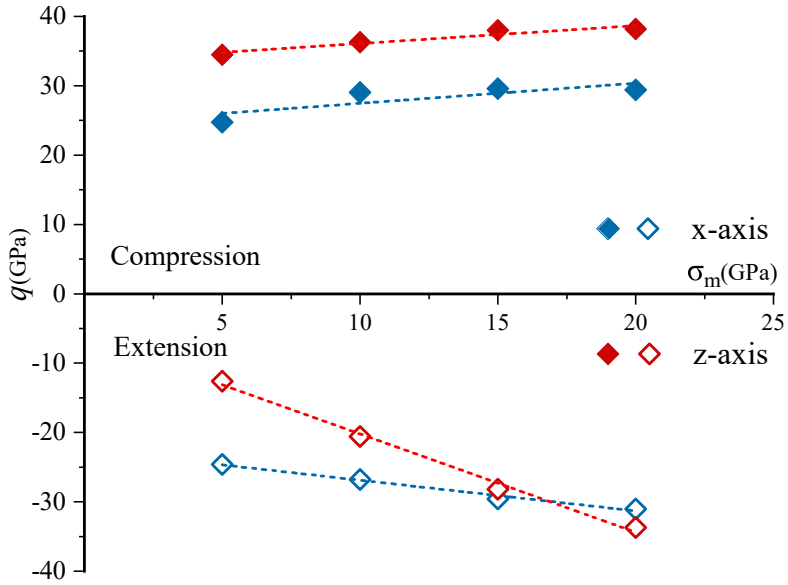

Figure II .11: Compression and extension of failure stress in the $\sigma_m - q$ plane in x (blue lines) and z (red lines) axes

4.2 Deformation and failure process at atomistic scale

The deformed crystal structures at different levels of loading are shown in Figures II .12 to II .15 for the compression and extension respectively along two axes. $q_{(p)}$ denotes the peak differential stress and the $q_{(f)}$ is the differential stress at the first point of residual strength phase.

More precisely, in Figure II .12, one shows the progressive deformation process during compression in z-axis. In this case, as the compressive axial stress is applied in the perpendicular direction to the crystal layers, the principal deformation process is the compaction of inter-layer space. The cohesion between layers is mainly contributed by the non-bonding interaction , namely the Coulombic and Van der Waals forces coming from the cation-layer and layer-layer interactions. The change of layer space will weaken the cohesion between layers, as characterized in terms of energy in (Duque-Redondo et al., 2014; Hantal et al., 2014). When the peak stress is reached, the MMT-crystal still keeps a layered structure in spite of large reduction of inter-layer space. When the residual state is finally obtained, there is a complete collapse of layered crystal structure. The deformation process during extension along z-axis is shown in Figure II .13. Due to the fact that a

tensile stress is applied in the perpendicular direction to crystal layers, the inter-layer spacing is gradually increased during both the elastic and plastic stages until 80% of peak strength. The atoms vibrate around the equilibrium position and structural damage is observed. When the differential stress approaches its peak value, there is bending of sheets and some atoms start moving towards the inter-layer space. The phenomenon of sheet bending, caused by the progressively increasing lateral stress, is the principal damage mechanism of crystal structure in the extension loading with a constant mean stress.

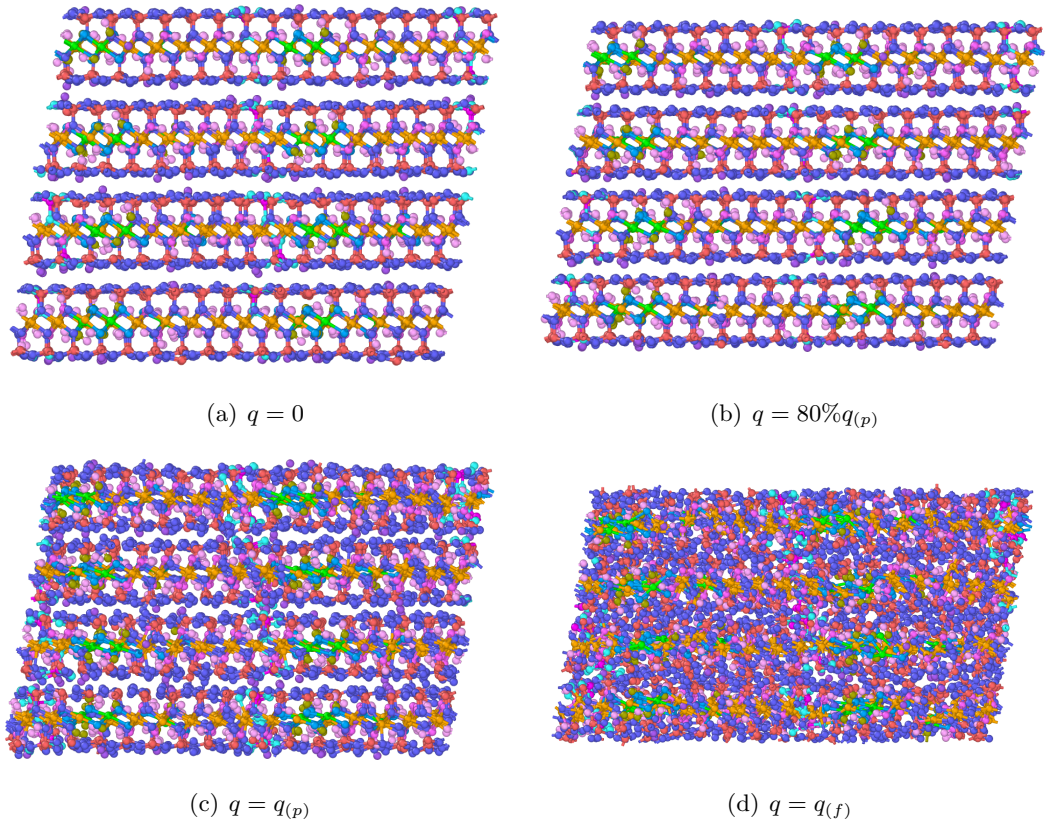

(a) $q = 0$ (b) $q = 80\% q_{(p)}$

(c) $q = q_{(p)}$ (d) $q = q_{(f)}$

Figure II .12: Deformed MMT crystal structures at different loading stages during compression in z-axis

When the compressive stress is applied in the parallel direction to crystal layers (x-axis), as shown in Figure II .14, one gets a progressive dilation of inter-layer space without structural damage until 80% of peak strength. The failure of crystal structure is essentially related to bending of sheets. For the case of extension along x-axis shown in Fig. II .15, the reduction of inter-layer space is the principal deformation process and the structural failure is caused by the collapse of inter-layer space. But the inter-layer space is not totally

closed even at the final residual stage.

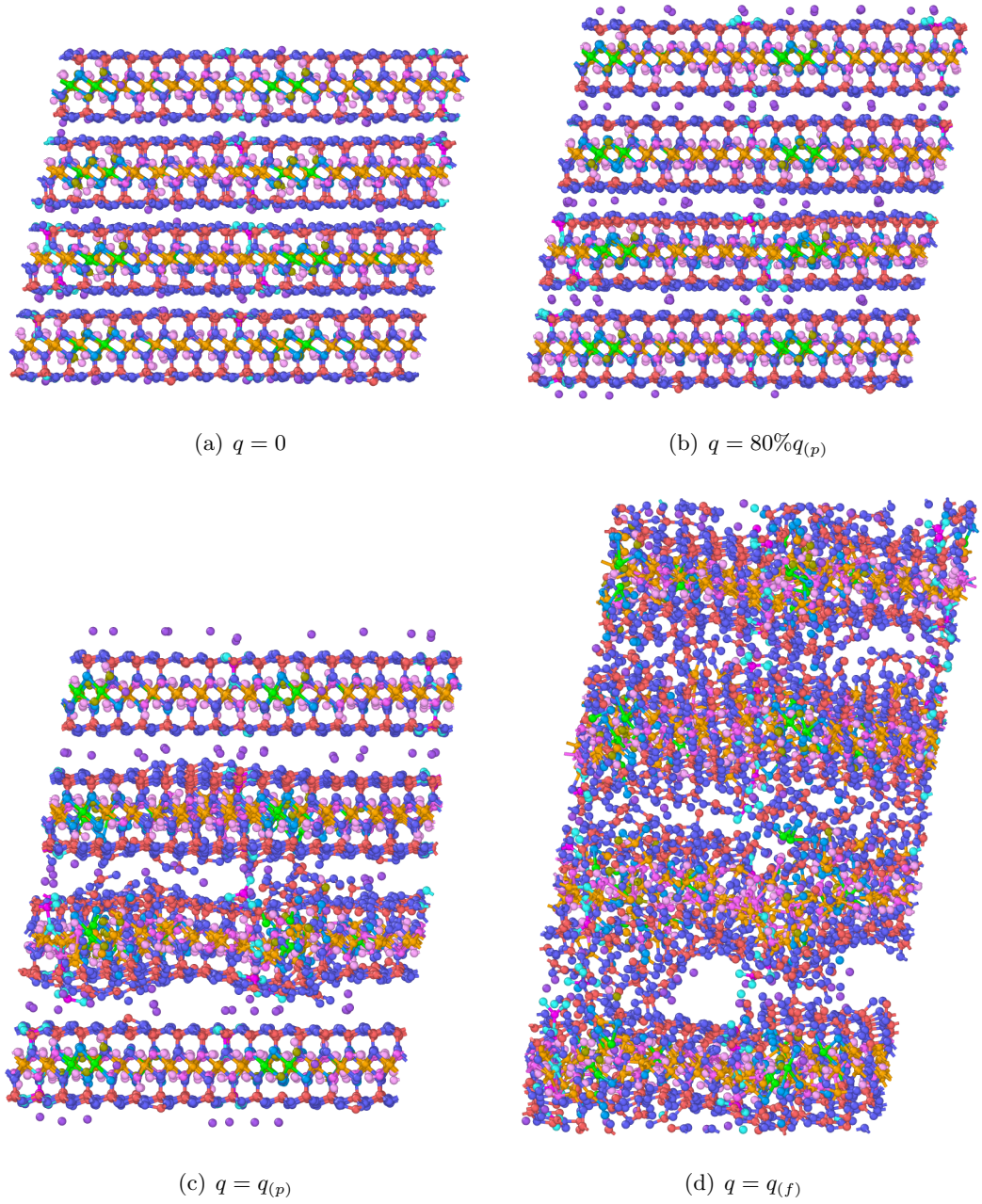

(a) $q = 0$

(b) $q = 80\%q_{(p)}$

(c) $q = q_{(p)}$

(d) $q = q_{(f)}$

Figure II .13: Deformed MMT crystal structures at different loading stages during extension in z-axis

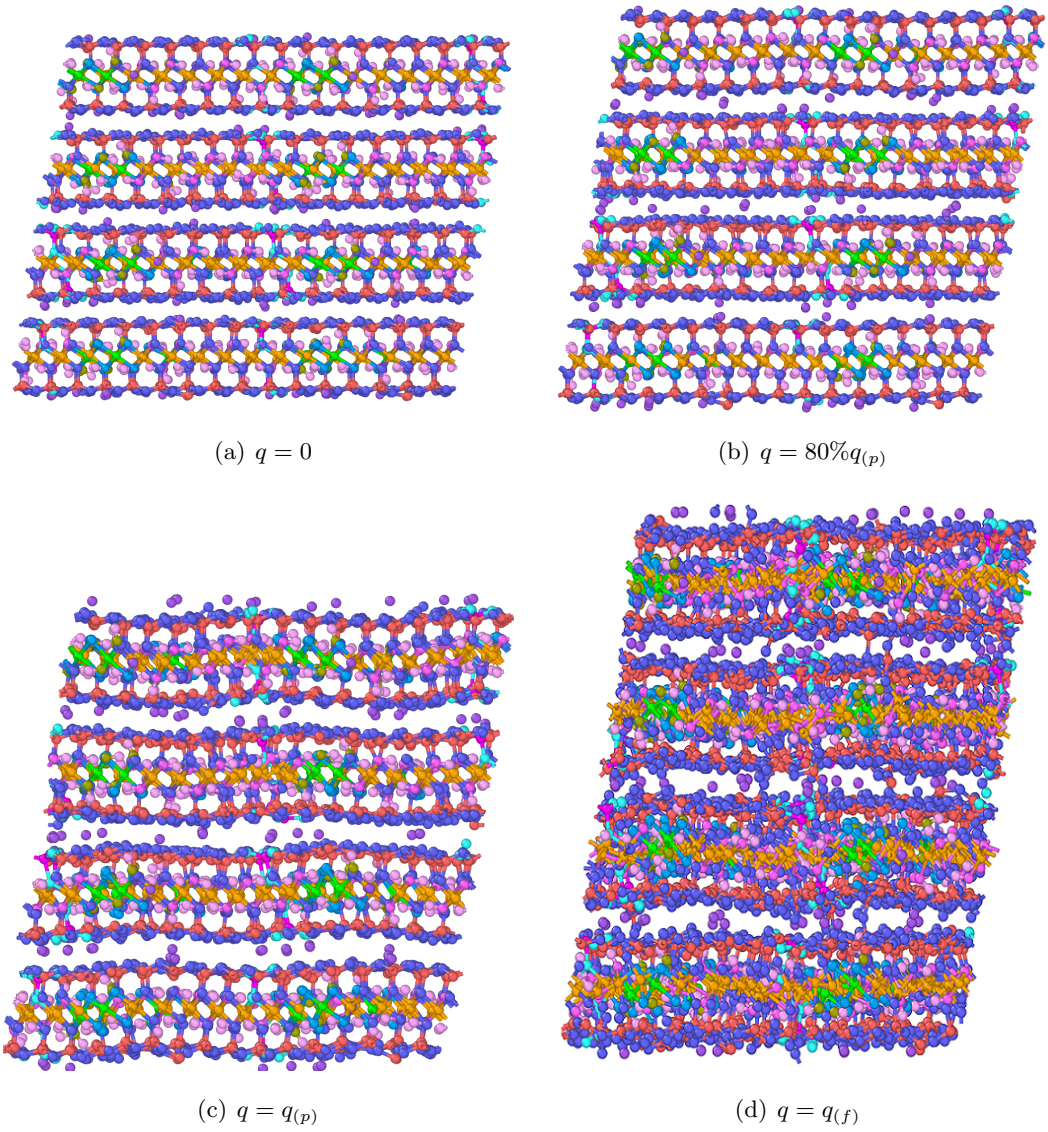

(a) $q = 0$ (b) $q = 80\%q_{(p)}$

(c) $q = q_{(p)}$ (d) $q = q_{(f)}$

Figure II .14: Deformed MMT crystal structures at different loading stages during compression in x-axis

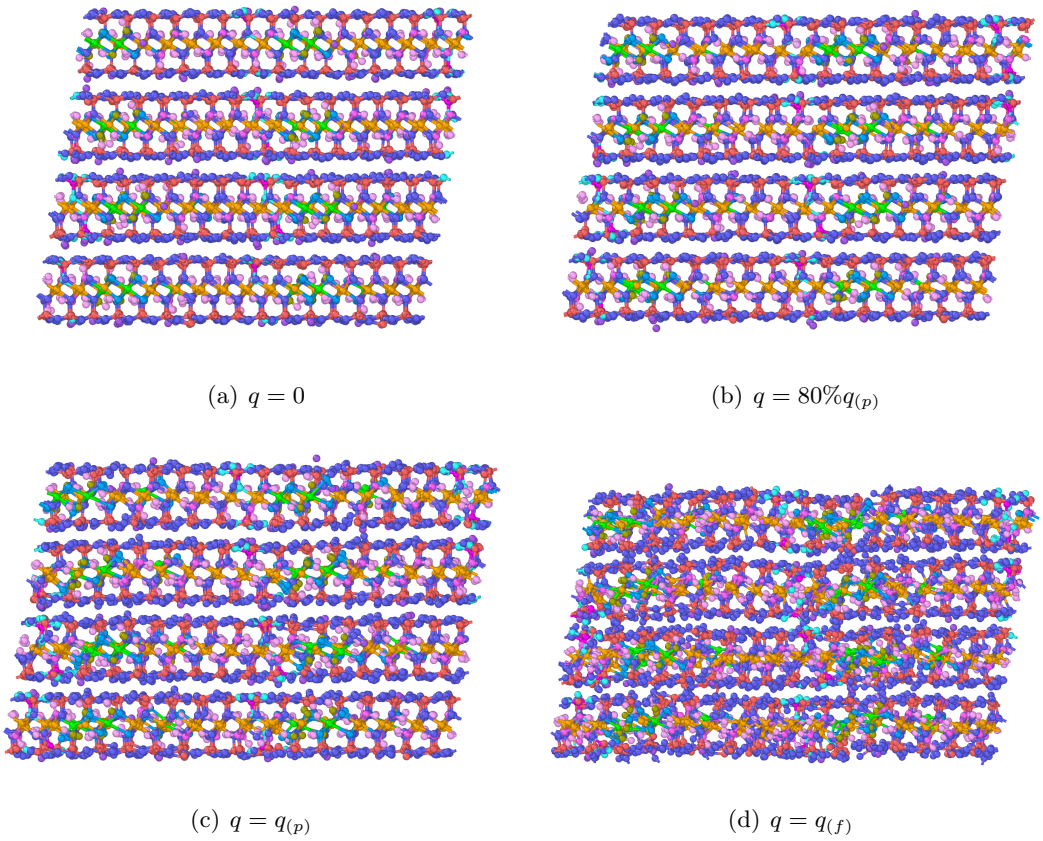

(a) $q = 0$ (b) $q = 80\%q_{(p)}$

(c) $q = q_{(p)}$ (d) $q = q_{(f)}$

Figure II .15: Deformed MMT crystal structures at different loading stages during extension in x-axis

From these results, it can be concluded that the failure mechanisms of the MMT crystal structure is not only influenced by loading paths (compression or extension) but also by the loading orientation with respect to crystal layers. In summary, the failure is caused by the collapse of inter-layer space for compression perpendicular to layers to for extension parallel to layers. However, the sheet bending becomes the principal failure mechanism for compression parallel to layer and extension perpendicular to layers. Finally, it is worth noticing that the positions where the isomorphous substitution happens (green atoms) have the tendency to form cracks.

5 Conclusions

A series of molecular dynamics simulations have been performed on the NaMMT crystal structure in order to investigate the mechanical behavior of clay particles at the atom-

istic scale. Two representative loading paths including compression and extension under constant mean stress were applied respectively in the parallel and perpendicular directions to crystal layers. Based on the results obtained, a number of concluding remarks can be formulated.

The basic stress-strain relationship at the atomistic scale is similar to that of most clayey rocks at the macroscopic scale. It is generally characterized by a short linear elastic phase followed by a large nonlinear plastic phase until the peak strength (represented by the absolute value of differential stress) is reached. A sharp or smooth material softening phase is observed in the post-peak regime due to damage of crystal bonds until the residual strength is reached.

The mechanical behavior of NoMMT crystal is strongly influenced by the loading path and orientation. In the perpendicular direction, the failure strength in compression is systematically higher than that in extension. But the difference is significantly reduced when the mean stress is high. In the parallel direction, the failure strength in compression is slightly higher than in extension under low mean stress but becomes slightly lower than extension under high mean stress. In general, the failure strength in compression in the perpendicular direction is higher than that the parallel direction. On the contrary, the strength in extension in the perpendicular direction can become lower than that the parallel direction under low mean stress. Therefore, the general failure criterion of NoMMT crystal depends on Lode's angle, mean stress as well as loading orientation. On the other hand, the post-peak stress-strain responses are also affected by these same factors, producing brittle or ductile behavior.

The mechanical behavior of Na-MMT crystal is further influenced by mean stress, but in a quite different manner in two loading orientations. In the parallel direction, the mean stress mainly affects the peak strength. But in the perpendicular direction, the mean stress affects not only the peak strength but also the post-peak stress-strain relationship by producing either a brittle or ductile behavior according to the value of mean stress. In a general way, the influence of mean stress is stronger in extension than in compression.

The deformation mechanism of crystal structure until around 80% of peak strength is mainly driven by the compaction or dilation of inter-layer space. Layer structure is progressively destroyed around the peak strength and during the softening zone. A relatively stable damaged structure is found and related to the residual strength of crystal. As a first approximation, the failure of crystal structure is generated by the collapse of inter-layer space under compression in perpendicular direction and under extension in parallel direction. The sheet bending is the principal failure mechanism under compression in parallel

direction and under extension in perpendicular direction.

A number of similar features have been observed between the atomistic behavior of clay crystal and macroscopic responses of clayey rocks, in terms of effects of loading path and orientation as well as mean stress on deformation and failure behaviors. Therefore, numerical results from molecular simulations can provide useful atomistic interpretation of macroscopic deformation and failure processes. However, macroscopic mechanical properties of clayey rocks are also strongly affected by other factors such voids and inclusions at different scales, and it is necessary to develop adequate multi-scale approaches. On the other hand, the mechanical behavior of both NoMMT crystal and clayey rocks are also affected by water content and temperature. These important issues will be investigated in our ongoing studies.

Chapter III

Effect of water content on mechanical property of claystone in compression

1 Introduction

Knowing the mechanical behaviors of clay-based materials in relation to water, especial failure property, is of crucial importance in earth sciences and in various industrial applications. For instance, hard claystone and swelling clay are used to put in water-rich deep underground as geological and engineered barriers for the storage of radioactive wastes which requires a deep knowledge of the failure characteristics of clay-rich rocks for long-term safety (Armand et al., 2013). Clay mineral, as the main component, play a dominant role on macroscopic deformation and failure process of clay-rich rocks because it is softer with respect to the mineral inclusions and has the ability to adsorb a great quantity of water and expand significantly upon hydration, modifying the interlayer connection, decreasing the cohesion, and leading to delamination or exfoliation in extreme cases (LeBaron et al., 1999). This is the fundamental reason why macroscopic mechanical properties of clay rich rocks strongly depend on water content (Liu et al., 2018a; Zhang et al., 2012). Therefore, building a macroscopic constitutive law that is able to predict the hydromechanical behavior of clay rich rocks in a bottom-up framework requires understanding and quantifying the hydro-mechanical behavior of the clay mineral.

At the atomic scale, swelling clay minerals, consist of (Meunier, 2005), the interlayer space is filled with a variable amount of adsorbed water molecules and with cations that ensure electro-neutrality of the system. The clay layers are stacked to form particles whose

thickness depends on the charge, size, type of cations and the charge of layer (Schramm and Kwak, 1982; Shomer and Mingelgrin, 1978). Therefore, the sensitivity to water of the mechanical properties of clay minerals originates from the scale of the clay layer. However, it is very challenging to directly measure the fundamental mechanical properties of clay layer due to their high affinity for water and their platy geometry (Vanorio et al., 2003). As computer models become increasingly more realistic, atomistic molecular dynamics(MD) computer simulation has during the past decades evolved into a tool suitable for addressing specific questions in materials science. In particular, it addresses the mechanism of water-related interactions in clay and clay-based hybrid materials (Chatterjee et al., 2021; Duque-Redondo et al., 2014; Wang et al., 2014).

MD simulations were first successfully applied to study the hydration and swelling of clay-based materials which is the basic and critical property related to water, with the introduction of water into the interlayer region, the compensating cations are hydrated, causing expansion of interlayer spacing and alteration of interlayer structure (Boek et al., 1995b; Rahromostaqim and Sahimi, 2018; Shroll and Smith, 1999; Underwood and Bourg, 2020; Yeh and Hummer, 2004; Zhang et al., 2014b). Generally, the strong electrostatic interactions between the clay layers and cations at dry state are gradually shield by the water molecules with the introduction of water molecules due to the hydration of cations, resulting in the great changes of interlayer connection which has proved to be closely related to mechanical properties (Wei et al., 2021). Therefore, the intrinsic micro-structure, as the basic knowledge to understand the mechanical property related to water of clay minerals at atomic level, has been studied for more than half a century. Based on previous researches (Duque-Redondo et al., 2014), the cohesion between clay layers for clay minerals with water can be described by attending to two types of connection: the first is related to interlayer cations consisting of the linkage to clay surface and water molecules. The second is about hydrogen bond network, including the hydrogen-bond network among water molecules and the clay surface. The effects on the hydration of cations simply are accounted for by increasing the radius of the ions. The enlarged ionic radius thus corresponds to the hydrated ionic radius? representing the size of the ion plus the hydration shell of tightly coordinated and oriented water molecules around it. With decreasing interlayer distances, the hydration shell may deform, eventually resulting in water molecules being squeezed out from the inner hydration shell. However, there are still some researches have shown not all cations are hydrated, they prefer to stay on clay surfaces to balance the negative surface charges and build up the relatively strong electrostatic interaction to resist external loading even at high water content which depend on the category of

cation, charge, the site of isomorphous substitution and so on (Subramanian et al., 2020; Teich-McGoldrick et al., 2012; Yang et al., 2017; Zhang et al., 2014b). In addition, hydrogen bond network, as a major contributor to mechanical strength at moist state in general, has been studied extensively and concluded that the adsorbed water molecules exist in two forms between the layers: (1)physical bound water was deeply adsorbed near the clay surface by the hydrogen bonds between water molecular and the oxygen on the clay surface. (2)capillary water was not bound and diffused freely like bulk water in the interlayer region which also connect each other through hydrogen bonds among water molecules (Erbas et al., 2012; Leng and Cummings, 2005, 2006; Raviv and Klein, 2002; Strauss et al., 2014). The way in which the properties of such adsorbed water layers differ from those of bulk water has for decades excited much debate. The top views have shown the density of confined water remains approximately the bulk value or less, whereas the diffusion of water molecules decreases dramatically. Further, it's structural and functional properties (density, mobility and ordering) of confined water vary between solid surfaces due to load and shear condition based on the wetting behavior of surfaces confining them, for example, the increase in confinement leads to a transition to a bi-layer ice, whose density is much less than that of ice because of the formation of a specific hydrogen-bonding network while they retain extremely a shear fluidity characteristic of the bulk liquid (Erbas et al., 2012; Leng and Cummings, 2005, 2006; Raviv and Klein, 2002; Strauss et al., 2014). The difference is proved to be crucial and is directly implicated clay plasticity (Ravina and Low, 1972). On this basis, the study of molecular dynamics on mechanical properties related to water of clay minerals is gradually expanded and deepened. At first, the elastic property of clay particles under different extent of hydration calculated by MD has been reported that the Young's modulus decrease with the increase of water content (Mazo et al., 2008a,a; Suter et al., 2007). Besides, the knowledge of failure mechanism at nano scale provides the deep understanding for macroscopic mechanical properties. In the work reported in Ref (Duque-Redondo et al., 2014), the authors have proved that the mechanical performance of clay hybrid material under uniaxial tension perpendicular to layers and shear along layers was dependent only on the cohesion between layers, while the layers themselves do not participate in the failure mechanism. The Coulombic force was more significant when a tensile strain was applied, while the hydrogen bonding became relevant under shear loading. Further, the results of MD calculation of calcium silicate hydrate gel have proven that water molecules have little influence on the compressive strength while the tensile strength greatly decreases from dry to the saturated state because the hydrogen bond network is difficult to be broken during uniaxial compression (Hou et al., 2014).

Although a large number of previous studies have provided great insight into the strength of interlayer connection under simple loading path such as shear, uniaxial tension and uniaxial compression, which causes the damage of interlayer structure while little deformation of the clay layer (Duque-Redondo et al., 2014; Medhekar et al., 2010). However, to the author?s knowledge, the coupling between deformation of the clay backbone and the rupture mechanisms of interlayer structure under complex loading paths has not yet been clarified. From a practical point of view, for example in the case of underground cavity excavation, two loading paths are particularly relevant (Liu et al., 2019a; Zhu et al., 2021). One of them is called triaxial compression, starting from initial $in-situ$ stress state, one principal stress is increased in compression while two others are decreased so that the mean stress remains constant. In our study, this triaxial compression with constant mean stress, namely σ_m=0.5 GPa, is selected to the montmorillonite systems with different hydration extent to study their strength and analyze the failure processes at molecular scale. The molecular forces that trigger the mechanical failure and govern the cohesion between clay layers and the deformation of clay layer has been investigated. The knowledge of their fundamental properties will give us valuable information to understand the influence of water content on the mechanical properties.

2 Models and methods

2.1 Crystal structure

The monoclinic atomic structure of Wyoming sodium montmorillonite(MMT) considered in our research is based on the natural (Boek et al., 1995a,b; Chang et al., 1995). It has the layered structure composed of one alumina octahedra(O) sheet sandwiched between two silica tetrahedra(T) to form a typical TOT layer structure. The chemical formula of the unit cell is expressed as $Na_{0.75}[Si_{7.75}Al_{0.25}][Al_{3.5}Mg_{0.5}]O_{20}(OH)_4.nH_2$ with negative charge $0.75e$ because of isomorphous substitution according to Loewenstein's rule (Bell et al., 1992; Loewenstein, 1954) to ensure that the nearest sites were not substituted at same time. The negative charge of the layer was compensated with sodium cations.

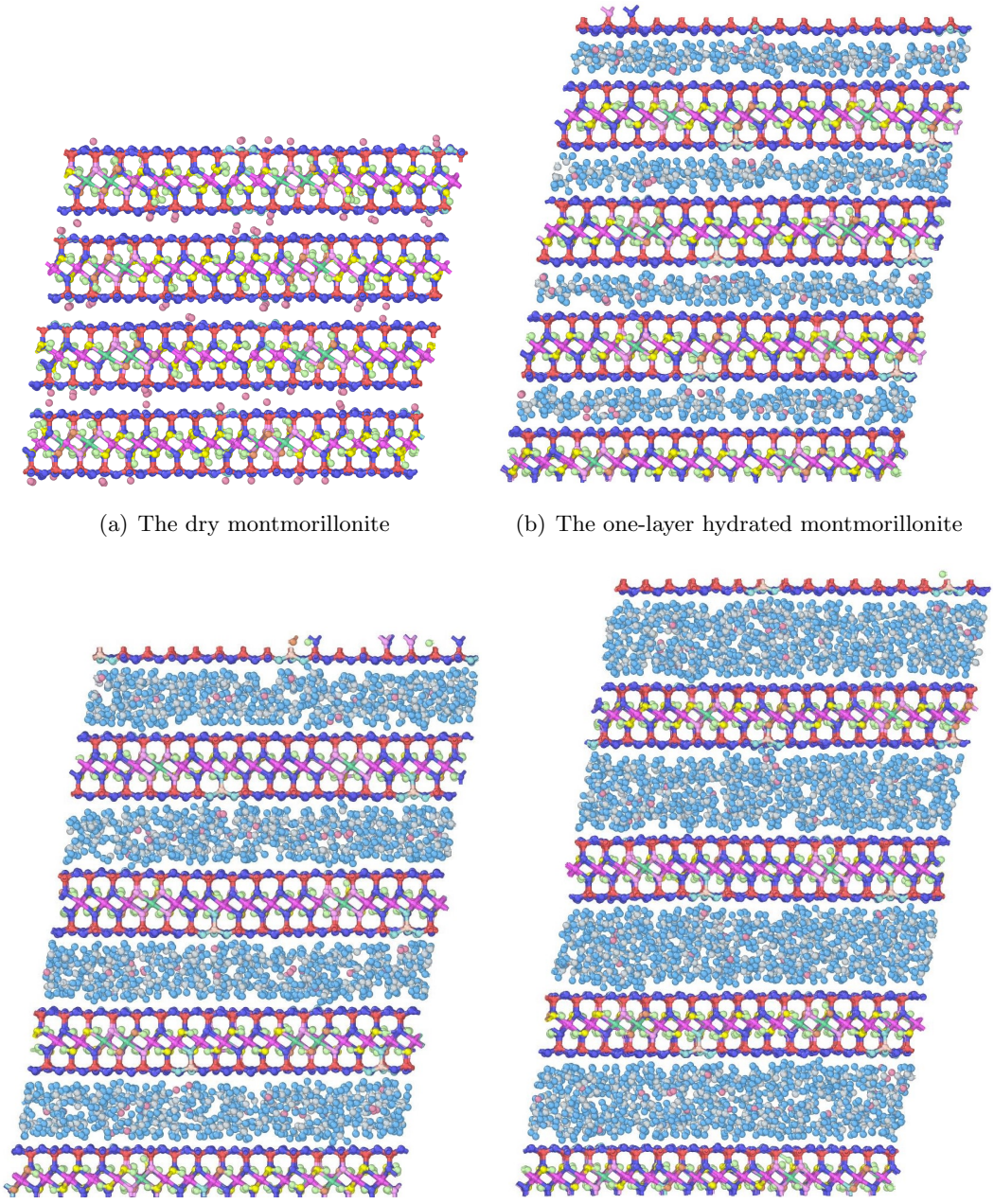

(a) The dry montmorillonite

(b) The one-layer hydrated montmorillonite

(c) The two-layer hydrated montmorillonite

(d) The three-layer hydrated montmorillonite

Figure III .1: The atomic structure of montmorillonite

Besides, different amounts of water molecules are introduced into the interlayer to form clay-water systems with different water content. Water molecules in our study is represented by SPC/E water model of Berendsen and co-workers (Berendsen et al., 1987), which have a rigid geometry with a bond length of 1 r A and a tetrahedral bond angle of 109.47°. According to the previous research, we constructed dry, one-layer, two-layer

and three-layer hydrated state systems shown in Fig. III .1(a), Fig. III .1(b), Fig. III .1(c), Fig. III .1(d) respectively, the number of interlayer water molecules for each unit cell increases from 0 to 12 (corresponding to water content ranges from approximately 0 to 0.3). We use N(H_2O) to indicate the number of water molecules in unit cell. Adsorbates H_2O locating in inter-layers are randomly distributed basing on Monte Carlo method. In our study, a periodic super-cell of size 8*4*4 in the a, b, c dimensions was generated by expanding the unit cell, which is large enough to ignore the size effect (Zhu et al., 2021).

2.2 Force filed

The CLAYFF force field developed by (Cygan et al., 2004) is adopted to compute the forces between atoms in present research. The total potential energy (E_{total}) in Clayff is shown in eq.1 and eq.2, it is composed of the Coulombic interactions (E_{Coul}), the van der Waals interactions (E_{VDW}) and the bonded interactions. The bonded terms include the bond stretch energy ($E_{bond\ strech}$) and the angle bend energy ($E_{angle\ bend}$) that is widely used in water and metal with hydroxyl. In the last few decades, CLAYFF force field has successfully simulated the crystal structure of different clay (Cygan et al., 2004; Leng and Cummings, 2006; Porion et al., 2007; Suter et al., 2007; Wang et al., 2005), mobility of interlayer water (Kalinichev et al., 2007; Leng and Cummings, 2006; Porion et al., 2007; Suter et al., 2007; Wang et al., 2005) because of the huge advantage of allowing atoms complete translation freedom. Recently, it has also widely used to study the mechanical behavior of clay and contributed to the understanding of the basic mechanical mechanism from atomic level (Carrier et al., 2014; Cygan et al., 2004; Ebrahimi et al., 2012; Manevitch and Rutledge, 2004; Mazo et al., 2008a,b; Suter et al., 2007; Zhang et al., 2015). Besides, the effectiveness of CLAYFF force field in the study of mechanical properties of clay minerals was evaluated through the comparison of simulation and experimental results by some researchers (Teich-McGoldrick et al., 2012). The total potential energy (E_{total}) is composed of the Coulombic interactions (E_{Coul}), the van der Waals interactions (E_{VDW}) and the bonded interactions. The bonded terms include the bond stretch energy ($E_{bond\ strech}$) and the angle bend energy ($E_{angle\ bend}$) that is used in water and metal with hydroxyl. One gets:

$$\begin{cases} E_{total} = E_{Coul} + E_{VDW} + E_{bond-strech} + E_{angle-bend} \\ E_{Coul} = e^2/4\pi\epsilon_0 \sum_{i\neq j} q_i q_j / r_{ij} \\ E_{VDW} = \sum_{i\neq j} D_{0,ij}[(R_{0,ij}/r_{ij})^{12} - 2(R_{0,ij}/r_{ij})^6] \\ E_{bond-strech} = k_1(r_{ij} - r_0)^2 \\ E_{angle-bend} = k_2(\theta_{ijk} - \theta_0)^2 \end{cases} \quad \text{(III .1)}$$

r_{ij} is the distance between the atoms i and j. In the Coulombic energy, e is the charge of an electron, ϵ_0 is the dielectric permittivity of a vacuum ($8.85419 \times 10^{12} F/m$) and q_i and q_j are the atomic partial charges, which can be derived from quantum mechanics calculations. In the Van der Waals energy, the terms $D_{0,ij}$ and $R_{0,ij}$ are calculated by:

$$\begin{cases} R_{0,ij} = 1/2(R_{0,i} + R_{0,j}) \\ D_{0,ij} = (D_{0,i} * D_{0,j})1/2 \end{cases} \quad \text{(III .2)}$$

About the $(O-H)$ bond stretch energy, k_1 defines a force constant and r_0 represents the equilibrium bond length. Finally for the angle bend energy, k_2 is a force constant, θ_{ijk} denotes the bond angle for the mental-oxygen-hydrogen and θ_0 is the equilibrium bond angle.

2.3 MD simulation procedure

A parallel molecular dynamics code Lammps (Plimpton, 1993) is used to perform simulations on the crystal structure of Na-Montmorillonite defined above. The samples are first relaxed at the desired temperature using an NVT (conserving the number of atoms, volume, and temperature) ensemble for 200 ps followed by an independent relaxation in three directions using an NPT (conserving the number of atoms, pressure, and temperature to mimic bulk behavior) ensemble for another 200 ps with zero pressure in all the directions. These relaxation steps are performed to uniformly distribute the excess free energy through the whole system.

Mechanical loads are then applied to the samples and their deformations are calculated. The loading path of triaxial compression with constant mean stress is considered. A hydrostatic compressive mean stress is first applied in three principal directions of the crystal sample. Then, after the stabilization of strains under the mean stress, in the

compression loading, one of three principal stresses is further increased (called the axial stress and denoted as $\sigma_a > 0$) while the others are decreased (called the radial stress and denoted as $\sigma_r < 0$) so that the value of mean stress remains unchanged $(\Delta\sigma_a + 2\Delta\sigma_r) = 0$. In this study, the value of mean stress is selected as 0.5 GPa, namely σ_m=0.5 GPa. The increase of the axial stress is proceeded at the rate 10MPa/fs while that of the radial stress at the rate 5MPa/fs according to the Parrinello-Rahman method under the constant temperature($T = 300K$) which is controlled by the Nose-Hoover thermostat. All simulations are run until failure of sample. The time step is set to 0.01 fs. A periodic boundary condition is adopted in all directions.

3 Results and discussion

3.1 Swelling property

Table III .1: The basal distance as a function of the number of water molecular for the unit cell

N(H2O)			Reference
4	8	12	
12.3-12.6	14.9-15.6	17.9-18.5	Experiment
12.32	14.96	17.07	1995 E.S. Boek
12.17	14.91		2015 Stephanie L
12.08	15.28	18.77	1995 Fang-Ru
12.22	14.91	17.93	1996 S. Karaborn
12.21	14.9	17.23	Our result

Swelling is the basic and important property for the MMT. It is well-known that the adsorption of water molecules induces an expansion of the clay interlayer space by reducing the electrostatic interactions of the negatively charged layers while simultaneously solvating the free sodium ions and clay surface. Our calculation of the relationship between the number of water molecules containing in each unit cell and the d-spacing at 300k is shown in the Table, the basal distance is the length between the middle planes of two adjacent

sheets, the number of 4, 8, 12 water molecules in each unit cell hints at the existence of one, two and three-layer hydration, represented the water content at approximately 0.1g, 0.2g and 0.3g of H2O/g of clay. the overall step-wise swelling behavior of montmorillonite is indeed agree well with previous simulations (Boek et al., 1995a; Chang et al., 1995; Karaborni et al., 1996; Teich-McGoldrick et al., 2015) and experimental studies (Ferrage et al., 2010; Morodome and Kawamura, 2009) which validates the conformation obtained from our simulation.

3.2 Stress-strain response of compression in z-axis

According to the typical stress-strain curves shown in Fig. III .2(a), the basic mechanical behavior of MMT under compression condition is strongly nonlinear. There is a short linear phase at the beginning of loading, indicating the elastic behavior of MMT. The linear phase is followed by a nonlinear one with increasing axial and radial strain until the peak deviatoric stress is reached. This nonlinear phase corresponds to the plastic deformation of the crystal sample. The peak deviatoric stress represents the maximum mechanical strength. However, the Na-MMT models exhibit different mechanical behaviors due to different number of water molecules in each unit cell corresponding to different water content. During the elastic phase, the axial elastic deformation increases with the increase of the water content under the same deviatoric stress level, and it has slight differences in the cases of comparatively high water content (i.e., two-layer and three-layer hydrated states). However, the results also indicated that the water content has slight effects on the lateral elastic deformation . For the plastic phase, the peak axial strain increases with the increase of water content but the strength decreases accordingly except the two-layer hydrated model which has the higher mechanical strength than one-layer hydrated model and the maximum deformation at peak strength among the four states. These results are not in good agreement with the previous findings reported from macroscopic experiment, the similar irregularities also occur in the post-peak phase. The decrease of deviatoric stress for one-layer and three-layer hydrated models show the similar trend with a slower stress drop, showing notable ductile behaviors compared to the other models. The special mechanical behavior of the two-layer hydrated state is mainly contributed to its interlayer structure and the ion-bond and h-bond-induced deformation of clay layer. More detailed discussions are given in the following section. Near the peak strength, the stress are primarily contributed by the clay layer, and the damage of the di-octahedral structure results in the weakening of their mechanical strength. As a consequence, the material weakening behavior during the post-peak phase can be obtained. Furthermore, the plastic deforma-

tion is inherently coupled with the weakening of chemical bonds, which concluded that the mechanical strength decreases with the increase of water content in compression test.

The variations of volumetric strain are illustrated in Fig. III .2(b). The volumetric strain is clearly compressive before the peak strength is reached and then turns into dilating in the post-peak region. This is clearly a consequence of compaction of inter-layer space along the z-axis. The volumetric dilatancy means an irreversible variation in the crystal structure, which can be regarded as an omen to the failure of crystal sample. In general, the volume variation is significantly affected by the water content that the peak volumetric strain increases with the increase of water content. However, the most obvious volume compaction and fastest evolution of volume appears in the case of the two-layer hydrated system. It's worth noting that for other cases, the inflection point of volume appears near the peak strength while it's relatively far for the two-layer hydrated state which mainly due to the orderly arrangement of water molecules between layers. This will be further discussed in the following sections.

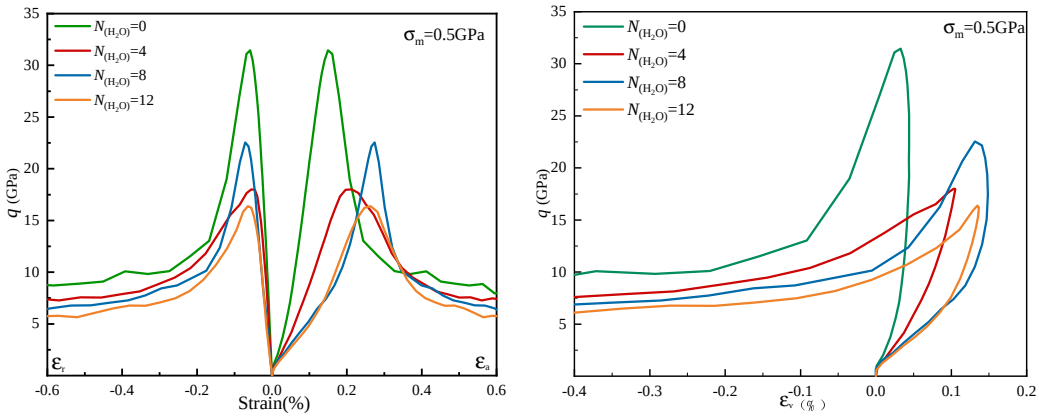

(a) Compression in z-axis - stress strain (b) Compression in z-axis - volumetrci strain

Figure III .2: Mechanical property of Montmorillonite under compression

3.3 Structural deformation characteristics

The mechanical properties of clay minerals are largely dependent on the arrangement of interlayer molecules and the linkage between interlayer molecules and clay layers. Thus, before analyzing the forces acting between the clay layers, we studied the molecular arrangement of one dry and three different water content MMT systems at the initial and the peak stress state. The intensity profiles of different atoms along the z direction in the four states are plotted in Fig. III .3. It can be observed clearly, the alternative maxima of St, Ao constitutes the basic and ordered skeleton of montmorillonite, in the interlayer re-

gion among MMT skeleton, water molecules (H and O) and Na cations (Na) are randomly distributed. The peaks corresponding to the oxygen atoms of the water molecules indicate that these are organized in one, two, and approximately three layers which become a little disorder. With respect to H atoms, they have more broaden density peaks than that of O atoms. The ability of water molecules to induce swelling in a step-wise fashion is related to the formation of an extended hydrogen bonding network and interaction of the water molecules with clay surface. The preferential residence of counterions is quite different. For the dry state, as shown in Fig. III .3(a), a small number of Na^+ across the interlayer region and impregnates into the aluminum oxygen octahedron forming strong ion-bond to hold stable structure of MMT. The rest distributed in the interlayer region with the approximate symmetric bimodal form, this is mainly due to the attraction of the tetrahedron bridging oxygen. In the one-layer case (Fig. III .3(c)), Na^+ almost evenly distributed across the entire interlayer region which means that Na^+ ions tend to get close to the montmorillonite surfaces and are only partly hydrated. However, most of the sodium are almost concentrated in the interlayer mid-plane for both of the two-layer and three-layer cases (Fig. III .3(e), Fig. III .3(g)), it is arranged into a mono-layer sandwiched by the two separated water layers for two-layer hydrate state while shows two peaks separating away from the clay surfaces by the water layers in the three-layer case, this arrangement indicated that Na^+ ions are almost fully hydrated at high water content. Meanwhile, there are two approximately symmetric small peaks located between the main peak and the clay layer, which can be attributed to the stronger electrostatic interaction between Na^+ and the charged clay sheets. Existing reports for simulated sodium hydrates of MMT has been confirmed that Na^+ ions tend to get close to the montmorillonite surfaces at low water content while prefer tightly bound hydration shells and therefore, are likely to be in the middle surrounded by interlayer water at high water content, only a few Na^+ drop into the clay surface because of the strong attraction of tetrahedron substitution oxygen (Subramanian et al., 2020; Tambach et al., 2006; Zhang et al., 2014b). This conclusion is completely in agreement with ours. The above analysis shows that in the dry and low water content system, the clay layers are primarily connected by the ion-bonds between counterions and oxygen atoms on the surface of clay. However, with the increase of water content, the clay has expanded to where the electrostatic interactions of the clay layers are effectively shielded from the sodium ions by the interlayer water, and there is noneffective coordinated stabilization of the configuration.

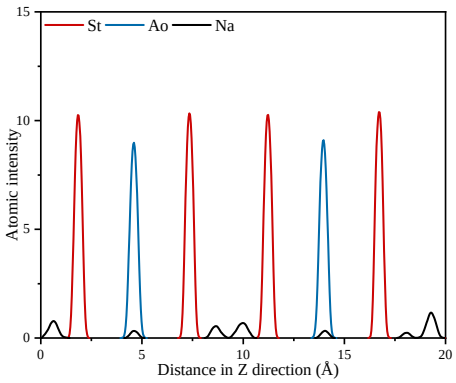

(a) $N(H_2O)$=0 at initial state

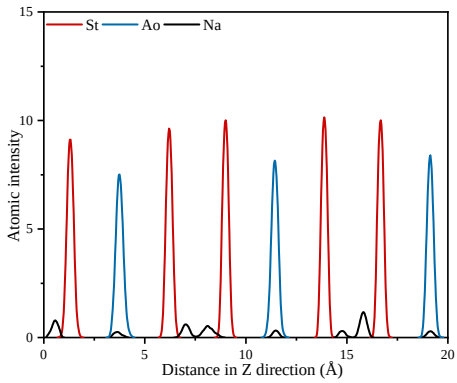

(b) $N(H_2O)$=0 at peak strength

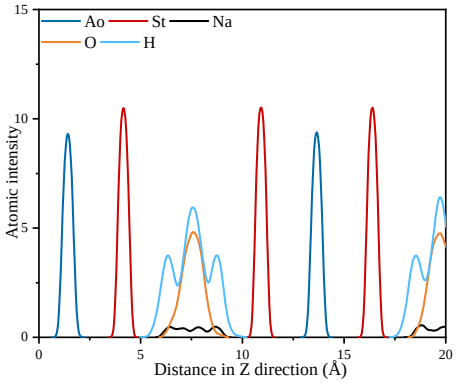

(c) $N(H_2O)$=4 at initial state

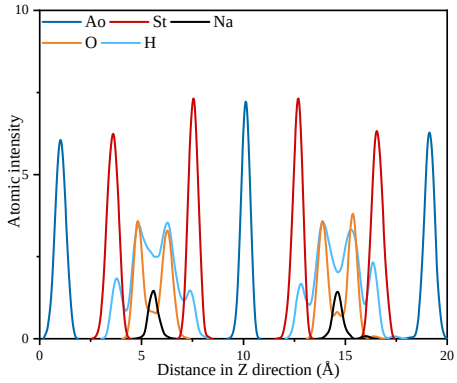

(d) $N(H_2O)$=4 at peak strength

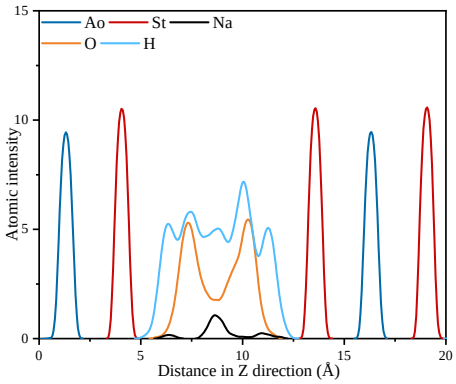

(e) $N(H_2O)$=8 at initial state

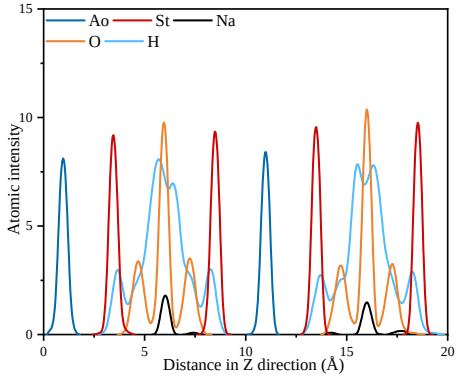

(f) $N(H_2O)$=8 at peak strength

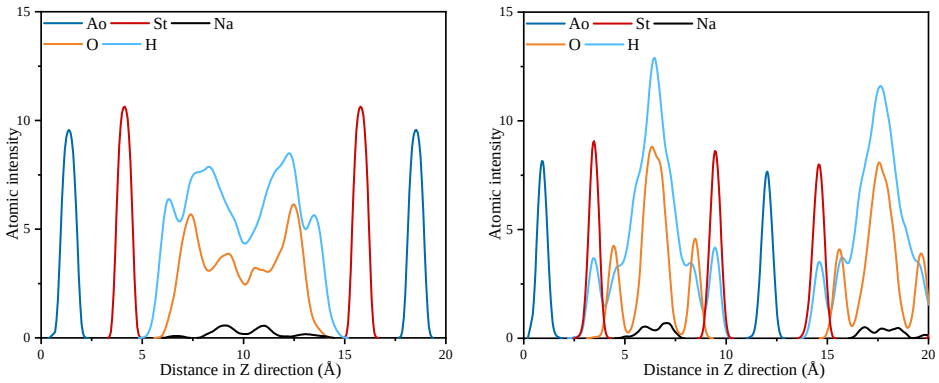

(g) $N(H_2O)$=12 at initial state (h) $N(H_2O)$=12 at peak strength

Figure III .3: Atomic intensity profiles along the Z direction

The comparison of density profile at the initial stage after equilibrium and the broken stage at the peak stress reflects the movement of atoms and deformation characteristics during compression. Respectively, the Fig. III .3(b) III .3(d) III .3(f) III .3(h) show the density profile at peak stress for dry and different hydration state. A series of main deformation features for different systems can be obtained. At first, the interlayer space has undergone marked compression while the vertical deformation of the clay layer is relatively small. For the dry state, the relative position of cations between layers has hardly changed, which means the failure of the model is mainly caused by the deformation of the clay layer. However, the Na cations for hydration systems have shown the tendency away from the clay surface, forming a single peak structure for one- and two-layer hydrated systems and two peaks for three-layer hydrated system at peak stress. Besides, the rearrangement of water molecules is very similar and become more regular for the different hydration systems, most of them moved to the center and the rest is adsorbed on the clay surface with much less density forming a three-peak interlayer structure dominated by the middle peak in the interlayer, which shows the great agree well with the previous reports that the increase of confinement leads to a transition to a bi-layer ice whose density is much less than that of bulk water (Leng and Cummings, 2006). The above analysis illustrates that the deformation characteristics of interlayer structure during compression are the critical embodiment of failure mechanism.

3.4 Radial distribution function of cations

The complex inter-facial structure can be investigated using radial distribution functions (RDF) and coordination number of equilibrium structure, denoted g(r) and CN

respectively, calculated between interlayer cation and the oxygen atoms coming from water or clay surface. In our case of dry sample (Fig. III .4(a)), Na^+ is the only counterions locating between layers which can interact with oxygen atoms on the clay surface through Coulomb and Van der Waals interaction to connect clay platelet directly. According to the former analysis of the density profile, the Na cation distributed in octahedral cavities which were mainly attracted by the bridging oxygen with octahedral substitution due to it's high electro-negative named $O_{(obos)}$ and interlayer which will interact with $O_{(ob)}$/ and $O_{(obts)}O_{(ob)}$. The $O_{(ob)}$ represent the bridging oxygen of alumino-silicate sheet and the $O_{(obts)}$ is the bridging oxygen with the tetrahedral substitution. To better understand the structure features of Na-O, we further differentiated the RDF (Na-O) into three pairs, as shown in Fig. III .4(a). The peak of RDF describes the short-range spatial correlation of Na^+ with its coordinated oxygen atoms of clay surface, the Na-$O_{(obos)}$, Na-$O_{(obos)}$, Na-$O_{(ob)}$ shows a maximum at 2.25, 2.35 and 2.58Å respectively, which matches with the average distances found in previous researches (Subramanian et al., 2020; Tambach et al., 2006; Zhang et al., 2014b). The first coordination number of Na^+ can be obtained from the integral of the RDF profile from the position starting r = 0, where RDF is approximately zero to the position where the first minimum locates after the first peak. It can be obtained the sodium coordination number (CN) in the first shell is about 8 for our dry system, mainly composed of 7 $O_{(ob)}$ and 1 $O_{(obts)}$, the CN of $O_{(obos)}$ are less than 0.2 which can be neglected. It means that a small amount of sodium ions gather in the ditrigonal cavities and most of them widely distribute in the interlayer and directly connect the neighboring clay platelet in the main form of $O_{(ob)}$-Na-$O_{(ob)}$. Fig. III .4(b)-III .4(d) show the ion-water oxygen and ion-clay surface oxygen partial radial distribution function g(r) and the coordination number (CN) around Na^+ for different hydration systems. From the data obtained, a number of significant remarks can be drawn. For the hydrated model, the interaction of Na-$O_{(ob)}$ is almost completely replaced by the Na-$O_{(w)}$, except the one-layer hydrated state which the first small peak located at about 2.58Å and has only 0.5 coordination number of $O_{(ob)}$. However, it is interesting to see that the peak of Na-$O_{(obts)}$ in all cases with water is located at 2.38 r A which is bigger than the peak at dry state while the CN of one-layer hydrated system decrease from 1 to 0.5 for two- and three-layer hydrated model, the above analysis shows that the interaction between counterions and clay surface mainly consist of Na-$O_{(obts)}$ for hydration system and is weakly affected by the level of hydration. Besides, the first peaks of the RDF of Na-$O_{(w)}$ are also located at 2.38Å for three different hydration systems while the CN are respectively 3.5,5 and 5.5 for one-layer, two-layer and three-layer hydrated system. Therefore, the sodium coordination

number (CN) in the first shell is 5 for one-layer hydrated system (3.5 $O_{(w)}$, 1 $O_{(obts)}$ and 0.5 $O_{(ob)}$), 5.5 for two-layer hydrated system (5 $O_{(w)}$ and 0.5 $O_{(obts)}$) and 6 for two-layer hydrated system (5.5 $O_{(w)}$ and 0.5 $O_{(obts)}$). There is a lack of consensus on the coordination number of the first hydration shell of Na^+. whereas coordination number ranging from 4.0 to 8.0 has been reported from experiments (Ansell et al., 2006) and numerical calculation (Boek and Sprik, 2003; Mignon et al., 2010; Ohtaki and Radnai, 1993; Sp r angberg and Hermansson, 2004; Tongraar et al., 1998).

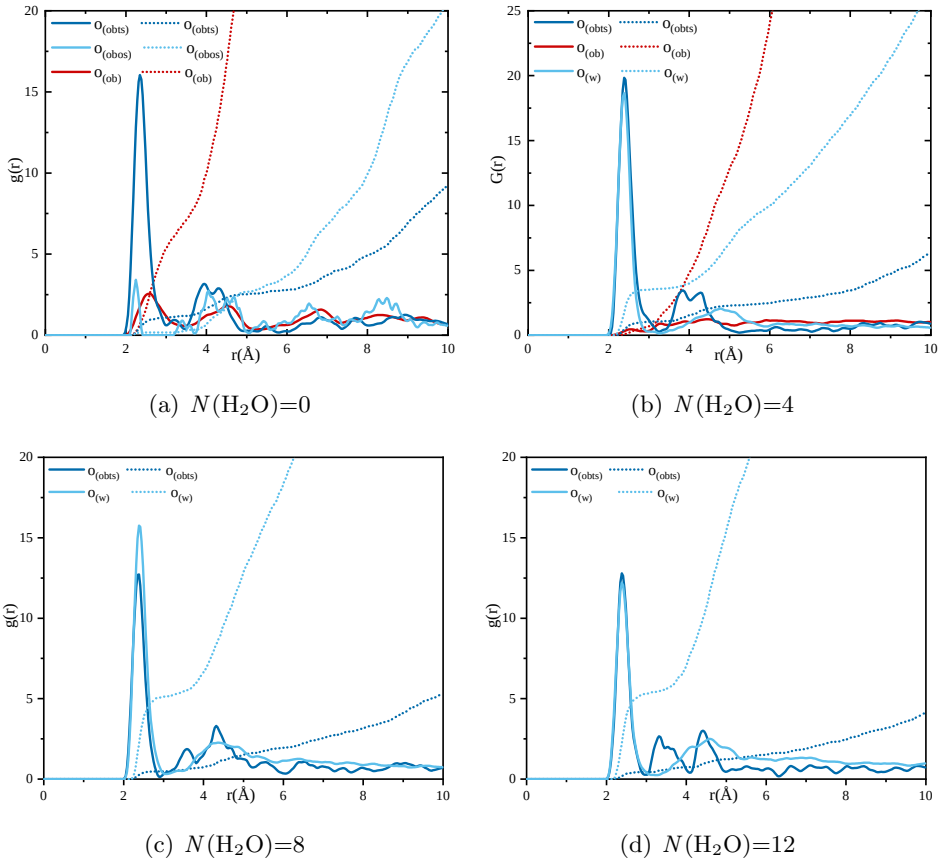

(a) $N(H_2O)$=0 (b) $N(H_2O)$=4

(c) $N(H_2O)$=8 (d) $N(H_2O)$=12

Figure III .4: RDF and CN between the Na cations and the oxygen atoms in the water and oxygen atoms on the clay surface at equilibrium structure

Our results is total consistent with previously publication (Zhang et al., 2014b). The variations in the coordinated oxygen atoms result in different link between neighboring clay platelet. For hydration systems, the interlayer distance expanded with the introduction of water into the inter-layer region, leading to the reduce of electrostatic interactions between the negatively charged layers and sodium ions while simultaneously solvating the free cations in the interlayer. Meanwhile, a hydrogen-bonded network of water within the

inter-layer will be developed resulting in a hybrid and complicated joint of hydrogen and ionic bonds in the interlayer region, when the water content further increases, multiple layers of water molecules are packed in the interlayer. In this case, the structural water molecules can play another key role in bridging near clay platelet.

3.5 Hydrogen bond network

The previous discussion describes the interlayer link of cation-clay surface for dry and hydration systems, the H-bond network as another key factor having an impact on the mechanical properties is also need to be further studied. The widely used geometric norm for hydrogen bonds is considered that the distance between the O atoms of the hydrogen donor and acceptor molecules is shorter than 3.5 r A, and the angle formed between the vector connecting those O atoms and vector connecting the O and H atoms of the donor molecule is lower than 30°. A hydrated montmorillonite system typically displays various configurations of the hydrogen bonds, it is possible to distinguish two types of hydrogen bonds in our studied systems based on this geometric rule: (1) H-bonds involving water molecules which means both the donor hydrogen and the acceptor oxygen atoms are from water molecules, denoted as $H_{(w)}$-$O_{(w)}$ bonds. (2) H-bonds formed between clay surfaces and water molecules occurs in two ways: the one is that the donor hydrogen $H_{(w)}$come from water molecules and the acceptor oxygen atoms $O_{(s)}$ come from clay surface. Meanwhile, the hydroxyl functional groups on the clay surface can also act as the donor hydrogen to form H-bond with the oxygen of water molecular, but we didn't make a detailed distinction for these two hydrogen bonds, because they both indicate the water molecules are adsorbed on the clay surface forming the clay-water complex. Thus, the H-bonds between clay and water can be called $H_{(w)}$-$O_{(s)}$ bonds. we analyze in detail the nature and extent of H-bonding within the balanced MMT structures, the average number of hydrogen bonds per water molecule is shown in Fig. III .5(a), Compared to bulk water which can form about 3.5 hydrogen bonds per water molecular, the average number of hydrogen bonds per water molecule reduces significantly due to the confinement. Per water molecules form, on average, about 0.6 H-bonds primarily with the bridging oxygen or hydroxyl on the clay surface and 0.45 H-bonds with water molecules at low hydration levels. With increasing water content, the $H_{(w)}$-$O_{(s)}$ H-bonds for per water molecular decrease while the change of $H_{(w)}$-$O_{(w)}$ is opposite. Meanwhile, the total number of H-bonds for per water molecules is greater one. In other words, some water molecules are bonded with more than one water molecule or bridging oxygen or hydroxyl on the clay surface, forming a H-bond network. For a better understanding of the H-bonds distribution in the interlayer region, we also

calculated the variation of the number of hydrogen bonds in a unit cell, shown in Fig. III .5(b).

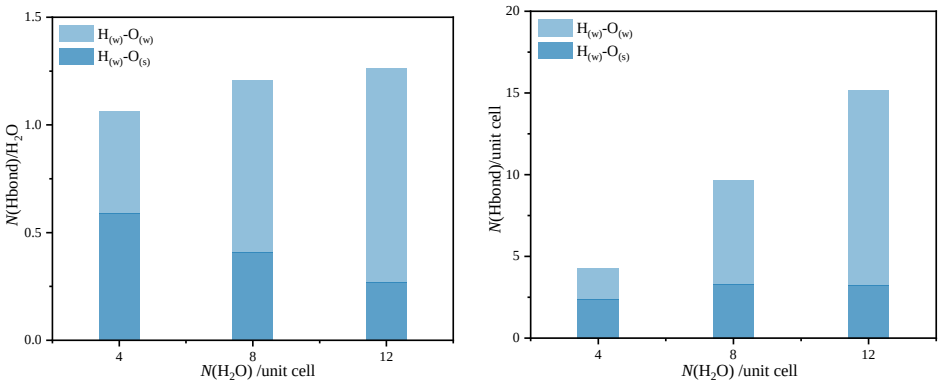

(a) Hbonds number for per water molecule (b) Hbonds number for unit cell

Figure III .5: Average number of hydrogen bonds

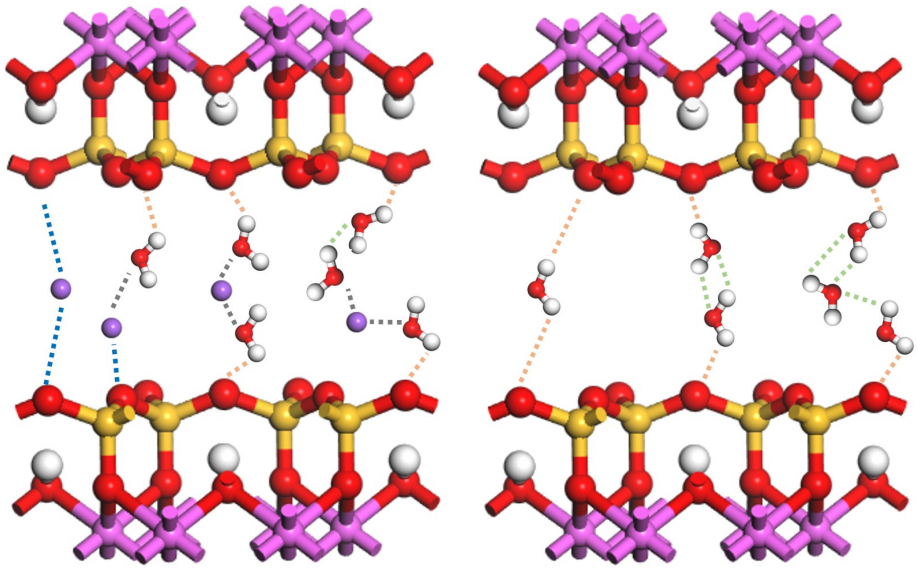

(a) Connection between cation and clay layer (b) Connection of hydrogen bonds

Figure III .6: Schematic diagrams of the interlayer connection

It can be obtained, the total number of H-bonds for unit cell increases with water content because of the much more water molecular in the interlayer region. At low hydration levels, the H-bond network is dominated by the bonds between the water and clay layer which means most of water molecules arranged on the clay surface and the rest

float between layers, Consequently, the clay platelets attains a compact structure with small interlayer distances. Some $H_{(w)}$-$O_{(s)}$ bonds can be distributed across the interlayer region and directly bridge the adjacent clay platelets. With increasing water content, the water molecules in the interlayer region transform from single-layer to multi-layer packing, the H-bond network is dominated by $H_{(w)}$-$O_{(w)}$ bonds. The clay platelets are now well-separated and do not interact directly with each other; Instead, the water connects indirectly to the surface water molecules by $H_{(w)}$-$O_{(w)}$ bonds. It is worth noticing that the number of $H_{(w)}$-$O_{(s)}$ bonds is 3.26 hydrated model while it is 3.22 for three-layer hydrated model which can illustrate the sequence of water molecules near the clay surface is orderly and directional for the two-layer hydrated system. The evolution of H-bond types and the connection between cation and clay surface also influence the bridging approach between nearby clay platelets, as schematically illustrated in Fig. III .6(a) and Fig. III .6(b).

3.6 Energy evolution

The key to understand the mechanical properties of MMT with water lies in examining the collective behavior of stacked clay platelets and cohesion between layers under loading. The decrease of the mechanical properties in the hybrid systems can be attributed to change of the molecular structure that modify the interaction among these parts. In our montmorillonite system with water, there are six kinds of interactions: clay-clay, cation-cation, water-water, cation-water, clay-cation, clay-water. For clarity and simplicity, we classify cations and water as interacting with clay as a whole called solution. Therefore, the interaction energy of systems can be treated as three parts: clay-clay(c-c), solution-solution(s-s) and clay-solution(c-s). The energy reduction of clay-clay represents the deformation of clay layer, the other two type interactions imply interlayer cohesion between clay layers. More precisely, the interaction of solution-solution mainly include the Coulombic and van der Waals force between water molecules and cations and the interaction of hydrogen bonds among water molecules, it's decrease of energy mainly due to a rearrangement of coordination shells around the cation and the decrease in the number of hydrogen bonds or stretching the movement among water molecules. Besides, the interaction of clay-solution can be described by the relevant non-bonding terms between charged clay layer and cations and the hydrogen-bond network between water molecules and oxygen on the clay surface. With the objective to understand the failure mechanism of different hydration systems, the rate of change of these different interactions which governs the mechanical properties are monitored separately during whole loading process, which is plotted with solid line as a function of the axial strain in Fig. III .7(a), Fig. III

.7(b), Fig. III .7(c), Fig. III .7(d). To clearly understand the effects of water, the change rate of the number of hydrogen bonds with axial strain are also noticed which is drawn in dotted line. Explanatory, the $H_{(w)}$-$O_{(s)}$ represents the hydrogen bonds between water and clay surface and the $H_{(w)}$-$O_{(w)}$ is the hydrogen bonds among water molecules. Positive values represent a decrease in the interacting energy.

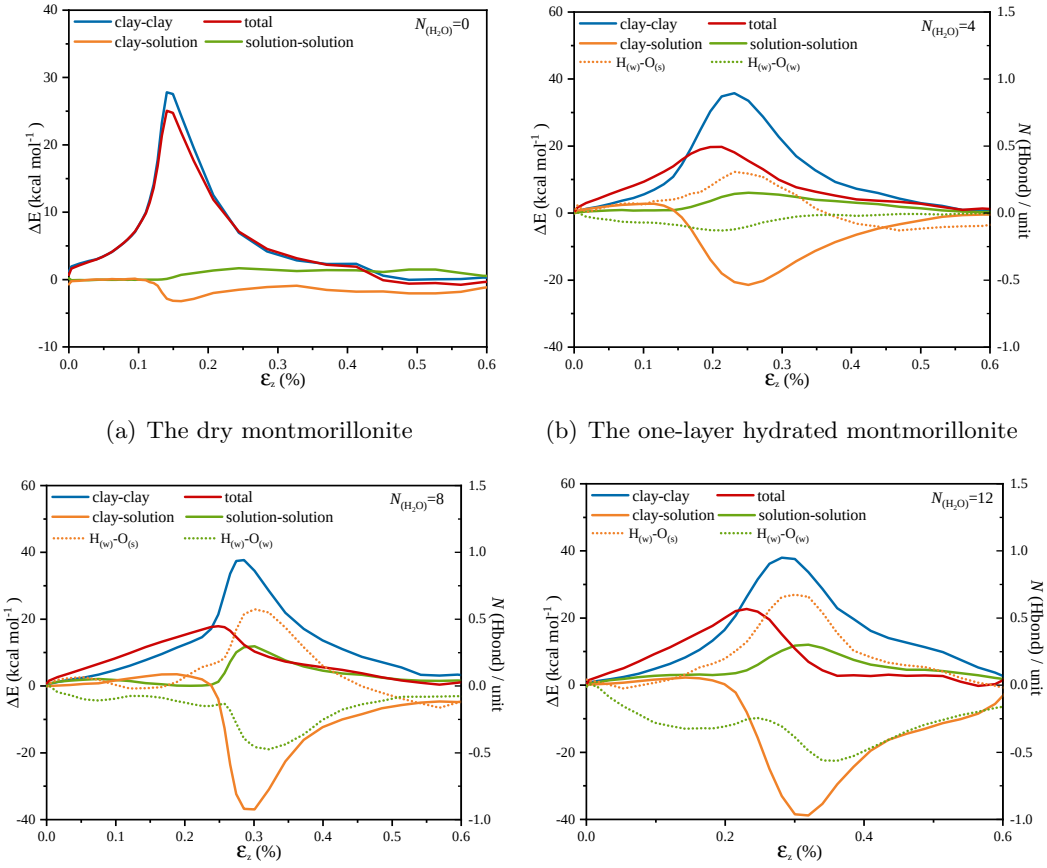

(a) The dry montmorillonite

(b) The one-layer hydrated montmorillonite

(c) The two-layer hydrated montmorillonite

(d) The three-layer hydrated montmorillonite

Figure III .7: The energy evolution with strain under compression

The clearly and common conclusion can be obtained that the clay platelets contribute the main mechanical strength for the different hydration systems while the proportion of contribution and their variation characters with respect to axial strain are significant differences because of the strong inductivity of c-s interaction. At the dry state, the interlayer cohesion energy is almost constant in the region of axial strain less than 0.1 and the decrease of c-c interaction is relatively slow mainly due to the lateral movement. Afterwards, the rate of reduction of c-c interaction is rapidly accelerated along with the sharp increase of c-s interaction, suggesting the inter-laminar sodium move toward clay surface form

stronger ion bond with the oxygen on the clay surface to resistance external loading while the traction of Na^+ on oxygen atoms causes accelerated deformation of the clay platelets until to the peak change of total energy which means the failure of model. Then, both the c-c and the c-s interaction change synchronously at a slower rate until the interaction energy almost keep constant. In the compression loading process, the significant energy change of clay platelets implies that the clay skeleton are the main contributors to the mechanical performance of dry montmorillonite. With the introduction of water molecules, the relative importance of cohesion energy to mechanical strength increases significantly. For the one-layer hydrated system, the cohesion energy is dominated by the interaction of c-s at the initial stage until it decreases to the minimum while the slight change of s-s interaction which shows the large space between clay layer and solution is compressed at first causing the stretching movement of H-bonds($H_{(w)}$-$O_{(s)}$) and Na-O bonds while the solution does not deform largely. Besides, the c-c interaction energy decrease slowly when the axial stress is less than 0.1 which can be regarded as the elastic region. With the increase of axial strain, the c-s interaction increase sharply due to the formation of new H-bonds between clay layer and interlayer water and the c-c interaction decrease rapidly at the same time, indicating the strong inductivity of c-s interaction to c-c deformation. In addition, the s-s interaction energy decreases fast after elastic region which is related to a rearrangement of coordination shells around the cation and the stretching and breakage of H-bond network among water molecules. This process can be clearly observed in the video. With the increase of water content, the water molecules are almost distributed throughout whole space between clay platelets resulting in the deformation of solution once the external load is applied which can be clearly observed both in the two-, three-layer hydrated systems. It's interesting noting that reduction rate of c-s interaction energy is less than that of s-s before the axial strain reaches a level of 0.12 and then exceeds. The s-s interaction energy which decreases slightly from initial to almost keep constant when the axial strain ranges from 0.16 to 0.24. This behavior occurs only in systems with two water layers can be understood as follows, when the structure is hydrated with one-, three-layer water molecules between clay platelets, any macroscopic deformation essentially translates to stretching of interlayer H-bonds. However, when there are two layers water present in the interlayer space, H-bond stretching is not the sole and main mechanism for accommodating deformations. Since the water molecules possess rotational degrees of freedom, they can also reorient themselves causing the breaking and forming new H-bonds, which can also be regarded the conversion of H-bonds type, in response to the external load. The reorientation of water molecules thus leads to the smaller strain and more orderly

arrangement in H-bonds network. As the continuous loading of external load, the ordered H-bond network among water molecules is much easier to be broken resulting in the hastily decrease of s-s interaction. In addition, the number of H-bonds between clay and water increase rapidly inducing the accelerated deformation of the clay layers. Therefore, the stable layers of water molecules is the main reasons for the high peak strength and axial strain of the two-layer hydrated system, there is also research published the same view that the full double-layer hydrated state is the most thermodynamically favorable one (Zhang et al., 2014b). Similarly, the increase rate of c-s interaction energy decrease rapidly causes the decrease rate of s-s interaction energy increase rapidly after the model is failure, which is account for the faster stress drop than one-layer hydrated state in the post-peak region. Therefore, the impact of water molecules on the mechanical property is more dependent on how they arrange in the inter-laminar space structure, which decided how the hydrogen bond breakage and formation and how to induce the clay deformation. The variation of interaction energy at three-hydrated state also provides intuitively and effectively evidences to understand the transformation of structure during loading. At first, the synchronous reduction of these three different interaction energy represent the deformation of whole model, including clay platelets, solution and the space between them. The s-s interaction plays a dominant role in the contribution of cohesion energy to the mechanical property mainly due to the hydrogen bonds network is dominated by hydrogen bonds among water molecules. The gradually improvement of s-s interaction in the contribution to mechanical properties from one-layer to three-layer hydrated state is almost identical to the conversion of dominant hydrogen bond type analyzed in the previous section, which proves the dominant role of H-bond network, comparing to the Coulombic interaction energy between cation and oxygen, in the hydrated systems during triaxial compression with constant mean stress. Further, it is interesting to see that the curves trend for c-s interaction(orange solid line) and $H_{(w)}$-$O_{(s)}$(orange dotted line) shows completely the same trend while the great difference between s-s interaction(green solid line) and $H_{(w)}$-$O_{(w)}$(green dotted line) at hydration state, which stresses that the contribution of c-s interaction almost come from the hydrogen bonds between clay surface and water while the s-s interaction contribution to mechanical property is the combination of hydrogen network among water molecules and ionic interaction between cation and oxygen in water molecules. Finally, when the rate of energy change reaches to its peak and then starts to drop until fluctuates around a constant value, which means the entire loading process. Based on the variation of interaction energy during compression, the effects of hydration extent on the mechanical properties can be obtained clearly. The

overall mechanical behavior of the hydrated montmorillonite system is governed by the combination of three different types interactions dominated by clay layers. In the dry sample, the deformation of clay layer is induced only by the interlayer cations through pulling coordinated oxygen atoms on the clay surface. Nevertheless, the Coulomb interaction is gradually replaced by the hydrogen bond network, which become the main factor affecting the clay layer. In addition, the influences of H-bonds depends more on the arrangement rather than the number of hydrogen bonds. In past researches that have been published, the tension and shear are the most commonly used loading path in current published researches for the mechanical property of paper-like material, most of them focuses on the cohesion between layers. Indeed, during this simple loading path, the layers suffers very limit deformation, the elastic modulus and fracture strength are almost decided by the interlayer structure. However, during triaxial compression with constant mean stress, the contribution of the clay layers to the mechanical properties becomes the most important based on our study.

4 Conclusions

In order to investigate the effects of water content on the mechanical property and the failure mechanism of clay-rich materials, we have employed atomistic simulation methods to study the molecular structure, mechanical behavior and the molecular forces governing the strength of montmorillonite at different hydrated states. The following conclusions can be drawn.

(1) The basic mechanical property of montmorillonite under the compression with constant mean stress can be characterized by a short linear elastic phase followed by a large nonlinear plastic phase until the peak strength is reached. In the post-peak regime, a sharp or smooth material softening phase is observed until residual strength is attained. However, it's mechanical property is very sensitive to the extent of hydration. Generally, the water molecules decreases the mechanical strength and increases the deformation property, leading the peak strength increases with the increase of water content while the performance of peak axial strain and compressive volumetric strain shows oppositely except the two-layer hydrated system which has higher peak strength than one-layer hydrated system and the biggest peak axial strain and compressive volumetric strain.

(2) During the process of compression, the change of structural characteristics of the montmorillonite systems have provided an important signal for understanding the features of failure. At first, the clay layer have been compressed obviously for all the systems while

the interlayer structure changes differently. For dry state, the distribution of cations between layers did not change significantly. However, the cation in the hydrated system shows the tendency to move away from the clay surface. In addition, the interlayer water molecules prefers to form more ordered triple-peak structure which represents the hydrogen bond type transition and breakage.

(3) Structurally, the clay layers are connected by the electrostatic interactions between Na^+ and oxygen on the clay surface for the dry state. As the water content increases, the bridging interaction between the clay layers become the combination of electrostatic and hydrogen bonds interactions which is dominated by hydrogen bonds. The different connections between layers is not only decided the interlayer cohesion energy, but also have the key impact on the deformation of clay layer induced by cation and H-bond network.

(4) In the process of triaxial compression with constant mean stress, the deformation of clay platelet and interlayer connection variation determine the mechanical properties evolution. clay layer, as the most stable backbone of montmorillonite system, contributes the primary mechanical strength. However, the deformation of clay platelet is strongly induced by the variation of clay-solution interaction which is mainly caused by the hydrogen bonds between clay and water for hydrated state while ion interaction between cation and oxygen in the dry state. In addition, the change of clay-solution interaction is also related to the evolution of solution-solution interaction due to the conversion of hydrogen bond types. Therefore, the stability of interlayer cation and water molecules shows the critical impact on the mechanical property because of the 'competition' among these three interactions even though a relatively small contribution to mechanical strength.

Chapter IV

Molecular dynamics study on creep deformation of montmorillonite

1 Introduction

During the last few decades, the macroscopic time-dependent deformation and failure of clay-rich rocks, as a potential geological barrier for subterranean radioactive waste disposal, has been extensively studied because of it's long-term security requirements(Armand et al., 2013; Belmokhtar et al., 2017; Liu et al., 2018a; Zhang, 2018; Zhang et al., 2019). For instance, the creep strain rates of COx claystone have proven to be the order of 10^{-10} to 10^{-11} when it is loaded with a relative low deviatoric stress like 10 MPa (Vales et al., 2002). (Liu et al., 2018a) explored systematically the effects of relative humidity, mineral compositions, anisotropy and confining stresses on the creep behaviors of claystone by the triaxial compression. The complete creep curves, including primary, steady and tertiary creep stage are obtained and concluded that confining stress increase creep strain. The clay minerals especially the smectite play an crucially role in increasing the creep strain at a certain relative humidity. Further, at high deviatoric stress levels, failure due to acceleration creep was also observed. These accomplishments have contributed to the basic knowledge of the creep properties and confirmed the diverse factors influencing the creep behavior of clayey-rich rocks. According to previous laboratory studies, local deformation mechanisms of clay particles and aggregates at the nanometer and micrometer scales generate macroscopic plastic deformation (Bornert et al., 2010). However, it is quite challenging to perform direct experimental measurement at such small scales in view of

identifying those mechanisms. In recent years, the rapid development of molecular dynamics(MD) and wide application in clay-rich materials provides an effective means for the study at nanoscale. MD was first used to investigate hydration-related swelling behavior, structural distribution, and water molecule or cation ion diffusion between layers (Boek et al., 1995b; Yeh and Hummer, 2004). Afterward, works on the mechanical property of clay minerals with MD have been reported gradually and obtained a serious valuable results, such as the elastic property and failure mechanism. However, in most previous studies, MD simulations were performed on crystal samples subjected to the loading paths like uniaxial compression, tension, triaxial compression with constant confining stress and triaxial compression with constant mean stress in clay-rich rocks field. As a matter of fact, due to the demand for the safety of high level radioactive waste disposal for hundreds of years, it is crucial to study the long-term deformation and failure mechanism (Zartman et al., 2010; Zhang et al., 2015; Zhu et al., 2021). To the best of our knowledge, the creep property of clay-rich materials have so far not been investigated at nanoscale by MD while it is widely used to explore the creep mechanism and determine the factors affecting the creep properties in metals field(Jiao and Kulkarni, 2015), such as temperature, applied stress and so on. It is also used to search nanoscale origins of creep in calcium silicate hydrates(Morshedifard et al., 2018). In this study, we shall perform atomic simulations on Na-montmorillonite with constant uniaxial stress under different temperature, applied stress level and loading orientation to identify the basic deformation and failure features and then to build the links between microscopic and macroscopic behaviors.

2 Computational method

Molecular dynamics (MD) is the computational method applied in this case. As in most prior MD simulation research, atoms are considered as basic particles. Inter-atomic potentials (force fields) that contain bonded and non-bonded interactions generate the forces acting on the atoms, and atomic movement is governed by Newton equations of motion. This section introduces the different steps of MD simulations employed in this study.

2.1 Crystal structure

The crystal structure considered here is based on the natural Wyoming MMT (Boek et al., 1995a,b; Chang et al., 1995). The unit cell formula is as follows:

$$Na_{0.75}nH_2O[Si_{7.75}Al_{0.25}][Al_{3.5}Mg_{0.5}]O_{20}(OH)_4. \qquad \text{(IV .1)}$$

The space group of unit cell is C2/M, monoclinic system, with a=5.23A, b=9.06A, c=9.6A, $\alpha = \gamma$=90° and β=99°. It is distinguished by a TOT (tetrahedron-octahedron-tetrahedron) layer made up of sheets of silica tetrahedra and alumina octahedra. The layer is negatively charged because of the isomorphous substitution which means the Al^{3+} in the octahedral sheet are substituted by Mg^{2+} and Si^{4+} in the tetrahedron sheet are substituted by Al^{3+}. Specifically, one of thirty-two Si^{4+} is replaced by an Al^{3+} and one of eight Al^{3+} is replaced by an Mg^{2+}. To keep the electrically neutral of model , the negative charge is balanced by the incorporation of Na cations in the inter-layer space. In addition, the eight water molecules are introduced into the interlayer space of each unit cell representing the hydrated model with water content of twenty percent. The model used in this study is shown in Fig. IV .1, it is an 8*4*4 super-cell and the total number of atoms in simulation cell is 5216.

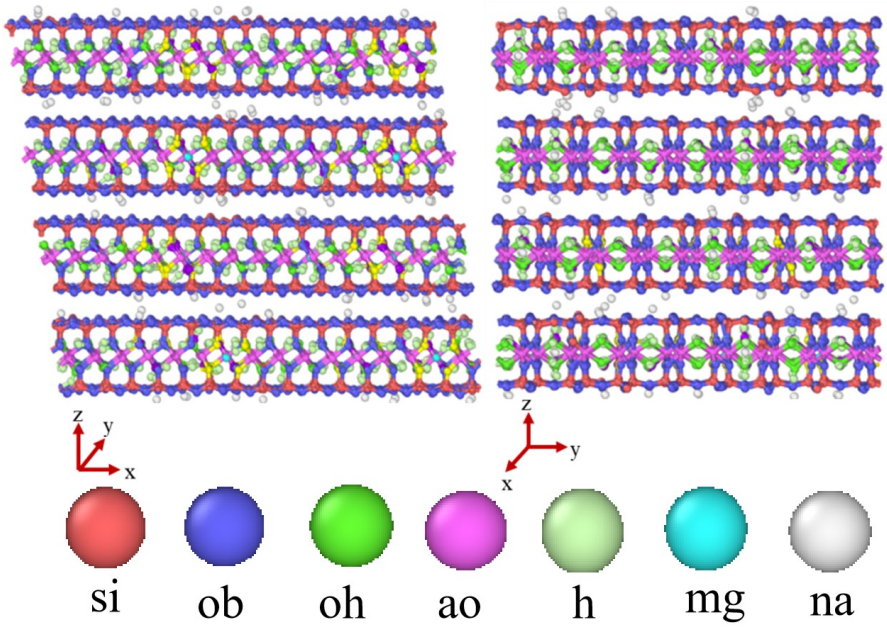

Figure IV .1: Atomic structure of Na-montmorillonite at two-layer hydrated state

2.2 Force field

The interatomic interactions in crystal systems are described by forces fields which are derived from energy potential functions. In the present study, the CLAYFF force field developed by (Cygan et al., 2004). is adopted. This force field is widely accepted because it has been shown to be highly effective in modeling the crystal structure with a number of different clay, mobility of interlayer water because of the huge advantage of

providing atoms with complete translation freedom. Recently, it has also been frequently utilized to investigate the mechanical behavior of clay and has aided in the understanding of fundamental mechanical mechanisms at the atomic level. The total potential energy (Etotal) is composed of the Coulomb interactions (ECoul), the van der Waals interactions (EVDW) and the bonded interactions. The bonded terms include the bond stretch energy (Ebond strech) and the angle bend energy (Eangle bend) that is used in water and metal with hydroxyl. One gets:

$$\begin{cases} E_{total} = E_{Coul} + E_{VDW} + E_{bond-strech} + E_{angle-bend} \\ E_{Coul} = e^2/4\pi\epsilon_0 \sum_{i\neq j} q_i q_j / r_{ij} \\ E_{VDW} = \sum_{i\neq j} D_{0,ij}[(R_{0,ij}/r_{ij})^{12} - 2(R_{0,ij}/r_{ij})^6] \\ E_{bond-strech} = k_1(r_{ij} - r_0)^2 \\ E_{angle-bend} = k_2(\theta_{ijk} - \theta_0)^2 \end{cases} \quad \text{(IV .2)}$$

r_{ij} is the distance between the atoms i and j. In the Coulombic energy, e is the charge of an electron, ϵ_0 is the dielectric permittivity of a vacuum ($8.85419 \times 10^{12} F/m$) and q_i and q_j are the atomic partial charges, which can be derived from quantum mechanics calculations. In the Van der Waals energy, the terms $D_{0,ij}$ and $R_{0,ij}$ are calculated by:

$$\begin{cases} R_{0,ij} = 1/2(R_{0,i} + R_{0,j}) \\ D_{0,ij} = (D_{0,i} * D_{0,j})1/2 \end{cases} \quad \text{(IV .3)}$$

About the $(O-H)$ bond stretch energy, k_1 defines a force constant and r_0 represents the equilibrium bond length. Finally for the angle bend energy, k_2 is a force constant, θ_{ijk} denotes the bond angle for the mental-oxygen-hydrogen and θ_0 is the equilibrium bond angle.

2.3 MD simulation procedure

A parallel molecular dynamics code Lammps (Plimpton, 1995) is used to perform simulations on the crystal structure of Na-Montmorillonite defined above. The samples are first relaxed at the desired temperature for 200 ps using an NVT (number of atoms, volume, and temperature) ensemble, then independently relaxed in three directions for another 200 ps using an NPT (number of atoms, pressure, and temperature to mimic

bulk behavior) ensemble with zero pressure in all directions. The goal of these relaxation processes is to evenly distribute the surplus free energy throughout the system. This model is used as a starting point for mechanical loading. In order to study the the impact of temperature, applied stress and the anisotropy on the creep deformation of MMT, the sample is subjected to different levels of applied stress along the x direction and z direction respectively while other two directions were exposed to zero pressure at temperature ranging from 300 K to 1200 K for 200ps. Finally, the corresponding creep curves are obtained to explore the creep mechanism at nanoscale.

3 Results and discussion

3.1 Conventional uniaxial and triaxial compression

In order to investigate creep behaviors of Na-MMT at dry and hydrated state, there is an key issue is about the selection of applied stress. Based on the method of macroscopic creep experiments, the short-term mechanical strength can be as a reference (Liu and Shao, 2017). Therefore, we first perform conventional shear loading on them in Z direction for selecting an appropriate applied stress. There are three sets of tests. The dry and hydrated montmorillonite are subjected to uniaxial compression along the z direction and the hydrated model is subjected to triaxial compression with a confining pressure of 5 GPa. The stress-strain curves are shown in the Fig. IV .2.

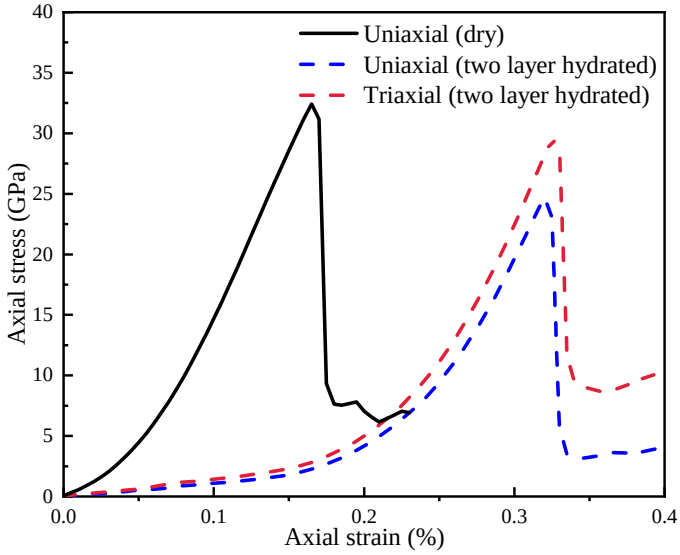

Figure IV .2: Stress-strain relationship of MMT

It can be obtained that the peak deviatoric stresses are 32.5 GPa at dry state under uniaxial compression, 24.744 GPa under uniaxial compression and 25.5 GPa under triaxial compression with confining pressure of 5 GPa in Z direction, these results are great well with the previous report (Han, 2020) that the uniaxial ultimate stress at the dry state and the two-layer hydrated state along the Z direction are 33.74 GPa and 25.1 GPa, respectively. Based on this, the planed deviatoric stresses level , such as 50% 60% 65% 70% 75% 80% and so on, are applied. In addition, for study the effect of temperature on creep behavior, the uniaxial creep test is performed on the hydrated Na-MMT in Z direction at the temperature of 600k. All our calculation are summarized in Table. IV .1

Table IV .1: Calculation program

	dry state		two-layer hydrated state				
	300k		300k				600k
	U-Com	U-Creep	U-Com	U-Creep	T-Com	T-Creep	U-Creep
50%	-	-	-	12.4	-	18	-
60%	-	20	-	15	-	20	15
65%	-	21.5	-	16.5	-	23	16.5
70%	-	23	-	17.5	-	24	-
75%	-	24.5	-	18.5	-	25	-
100%	32.5	-	24.75	-	25.5	-	-

3.2 Triaxial creep

3.2.1 Effect of deviatoric stress at two-layer hydrated state

With the objective to investigate the effects of applied stress level and the possibility of tertiary creep, a series of different deviatoric creep stress levels with constant confining pressure of 5 GPa have been calculated. According to the analysis in the previous section, The 40 percent is chosen as the minimum deviatoric stress ratio, the peak strength then

it is gradually increased at intervals of 5% of the deviatoric stress until the stress exceeds the long-term strength. Therefore, the creep tests along the z direction under the applied stress level ranging from 16 to 25 GPa. The axial strain evolutions during the creep process of the one step creep tests are shown in Fig. IV .3, the corresponding axial creep-stress curves are also plotted in Fig. IV .4.

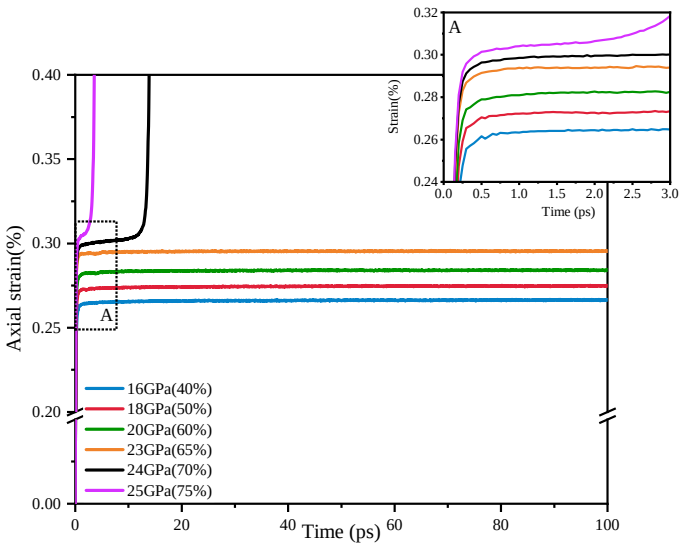

Figure IV .3: Axial strain-time curves at hydrated state under different deviatoric stress

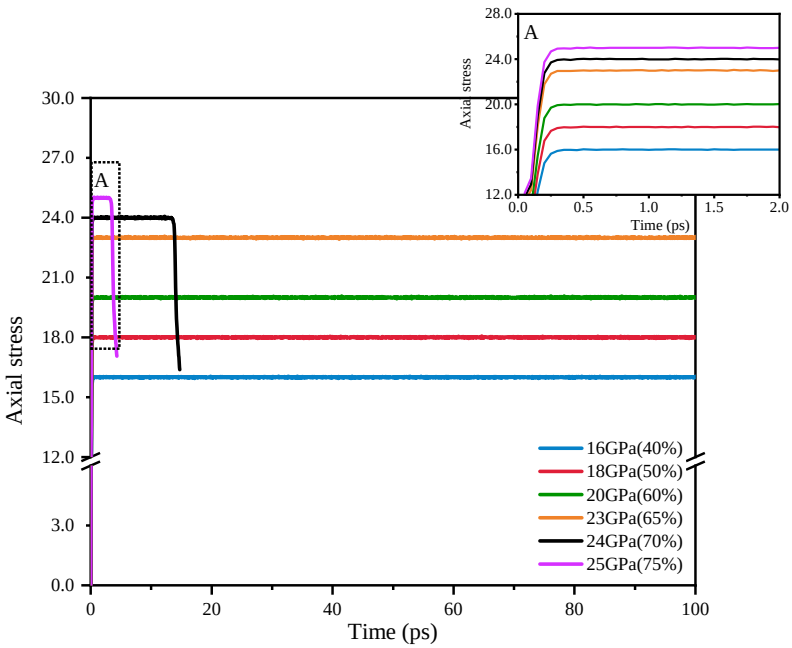

Figure IV .4: Axial stress-time curves at hydrated state under different deviatoric stress

It can be seen clearly that the planned deviatoric stress reaches absolute stability at the time around 0.3ps meaning the stress rise stage, the evolution of strain is relative slow and reaches stability about 0.5ps for the stress state of minimum, this part of the deformation will be ignored in the following analysis. From our calculation, it is evident that the deviatoric loading level has an important enhancing effect on the amount of axial creep strain of the hydrated Na-MMT during the primary and steady creep. The higher the deviatoric stress level, the greater the axial strain. Also, the axial strain curves indicate that the augmentation of the axial strain induced by the increase of deviatoric creep stress in higher stress levels is more important than that in lower levels. Moreover, the tertiary creep stage is the key to study creep failure relating to time-dependent under certain specific conditions, when the applied stress reach to the 75%, the model is broken rapidly indicating the tertiary creep stage. The time-lateral strain curves and the corresponding time-lateral stress at different deviatoric stress level are given in Fig. IV .5 and Fig. IV .6. Lateral strain shows obvious expansion behavior. Generally, it's trends with the change of deviatoric stress level revealed by the lateral strains are agreement with that of the axial strains while it is significantly smaller than that of axial strain under the low deviatoric stress level, the corresponding volume strain is always compressive due to the much small lateral strain, as illustrate in Fig. IV .7. However, it is worthy noting under the higher deviatoric stress, the volume change occurs a clear inflection point, corresponding to the

onset of the accelerated creep stage, which also indicates the model has lost its loading-bearing capacity. These findings can also be observed from the time-lateral strain curves, which indicates the dominance of lateral strain at this time.

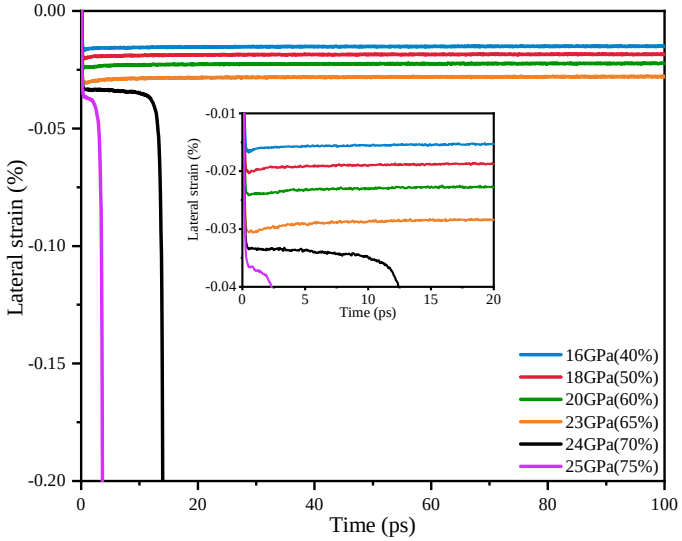

Figure IV .5: Lateral strain-time curves at hydrated state under different deviatoric stress

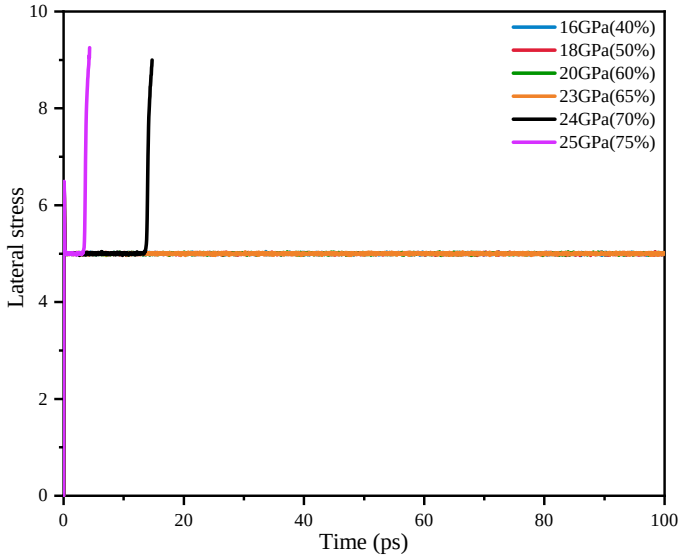

Figure IV .6: Lateral stress-time curves at hydrated state under different deviatoric stress

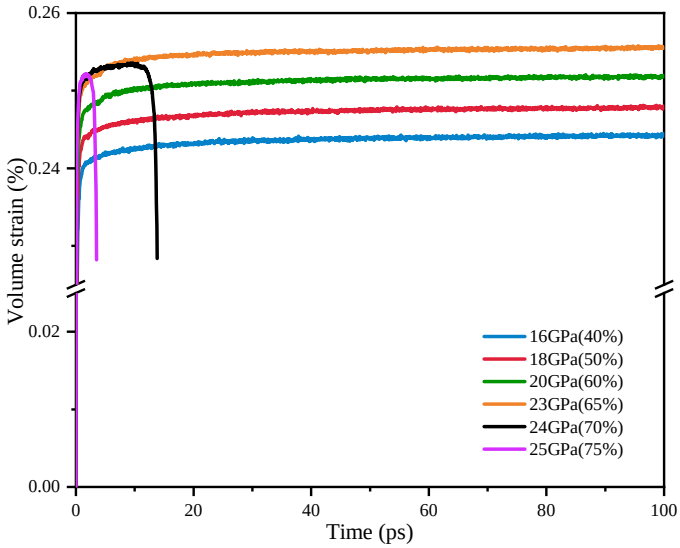

Figure IV .7: Volume strain-time curve at hydrated state under different deviatoric stress

3.2.2 Influence of confining pressure at two-layer hydrated state

In this section, in order to investigate the effects of confining pressure on creep behavior, the modes are loaded in z direction under loading path of uniaxial creep and triaxial creep with confining pressure of 5 GPa, respectively. The results of axial - strain are illustrated Fig. IV .8 and the corresponding axial - stress curves are also shown in the Fig. IV .9.

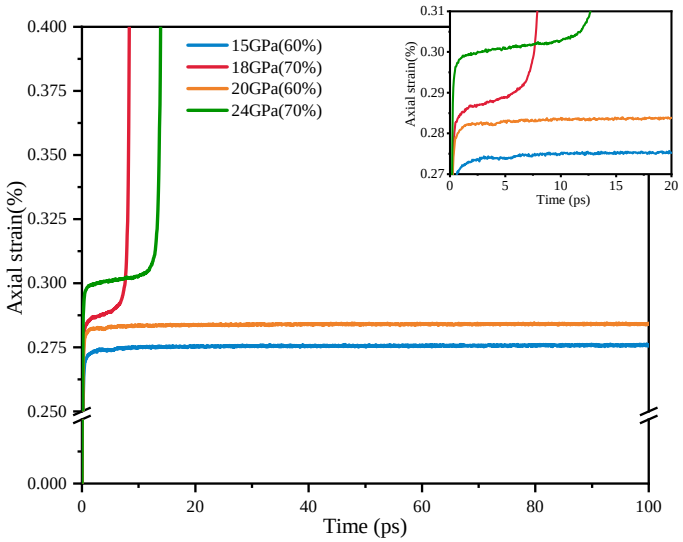

Figure IV .8: Axial strain-time behavior at hydrated state under different confining pressure

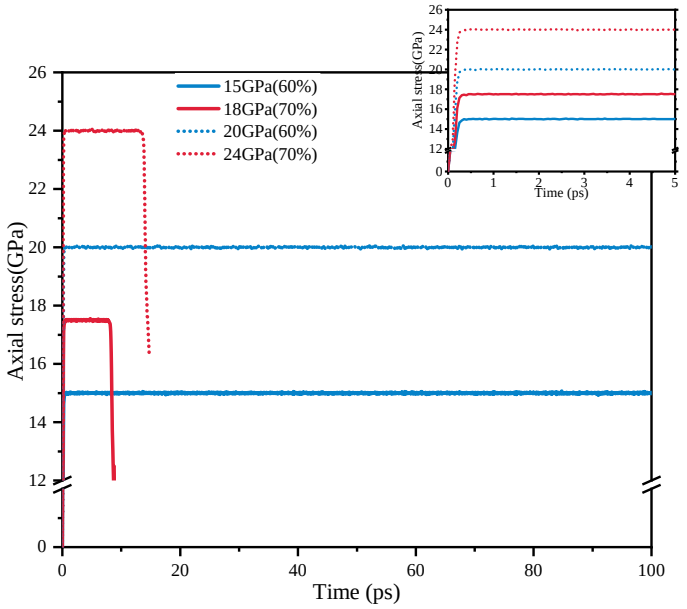

Figure IV .9: Axial stress-time behavior at hydrated state under different confining pressure

Form the time-axial strain curves during the creep process of the one-step creep tests, the axial strain caused by uniaxial compressive creep is evidently smaller than that of triaxial compressive creep under the same deviatoric stress level, due to the smaller constant axial stress. After the initial creep, the model remains in the stable creep stage under the comparatively low deviatoric stress level (i.e., q/q_{peak}=75%), while higher deviatoric stress can drive the model into an accelerated creep stage, that is, the initial damage induced by high deviatoric stress significantly reduces the stability during creep. Furthermore, the creep rate is a little higher under uniaxial condition, which is more obvious under the deviatoric stress of q/q_{peak}=75%).

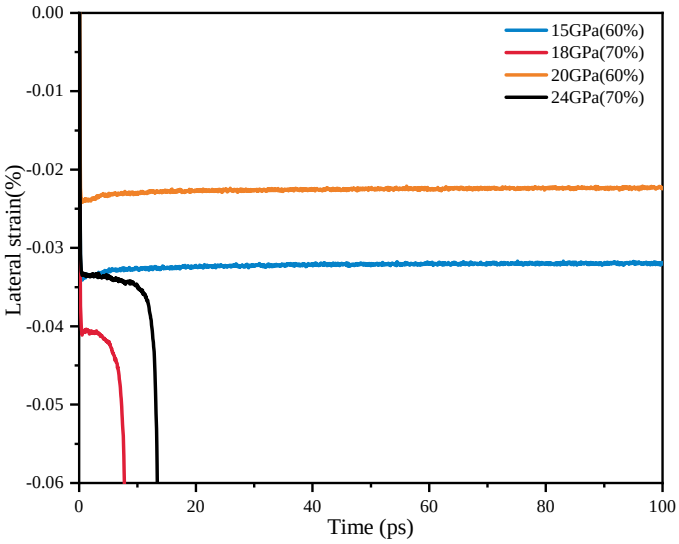

Figure IV .10: Lateral strain-time creep relationship at hydrated state under different confining pressure

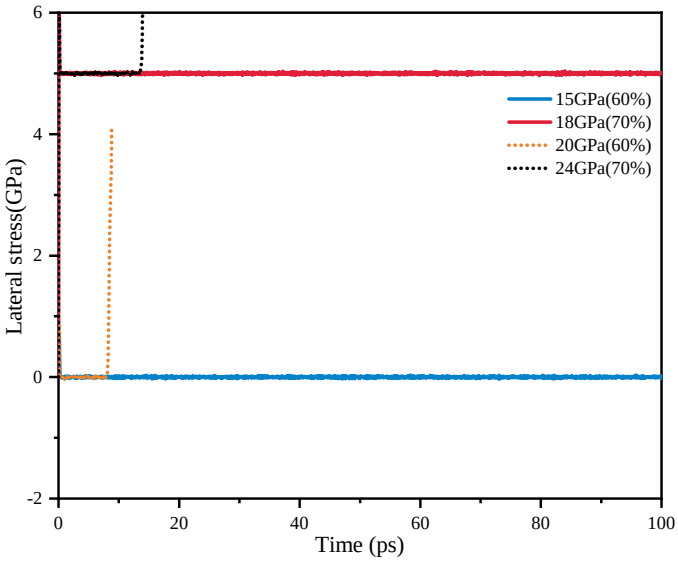

Figure IV .11: Lateral stress-time creep relationship at hydrated state under different confining pressure

The time-lateral strain curves and the corresponding time-lateral stress are given in Fig. IV .10 and Fig. IV .11 for the uniaxial creep and triaxial creep under different deviatoric stresses. The trends revealed by the lateral strains are opposite with that of the axial strains, under the same deviatoric stress ratio, the lateral strain of triaxial creep is significantly smaller than that of uniaxial creep test indicating the confining pressure

inhibits lateral deformation. The time-volume strain curves are shown in Fig. IV .12 It is worthy noting the volume of the model is always compressed under lower deviatoric stress level (i.e., q/q_{peak}=60%). However, the higher deviatoric stress can cause the volume change from compression to expansion, corresponding to the onset of the accelerated creep stage, which also indicates the model has lost its loading-bearing capacity. These findings can also be observed from the time-lateral strain curves (see Fig. IV .10). According to the lateral strain curves, the lateral expansion is more notable under uniaxial condition, indicating that the confining pressure has a strong inhibitory effect on lateral deformation.

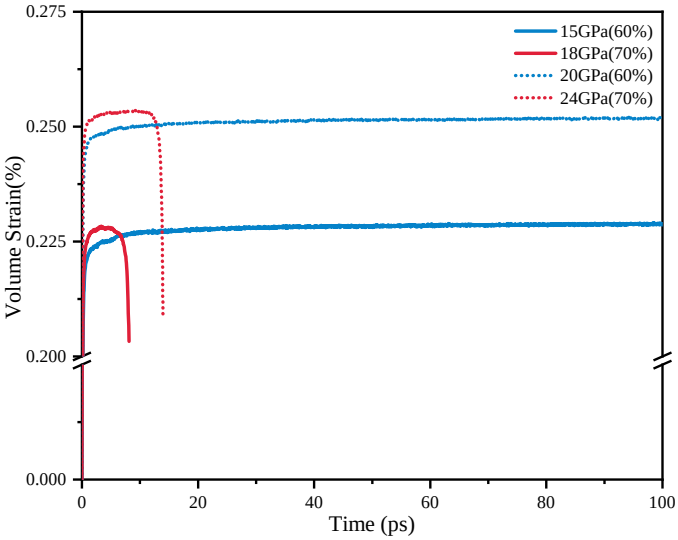

Figure IV .12: Volume strain-time relationship at hydrated state under different confining pressure

3.3 Uniaxial creep

3.3.1 Effect of temperature

Fig. IV .13 shows the creep curve of MMT at different temperatures under the applied stress of 15 GPa and 16.5 GPa along z direction. A standard creep curve contains three creep regions, including the primary stage, secondary stage, and tertiary stage is obtained at the applied stress of 16.5 GPa under the temperature of 600K, indicating the applied stress of 16.5 GPa is over the long-term strength under the temperature of 16.5 GPa. However, as presented, when the temperature is 300K, there are only two stages in the curve creep. For the creep curve with applied stress of 15 GPa, whether the temperature is 300K or 600K, the creep curve show only two stages in the time we calculated, but the creep strain of 600K is obviously greater than 300K. The reason for this scenario is that

high temperatures could accelerate creep deformation and destroy the atomic structure due to intense vibrations. Hence, it becomes easier to deform and faster destruction.

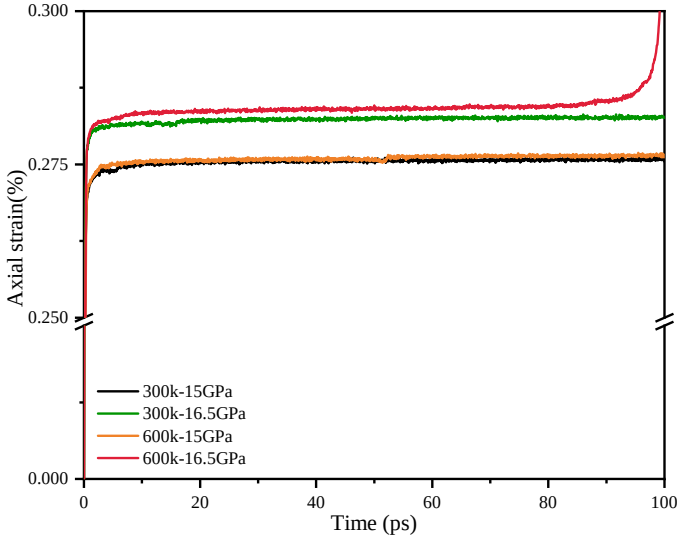

Figure IV .13: Axial strain-time relationship under different temperature

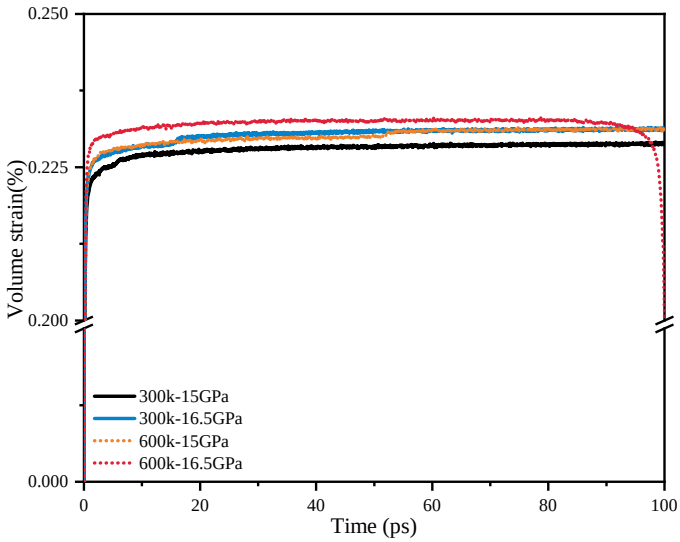

Figure IV .14: Volume strain versus time curves under different values of temperature

3.3.2 Influence of water content

For clay-rich rocks, water content can significantly affect its mechanical properties, specifically the softening effect. In this work, uniaxial creep simulations under different water content (e.g., dry state and two-layer hydrated state) were performed. Under the

same deviatoric stress level, the axial strain at two-layer hydrated state is evidently larger than that of model at dry state, as shown in Fig. IV .15. It is worth noting that, under the deviatoric stress of q/q_{peak}=70%, the model at dry state remains in the stable creep stage, while the model at two-layer hydrated state enters the accelerated creep stage relatively quickly after the initial creep. This result indicates that the effect of water content on the mechanical behavior is more pronounced at higher deviatoric stress level, suggesting that the influences of water content are strongly dependent on the stress state. In addition, the model at two-layer hydrated state has a larger creep rate. From perspective of volume strain (see Fig. IV .16), it can be found that the model is in compression for both dry state as well as two-layer hydrated state under lower deviatoric stress level, however, the model at two-layer hydrated state changes from compression to expansion under the deviatoric stress of q/q_{peak}=70%. It is conclusive that water content can reduce the stability during creep, which shows a good agreement with lab-scale experimental studies (Liu et al., 2018a)

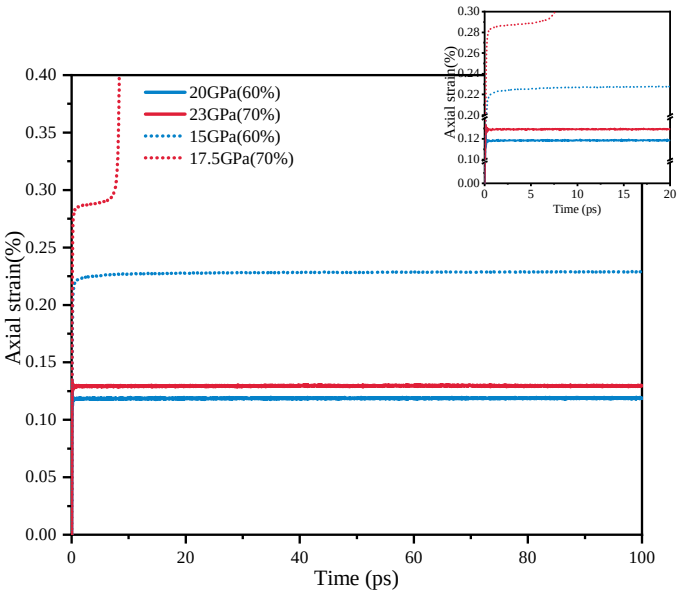

Figure IV .15: Axial strain-time relationship under dry and hydrated state

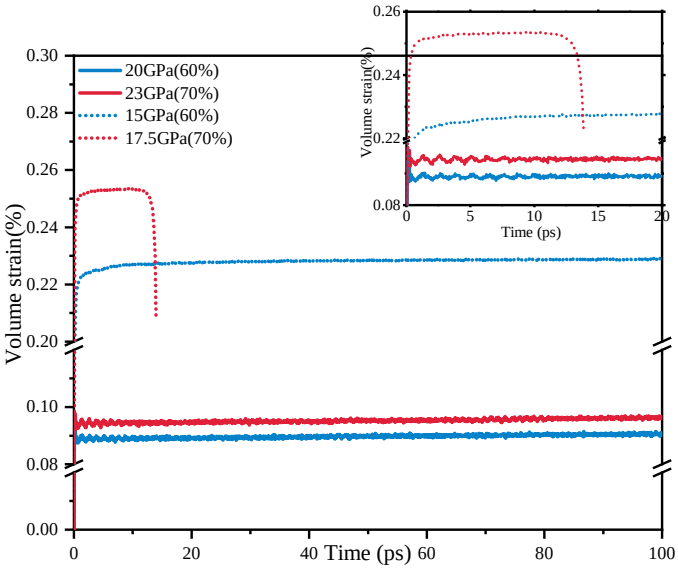

Figure IV .16: Volume strain-time relationship under dry and hydrated state

4 Conclusions

In this work, the molecular dynamics is used to identify the impact of applied stress level on the creep behavior of two-layer hydrated state under uniaxial compressive creep, temperature, confining and water content on the creep property of single crystal montmorillonite. The main conclusions can be given as follows:

The creep behavior is also strongly dependent on the confining pressure, under same ratio of q q_{peak}, the lateral deformation of uniaxial creep is significantly greater than that of triaxial creep while the axial strain shows on the contrary. the volume strains almost shows same tendency of axial strains.

Creep strain and creep rate of the hydrated Na-montmorillonite are positively correlated with the variation of the applied stress level under one-step uniaxial creep. In the steady creep stage, the higher the applied deviatoric stress level in the creep test, the more significant the creep deformation and the higher the creep rate.

Temperature has been shown to have a significant effect on creep behavior, high temperature can accelerate the movement of atoms and eventually caused large deformations and even destruction.

The creep deformation and failure strength are strongly influenced by water content. The creep strain under two layer-hydrated state is much larger than that of dry state. In addition, the mechanical strength for these two different hydrated state shows significantly

difference. Under the deviatoric stress of q/q_{peak}=70%, the model at dry state remains in the steady creep stage while the model at two-layer hydrated state enters to the tertiary stage leading failure. Also, the corresponding time-volume shows obvious difference, it goes from compression to expansion when the q/q_{peak}=70% at two layer hydrated state.

This work is an attempt to report the computational investigation of the creep behaviors of MMT by molecular dynamics simulation, the atomic-scale analysis of the creep mechanism will be helpful for the experimental design and understanding. Also, further efforts are required to overcome the limitation of timescale in MD simulations for investigating the creep-related issue.

Chapter V

Conclusions and Perspectives

1 Conclusions

In this thesis, montmorillonite, the main mineral composition of clayey rocks and clay, is selected as our research object to perform a serious of mechanical loading consistent with laboratory tests by molecular dynamics simulation. At first, the lateral decompression and axial extension test along x and z direction are applied on the dry montmorillonite to explore the effects of loading path and anisotropy on the mechanical properties. Then, the same mechanical tests are applied on montmorillonite with different hydration levels for the purpose of that the failure mechanism caused by the movement of water molecules during loading. At last, we calculate the creep behavior under varied stress levels, temperature and two orientations, the results shows the consistent tendency with the macroscopic tests. The emphasis of our work is put on the nanoscale mechanism related to the macroscopic behaviors instead of the mechanical properties observed in the experiment.

Based on the researches performed in our work, the following main remarks can be obtained.

- At the atomistic scale, the basic stress-strain relationship is comparable to that of most clayey rocks at the macroscopic scale. It has a short linear elastic phase followed by a large nonlinear plastic phase until it reaches its maximal strength (expressed by the absolute value of differential stress). In the post-peak regime, due to crystal structure instability, a sharp or smooth material softening phase is observed until the residual strength is attained.

- The loading path and orientation have a significant impact on the mechanical behavior of a single crystal of Na-MMT. Compression failure strength is systemati-

cally higher than extension failure strength in the perpendicular direction. When the mean stress is high, however, the difference is greatly reduced. Under low mean stress, compression has a little higher failure strength than extension, whereas under high mean stress, compression has a slightly lower failure strength than extension. In general, the failure strength in compression in the perpendicular direction is higher than that the parallel direction. On the contrary, the strength in extension in the perpendicular direction can become lower than that the parallel direction under low mean stress. Therefore, the general failure criterion of NoMMT crystal depends on Lode's angle, mean stress as well as loading orientation. On the other hand, the post-peak stress-strain responses are also affected by these same factors, producing brittle or ductile behavior.

- The mechanical behavior of Na-MMT crystal is further influenced by mean stress, but in a quite different manner in two loading orientations. In the parallel direction, the mean stress mainly affects the peak strength. But in the perpendicular direction, the mean stress affects not only the peak strength but also the post-peak stress-strain relationship by producing either a brittle or ductile behavior according to the value of mean stress. In a general way, the influence of mean stress is stronger in extension than in compression.

- The deformation mechanism of crystal structure until around 80% of peak strength is mainly driven by the compaction or dilation of inter-layer space. Layer structure is progressively destroyed around the peak strength and during the softening zone. A relatively stable damaged structure is found and related to the residual strength of crystal. As a first approximation, the failure of crystal structure is generated by the collapse of inter-layer space under compression in perpendicular direction and under extension in parallel direction. The sheet bending is the principal failure mechanism under compression in parallel direction and under extension in perpendicular direction.

- The basic mechanical property of hydrated montmorillonite under the compression with constant mean stress can be characterized by a short linear elastic phase followed by a large nonlinear plastic phase until the peak strength is reached. In the post-peak regime, a sharp or smooth material softening phase is observed until residual strength is attained. However, it's mechanical property is very sensitive to the extent of hydration. Generally, the water molecules decreases the mechanical strength and increases the deformation property, leading the peak strength increases

with the increase of water content while the performance of peak axial strain and compressive volumetric strain shows oppositely except the two-layer hydrated system which has higher peak strength than one-layer hydrated system and the biggest peak axial strain and compressive volumetric strain.

- During the process of compression, the change of structural characteristics of the montmorillonite systems have provided an important signal for understanding the features of failure. At first, the clay layer have been compressed obviously for all the systems while the interlayer structure changes differently. For dry state, the distribution of cations between layers did not change significantly. However, the cation in the hydrated system shows the tendency to move away from the clay surface. In addition, the interlayer water molecules prefers to form more ordered triple-peak structure which represents the hydrogen bond type transition and breakage.

- Structurally, the clay layers are connected by the electrostatic interactions between Na^+ and oxygen on the clay surface for the dry state. As the water content increases, the bridging interaction between the clay layers become the combination of electrostatic and hydrogen bonds interactions which is dominated by hydrogen bonds. The different connections between layers is not only decided the interlayer cohesion energy, but also have the key impact on the deformation of clay layer induced by cation and Hbond network.

- In the process of triaxial compression with constrant mean stress, the deformation of clay platelet and interlayer connection variation determine the mechanical properties evolution. clay layer, as the most stable backbone of montmorillonite system, contributes the primary mechanical strength. However, the deformation of clay platelet is strongly induced by the variation of clay-solution interaction which is mainly caused by the hydrogen bonds between clay and water for hydrated state while ion interaction between cation and oxygen molecules in the dry state. In addition, the change of clay-solution interaction is also related to the evolution of solution-solution interaction due to the conversion of hydrogen bond types. Therefore, the stability of interlayer cation and water molecules shows the critical impact on the mechanical property because of the 'competition' among these three interactions even though a relatively small contribution to mechanical strength.

- Creep strain and creep rate of the single crystal montmorillonite are positively correlated with the variation of temperature, the applied deviatoric stress level, confining pressure and water content. The creep deformation and creep rate are positively

correlated with water content, temperature, the applied deviatoric stress level. The rapid evolution of creep failure stage shows the brittleness of dry montmorillonite.

2 Perspectives

This work focuses on studying the mechanical properties of the clay mineral — Na-montmorillonite in order to identify the influence factors and understand the mechanism of deformation and failure at nanoscale, a series of mechanical tests have been performed based on the background of high-level waste disposal and obtain plenty of valuable insights. However, clay minerals are not always exist singly. The mixed-layer clay minerals which exhibit alternating layers with differing structures, compositions, and basal distances, or with varied layer displacement or rotation between consecutive layers are more typically found in the clay-based materials. The different layer types can co-exist in variable proportions resulting in a variety of layer stacking sequences. In general, the surface properties of mixed layer mineral particles are not strictly equal to the simple combination of the properties of their constitutive layers (Rahromostaqim and Sahimi, 2018; Sakharov and Lanson, 2013; Tournassat et al., 2015). In addition, based on the concept of high-level waste disposal in French, the waste tank is packaged by the engineering barrier which contains the swelling clay and ultra-high-performance concrete, the host rock, Callovo-Oxfordian (COx) claystone, is selected as the geological barrier. The way to splice these different materials will form three different kinds of interfaces: clay-concrete, claystone-concrete, clay-claystone. The interface can form the migration channels for the underground water and radioactive ions, it is also the weak zone of mechanical strength. Therefore, it is necessary to the evaluate the physical mechanical properties of this composite materials at nanoscale to deeply understand their interaction mechanism. This will be our research emphasizes in the near future, we will conduct our work by the following aspects orderly:

- According to the previous researches, illite-montmorillonite mixed-layer minerals are very common in clay rich rocks and have the entirely different molecular sequence leading to the differences in physical mechanical behaviors with the single clay mineral (Gaucher et al., 2004; Robinet et al., 2015; Sakharov and Lanson, 2013; Song et al., 2017; Weaver, 1955; Zhang et al., 2021a). However, there has been limited researches focused on the physical mechanical properties of clay with mixed-layers. Therefor, we will firstly build the reasonable atomic structure of illite-montmorillonite in varied proportions. Afterwards, the mechanical test will be performed to explore the strength and deformation features influenced by dif-

ferent conditions like water content, temperature, loading path and so on. Finally and most important, the comparison of failure mechanism between mixed-layer and single-layer have to be analyzed deeply. This will provide us a nanoscale insight into macroscopic mechanical properties.

- Based on the research background of high-level radioactive waste disposal, the interface between two different geotechnical materials has to be pay attention as areas of weakness in mechanical properties. Actually, the clay–concrete interface is more complicated than host rock–concrete interfaces because of the water sensitivity of clay, with its potential interaction with concrete. Further, the swelling of clay is mainly caused by the typical clay mineral — montmorillonite. Therefore, Montmorillonite, the main component and origin of the interaction between clay and water from the formation or curing of concrete, is selected as our representative of clay. For concrete, which is the mixture of cement, water, fine and coarse aggregate. The hydration of cement is a complicated process creating complex micro-structures and the associated molecular structures that vary, the key cement mineral, Calcium-Silicate-Hydrate (CSH), is chosen as the representative of concrete. At last, the atomic structure of MMT and CSH will be combined together as our objective to explore the deformation and shear strength of the interface under various normal and shear stress levels. According to the introduction in our thesis, molecular dynamics simulation is successfully used to explore the interface property of clay based materials and explain the interaction mechanism at nanoscale (Chatterjee et al., 2021; Delville, 1993; Gao et al., 2018, 2019; Lai et al., 2018; Liu et al., 2020b; Wang et al., 2020, 2015b, 2014). However, to the best of our knowledge, the atomic-scale research of clay-concrete complex is rarely reported while the macro test has been performed by our team. It has been proven that the interface between clay and concrete is not the obvious weak zone of mechanical strength, which is extremely beneficial to the geological disposal (Liu et al., 2021). We expect to understand this surprising phenomenon at atomic scale.

Bibliography

Abedi, S., Slim, M., Hofmann, R., Bryndzia, T., and Ulm, F. (2016). Nanochemo-mechanical signature of organic-rich shales: a coupled indentation-edx analysis. *Acta Geotechnica*, 11:559–572.

Ansell, S., Barnes, A., Mason, P., Neilson, G., and Ramos, S. (2006). X-ray and neutron scattering studies of the hydration structure of alkali ions in concentrated aqueous solutions. *Biophysical chemistry*, 124(3):171–179.

Armand, G., Conil, N., Talandier, J., and Seyedi, D. M. (2017). Fundamental aspects of the hydromechanical behaviour of callovo-oxfordian claystone: from experimental studies to model calibration and validation. *Computers and Geotechnics*, 85:277–286.

Armand, G., Djizanne, H., Zghondi, J., de La Vaissière, R., Talandier, J., and Conil, N. (2016). Inputs from in situ experiments to the understanding of the unsaturated behaviour of callovo-oxfordian claystone. In *E3S Web of Conferences*, volume 9, page 03004. EDP Sciences.

Armand, G., Noiret, A., Zghondi, J., and Seyedi, D. (2013). Short-and long-term behaviors of drifts in the callovo-oxfordian claystone at the meuse/haute-marne underground research laboratory. *Journal of Rock Mechanics and Geotechnical Engineering*, 5(3):221–230.

Beeman, D. (1976). Some multistep methods for use in molecular dynamics calculations. *Journal of computational physics*, 20(2):130–139.

Bell, R., Jackson, R., and Catlow, C. (1992). Löwenstein's rule in zeolite a: A computational study. *Zeolites*, 12(7):870–871.

Belmokhtar, M., Delage, P., Ghabezloo, S., and Conil, N. (2017). Thermal volume changes and creep in the callovo-oxfordian claystone. *Rock Mechanics and Rock Engineering*, 50(9):2297–2309.

Bennett, K., Berla, L., Nix, W., and Borja, R. (2015). Instrumented nanoindentation and 3d mechanistic modeling of a shale at multiple scales. *Acta Geotechnica*, 10:1–14.

Berendsen, H., Grigera, J., and Straatsma, T. (1987). The missing term in effective pair potentials. *Journal of Physical Chemistry*, 91(24):6269–6271.

Boek, E., Coveney, P., and Skipper, N. (1995a). Monte carlo molecular modeling studies of hydrated li-, na-, and k-smectites: Understanding the role of potassium as a clay swelling inhibitor. *Journal of the American Chemical Society*, 117(50):12608–12617.

Boek, E. and Sprik, M. (2003). Ab initio molecular dynamics study of the hydration of a sodium smectite clay. *The Journal of Physical Chemistry B*, 107(14):3251–3256.

Boek, E. S., Coveney, P. V., and Skipper, N. T. (1995b). Molecular modeling of clay hydration, a study of hysteresis loops in the swelling curves of sodium montmorillonites. *Langmuir*, 11(12):4629–4631.

Bonini, M., Debernardi, D., Barla, M., and Barla, G. (2009). The mechanical behaviour of clay shales and implications on the design of tunnels. *Rock mechanics and rock engineering*, 42(2):361.

Born, M. and Von Kármán, T. (1967). *Über schwingungen in raumgittern*.

Bornert, M., Vales, F., Gharbi, H., and Nguyen, M. D. (2010). Multiscale full field strain measurements for micromechanical investigations of the hydromechanical behaviour of clayey rocks. *Strain*, 46:33–46.

Bossart, P., Jaeggi, D., and Nussbaum, C. (2017). Experiments on thermo-hydro-mechanical behaviour of opalinus clay at mont terri rock laboratory, switzerland. *Journal of Rock Mechanics and Geotechnical Engineering*, 9(3):502–510.

Bourg, I. C. and Sposito, G. (2010). Connecting the molecular scale to the continuum scale for diffusion processes in smectite-rich porous media. *Environmental science & technology*, 44(6):2085–2091.

Bourg, I. C. and Sposito, G. (2011). Molecular dynamics simulations of the electrical double layer on smectite surfaces contacting concentrated mixed electrolyte (nacl–cacl2) solutions. *Journal of colloid and interface science*, 360(2):701–715.

Braun, J., Stippich, C., and Glasmacher, U. A. (2016). The effect of variability in rock thermal conductivity on exhumation rate estimates from thermochronological data. *Tectonophysics*, 690:288–297.

Brochard, L., Honório, T., Vandamme, M., Bornert, M., and Peigney, M. (2017). Nanoscale origin of the thermo-mechanical behavior of clays. *Acta Geotechnica*, 12(6):1261–1279.

Carrier, B., Vandamme, M., Pellenq, R. J.-M., and Van Damme, H. (2014). Elastic properties of swelling clay particles at finite temperature upon hydration. *The Journal of Physical Chemistry C*, 118(17):8933–8943.

Chang, F.-R. C., Skipper, N., and Sposito, G. (1995). Computer simulation of interlayer molecular structure in sodium montmorillonite hydrates. *Langmuir*, 11(7):2734–2741.

Chatterjee, A., Dubey, D. K., and Sinha, S. K. (2021). Nanoscale friction and adhesion mechanisms in articular cartilage top layer hydrated interfaces: Insights from atomistic simulations. *Applied Surface Science*, 550:149216.

Chiarelli, A. S., Shao, J. F., and Hoteit, N. (2003). Modeling of elastoplastic dammage behavior of a claystone. *International Journal of Plasticity*, 19:23–45.

Chuanrui, W., Catherine, D., SKOCZYLAS, F., and TALANDIER, J. (2021). Effect of mineralogical composition and pore structure on the swelling of cox claystone. *Academic Journal of Civil Engineering*, 39(1):9–16.

Cui, S.-L., Zhang, H.-Y., and Zhang, M. (2012). Swelling characteristics of compacted gmz bentonite–sand mixtures as a buffer/backfill material in china. *Engineering Geology*, 141:65–73.

Cygan, R. T., Liang, J.-J., and Kalinichev, A. G. (2004). Molecular models of hydroxide, oxyhydroxide, and clay phases and the development of a general force field. *The Journal of Physical Chemistry B*, 108(4):1255–1266.

Delville, A. (1993). Structure and properties of confined liquids: a molecular model of the clay-water interface. *The Journal of Physical Chemistry*, 97(38):9703–9712.

Duque-Redondo, E., Manzano, H., Epelde-Elezcano, N., Martinez-Martinez, V., and Lopez-Arbeloa, I. (2014). Molecular forces governing shear and tensile failure in clay-dye hybrid materials. *Chemistry of Materials*, 26(15):4338–4345.

Ebrahimi, D., Pellenq, R. J.-M., and Whittle, A. J. (2012). Nanoscale elastic properties of montmorillonite upon water adsorption. *Langmuir*, 28(49):16855–16863.

Erbas, A., Horinek, D., and Netz, R. R. (2012). Viscous friction of hydrogen-bonded matter. *Journal of the American Chemical Society*, 134(1):623–630.

Espitia, J. and Caicedo, B. (2020). Mechanical behavior of unsaturated argillaceous rocks under uniaxial compression through acoustic emission. In *Unsaturated Soils: Research & Applications*, pages 1597–1603. CRC Press.

Espitia, J. M., Caicedo, B., and Vallejo, L. (2019). Comparison of the uniaxial compressive strength of the belencito claystone under stress control and suction control paths. *Rock Mechanics and Rock Engineering*, 52(1):19–34.

Fabre, G. and Pellet, F. (2006). Creep and time-dependent damage in argillaceous rocks. *International Journal of Rock Mechanics and Mining Sciences*, 43(6):950–960.

Faisal, H. N., Katti, K. S., and Katti, D. R. (2020). Molecular mechanics of the swelling clay tactoid under compression, tension and shear. *Applied Clay Science*, page 105908.

Faust, J. and Knittle, E. (1994). The equation of state, amorphization, and high-pressure phase diagram of muscovite. *Journal of Geophysical Research: Solid Earth*, 99(B10):19785–19792.

Ferrage, E., Lanson, B., Michot, L. J., and Robert, J.-L. (2010). Hydration properties and interlayer organization of water and ions in synthetic na-smectite with tetrahedral layer charge. part 1. results from x-ray diffraction profile modeling. *The Journal of Physical Chemistry C*, 114(10):4515–4526.

Frenkel, D. and Smit, B. (2001). *Understanding molecular simulation: from algorithms to applications*, volume 1. Elsevier.

Fu, M., Zhang, Z., Low, P., et al. (1990). Changes in the properties of a montmorillonite-water system during the adsorption and desorption of water: hysteresis. *Clays and Clay Minerals*, 38(5):485–492.

Gao, Y., Zhang, Y., Gu, F., Xu, T., and Wang, H. (2018). Impact of minerals and water on bitumen-mineral adhesion and debonding behaviours using molecular dynamics simulations. *Construction and Building Materials*, 171:214–222.

Gao, Y., Zhang, Y., Yang, Y., Zhang, J., and Gu, F. (2019). Molecular dynamics investigation of interfacial adhesion between oxidised bitumen and mineral surfaces. *Applied Surface Science*, 479:449–462.

Gasc-Barbier, M., Chanchole, S., and Bérest, P. (2004). Creep behavior of bure clayey rock. *Applied Clay Science*, 26(1-4):449–458.

Gaucher, E., Robelin, C., Matray, J., Negrel, G., Gros, Y., Heitz, J., Vinsot, A., Rebours, H., Cassagnabère, A., and Bouchet, A. (2004). Andra underground research laboratory:

interpretation of the mineralogical and geochemical data acquired in the callovian–oxfordian formation by investigative drilling. *Physics and Chemistry of the Earth, Parts A/B/C*, 29(1):55–77.

Gibbs, J. W. (1878). On the equilibrium of heterogeneous substances. *American Journal of Science*, 3(96):441–458.

Greathouse, J. and Cygan, R. (2013). Molecular simulation of clay minerals. In *Developments in Clay Science*, volume 5, pages 405–423. Elsevier.

Gutiérrez, G. G. (2010). *Oxydation of Clay Nanoreinforced Polyolefins*. PhD thesis, Arts et Métiers ParisTech.

Han, Z. (2020). *Molecular dynamics study on the micromechanical properties of clay minerals*. PhD thesis, China University of Mining and Technology, Beijing (China).

Hantal, G., Brochard, L., Laubie, H., Ebrahimi, D., Pellenq, R. J.-M., Ulm, F.-J., and Coasne, B. (2014). Atomic-scale modelling of elastic and failure properties of clays. *Molecular Physics*, 112(9-10):1294–1305.

Heino, P., Häkkinen, H., and Kaski, K. (1998). Molecular-dynamics study of mechanical properties of copper. *EPL (Europhysics Letters)*, 41(3):273.

Hoek, E. and Brown, E. T. (1997). Practical estimates of rock mass strength. *International journal of rock mechanics and mining sciences*, 34(8):1165–1186.

Hoek, E., Carranza-Torres, C., Corkum, B., et al. (2002). Hoek-brown failure criterion-2002 edition. *Proceedings of NARMS-Tac*, 1(1):267–273.

Hou, D., Ma, H., Zhu, Y., and Li, Z. (2014). Calcium silicate hydrate from dry to saturated state: Structure, dynamics and mechanical properties. *Acta materialia*, 67:81–94.

Hoxha, D., Giraud, A., Homand, F., and Auvray, C. (2007). Saturated and unsaturated behaviour modelling of meuse haute marne argillite. *International Journal of Plasticity*, 23:733–766.

Hu, D., Zhang, F., Shao, J.-F., and Gatmiri, B. (2014a). Influences of mineralogy and water content on the mechanical properties of argillite. *Rock mechanics and rock engineering*, 47(1):157–166.

Hu, D. W., Zhang, F., and Shao, J. F. (2014b). Experimental study of poromechanical behavior of saturated claystone under triaxial compression. *Acta Geotechnica*, 9(2):207–214.

Huang, Y., Xie, S., and Shao, J.-F. (2014). An experimental study of crack growth in claystones. *European journal of environmental and civil engineering*, 18(3):307–319.

Jiao, S. and Kulkarni, Y. (2015). Molecular dynamics study of creep mechanisms in nanotwinned metals. *Computational Materials Science*, 110:254–260.

Kalinichev, A. G., Wang, J., and Kirkpatrick, R. J. (2007). Molecular dynamics modeling of the structure, dynamics and energetics of mineral–water interfaces: Application to cement materials. *Cement and Concrete Research*, 37(3):337–347.

Karaborni, S., Smit, B., Heidug, W., Urai, J., and Van Oort, E. (1996). The swelling of clays: molecular simulations of the hydration of montmorillonite. *Science*, 271(5252):1102–1104.

Katahara, K. W. (1996). Clay mineral elastic properties. In *SEG Technical Program Expanded Abstracts 1996*, pages 1691–1694. Society of Exploration Geophysicists.

Koh, S. and Lee, H. (2006). Molecular dynamics simulation of size and strain rate dependent mechanical response of fcc metallic nanowires. *Nanotechnology*, 17(14):3451.

Lai, Z. B., Bai, R., Lei, Z., and Yan, C. (2018). Interfacial mechanical behaviour of protein–mineral nanocomposites: A molecular dynamics investigation. *Journal of biomechanics*, 73:161–167.

Lammers, L. N., Bourg, I. C., Okumura, M., Kolluri, K., Sposito, G., and Machida, M. (2017). Molecular dynamics simulations of cesium adsorption on illite nanoparticles. *Journal of colloid and interface science*, 490:608–620.

LeBaron, P. C., Wang, Z., and Pinnavaia, T. J. (1999). Polymer-layered silicate nanocomposites: an overview. *Applied clay science*, 15(1-2):11–29.

Lebon, P. and Mouroux, B. (1999). Knowledge of the three french underground laboratory sites. *Engineering Geology*, 52(3-4):251–256.

Lee, J. G. (2016). *Computational materials science: an introduction*. CRC press.

Leng, Y. and Cummings, P. T. (2005). Fluidity of hydration layers nanoconfined between mica surfaces. *Physical review letters*, 94(2):026101.

Leng, Y. and Cummings, P. T. (2006). Hydration structure of water confined between mica surfaces. *The Journal of chemical physics*, 124(7):074711.

Liu, B., Wang, J., Zhao, S., Qu, C., Liu, Y., Ma, L., Zhang, Z., Liu, K., Zheng, Q., and Ma, M. (2020a). Negative friction coefficient in microscale graphite/mica layered heterojunctions. *Science advances*, 6(16):eaaz6787.

Liu, H., Zhang, D., Li, M., Tong, L., and Feng, L. (2013). Competitive adsorption and transport of phthalate esters in the clay layer of jianghan plain, china. *Chemosphere*, 92(11):1542–1549.

Liu, K., Cheng, X., Ma, Y., Gao, X., Zhang, C., Li, Z., and Zhuang, J. (2020b). Analysis of interfacial nanostructure and interaction mechanisms between cellulose fibres and calcium silicate hydrates using experimental and molecular dynamics simulation data. *Applied Surface Science*, 506:144914.

Liu, Z. and Shao, J. (2016a). Moisture effects on damage and failure of bure claystone under compression. *Geotechnique letters*, 6(3):182–186.

Liu, Z. and Shao, J. (2017). Strength behavior, creep failure and permeability change of a tight marble under triaxial compression. *Rock Mechanics and Rock Engineering*, 50(3):529–541.

Liu, Z., Shao, J., Xie, S., and Conil, N. (2017). Triaxial creep induced gas permeability change and elastic modulus variation in callovo-oxfordian argillite. In *Poromechanics VI*, pages 1037–1044.

Liu, Z., Shao, J., Xie, S., Conil, N., and Zha, W. (2018a). Effects of relative humidity and mineral compositions on creep deformation and failure of a claystone under compression. *International Journal of Rock Mechanics and Mining Sciences*, 103:68–76.

Liu, Z., Shao, J., Zha, W., Xie, S., Bourbon, X., and Camps, G. (2021). Shear strength of interface between high-performance concrete and claystone in the context of a french radioactive waste repository project. *Géotechnique*, 71(6):534–547.

Liu, Z., Xie, S., Shao, J., and Conil, N. (2018b). Multi-step triaxial compressive creep behaviour and induced gas permeability change of clay-rich rock. *Géotechnique*, 68(4):281–289.

Liu, Z., Xie, S., Shao, J.-F., and Conil, N. (2015a). Effects of deviatoric stress and structural anisotropy on compressive creep behavior of a clayey rock. *Applied Clay Science*, 114:491–496.

Liu, Z. B. and Shao, J. F. (2016b). Moisture effects on damage and failure of claystone under compression. *Geotechnique Letters*, 6:1–5.

Liu, Z. B., Shao, J. F., Xie, S. Y., Conil, N., and Talandier, J. (2019a). Mechanical behavior of claystone in lateral decompression test and thermal effects. *Rock Mechanics and Rock Engineering*, 52:321–334.

Liu, Z. B., Shao, J Fand Xie, S. Y., Conil, N., and Talandier, J. (2019b). Mechanical behavior of claystone in lateral decompression test and thermal effect. *Rock Mechanics and Rock Engineering*, 52(2):321–334.

Liu, Z. B., Xie, S. Y., Shao, J. F., and Conil, N. (2015b). Effects of deviatoric stress and structural anisotropy on compressive creep behavior of a clayey rock. *Applied Clay Science*, 114:491–496.

Liu, Z. B., Xie, S. Y., Shao, J. F., and Conil, N. (2018c). Multi step triaxial compressive creep behaviour and induced gas permeability change of clay rich rock. *Geotechnique*, 68:281–289.

Liu, Z. B., Zhou, H. Y., Zhang, W., Xie, S. Y., and Shao, J. F. (2019c). A new experimental method for tensile property study of quartz sandstone under confining pressure. *International Journal of Rock Mechanics and Mining Sciences*, 123:104091.

Loewenstein, W. (1954). The distribution of aluminum in the tetrahedra of silicates and aluminates. *American Mineralogist: Journal of Earth and Planetary Materials*, 39(1-2):92–96.

Malikova, N., Dubois, E., Marry, V., Rotenberg, B., and Turq, P. (2010). Dynamics in clays-combining neutron scattering and microscopic simulation. *Zeitschrift für Physikalische Chemie*, 224(1-2):153–181.

Manevitch, O. L. and Rutledge, G. C. (2004). Elastic properties of a single lamella of montmorillonite by molecular dynamics simulation. *The Journal of Physical Chemistry B*, 108(4):1428–1435.

Mazo, M. A., Manevitch, L. I., Gusarova, E. B., Berlin, A. A., Balabaev, N. K., and Rutledge, G. C. (2008a). Molecular dynamics simulation of thermomechanical properties

of montmorillonite crystal. ii. hydrated montmorillonite crystal. *The Journal of Physical Chemistry C*, 112(44):17056–17062.

Mazo, M. A., Manevitch, L. I., Gusarova, E. B., Shamaev, M. Y., Berlin, A. A., Balabaev, N. K., and Rutledge, G. C. (2008b). Molecular dynamics simulation of thermomechanical properties of montmorillonite crystal. 1. isolated clay nanoplate. *The Journal of Physical Chemistry B*, 112(10):2964–2969.

Medhekar, N. V., Ramasubramaniam, A., Ruoff, R. S., and Shenoy, V. B. (2010). Hydrogen bond networks in graphene oxide composite paper: structure and mechanical properties. *ACS nano*, 4(4):2300–2306.

Menaceur, H., Delage, P., Tang, A.-M., and Conil, N. (2015). The thermo-mechanical behaviour of the callovo-oxfordian claystone. *International Journal of Rock Mechanics and Mining Sciences*, 78:290–303.

Menaceur, H., Delage, P., Tang, A. M., and Conil, N. (2016). On the thermo-hydro-mechanical behaviour of a sheared callovo-oxfordian claystone sample with respect to the edz behaviour. *Rock Mechanics and Rock Engineering*, 49(5):1875–1888.

Meunier, A. (2005). *Clays*. Springer Science & Business Media.

Mignon, P., Ugliengo, P., Sodupe, M., and Hernandez, E. R. (2010). Ab initio molecular dynamics study of the hydration of li+, na+ and k+ in a montmorillonite model. influence of isomorphic substitution. *Physical Chemistry Chemical Physics*, 12(3):688–697.

Mohajerani, M., Delage, P., Sulem, J., Monfared, M., Tang, A. M., and Gatmiri, B. (2012). A laboratory investigation of thermally induced pore pressures in the callovo-oxfordian claystone. *International Journal of Rock Mechanics and Mining Sciences*, 52:112–121.

Monfared, M., Sulem, J., Delage, P., and Mohajerani, M. (2011). A laboratory investigation on thermal properties of the opalinus claystone. *Rock Mechanics and Rock Engineering*, 44(6):735.

Monfared, M., Sulem, J., Delage, P., and Mohajerani, M. (2014). Temperature and damage impact on the permeability of opalinus clay. *Rock mechanics and rock engineering*, 47(1):101–110.

Morodome, S. and Kawamura, K. (2009). Swelling behavior of na-and ca-montmorillonite up to 150 c by in situ x-ray diffraction experiments. *Clays and Clay Minerals*, 57(2):150–160.

Morshedifard, A., Masoumi, S., and Qomi, M. A. (2018). Nanoscale origins of creep in calcium silicate hydrates. *Nature communications*, 9(1):1–10.

Naumann, M., Hunsche, U., and Schulze, O. (2007). Experimental investigations on anisotropy in dilatancy, failure and creep of opalinus clay. *Physics and Chemistry of the Earth, Parts A/B/C*, 32(8-14):889–895.

Ni, H., Liu, J., Guo, J., Yang, D., and Chen, Y. (2020). Numerical modelling on water retention and permeability of compacted gmz bentonite under free-swelling conditions. *International Journal for Numerical and Analytical Methods in Geomechanics*, 44(12):1619–1633.

Niandou, H., Shao, J. F., Henry, J. P., and Fourmaintraux, D. (1997). Laboratory investigation of the mechanical behaviour of tournemire shale. *International Journal of Rock Mechanics and Mining Sciences*, 34:3–16.

Ohtaki, H. and Radnai, T. (1993). Structure and dynamics of hydrated ions. *Chemical reviews*, 93(3):1157–1204.

Peng-Fei, H., Yan-Hu, M., Wei, M., HUANG, Y.-T., and Jian-Hua, D. (2021). Testing and modeling of frozen clay–concrete interface behavior based on large-scale shear tests. *Advances in Climate Change Research*, 12(1):83–94.

Plimpton, S. (1993). Fast parallel algorithms for short-range molecular dynamics. Technical report, Sandia National Labs., Albuquerque, NM (United States).

Plimpton, S. (1995). Fast parallel algorithms for short-range molecular dynamics. *Journal of computational physics*, 117(1):1–19.

Porion, P., Michot, L. J., Faugère, A. M., and Delville, A. (2007). Structural and dynamical properties of the water molecules confined in dense clay sediments: a study combining 2h nmr spectroscopy and multiscale numerical modeling. *The Journal of Physical Chemistry C*, 111(14):5441–5453.

Rahromostaqim, M. and Sahimi, M. (2018). Molecular dynamics simulation of hydration and swelling of mixed-layer clays. *The Journal of Physical Chemistry C*, 122(26):14631–14639.

Ravina, I. and Low, P. F. (1972). Relation between swelling, water properties and b-dimension in montmorillonite-water systems. *Clays and Clay Minerals*, 20(3):109–123.

Raviv, U. and Klein, J. (2002). Fluidity of bound hydration layers. *Science*, 297(5586):1540–1543.

Robinet, J., Sardini, P., Siitari-Kauppi, M., Prêt, D., and Yven, B. (2015). Upscaling the porosity of the callovo-oxfordian mudstone from the pore scale to the formation scale; insights from the 3h-pmma autoradiography technique and sem bse imaging. *Sedimentary Geology*, 321:1–10.

Robinet, J.-C. (2008). *Minéralogie, porosité et diffusion des solutés dans l'argilite du Callovo-Oxfordien de Bure (Meuse, Haute-Marne, France) de l'échelle centimétrique à micrométrique*. PhD thesis, Poitiers.

Robinet, J. C., Sardini, P., Coelho, D., Parneix, J. C., Pret, D., Sammartino, S., Boller, E., and Altmann, S. (2012). Effects of mineral distribution at mesoscopic scale on solute diffusion in a clay-rich rock: Example of the callovo-oxfordian mudstone (bure, france). *Water resources research*, 48:W05554.

Rotenberg, B., Marry, V., Vuilleumier, R., Malikova, N., Simon, C., and Turq, P. (2007). Water and ions in clays: Unraveling the interlayer/micropore exchange using molecular dynamics. *Geochimica et Cosmochimica Acta*, 71(21):5089–5101.

Sakharov, B. and Lanson, B. (2013). X-ray identification of mixed-layer structures: modelling of diffraction effects. In *Developments in Clay Science*, volume 5, pages 51–135. Elsevier.

Sarout, J. and Guéguen, Y. (2008). Anisotropy of elastic wave velocities in deformed shales: Part 1—experimental results. *Geophysics*, 73(5):D75–D89.

Sarout, J., Molez, L., Guéguen, Y., and Hoteit, N. (2007). Shale dynamic properties and anisotropy under triaxial loading: Experimental and theoretical investigations. *Physics and Chemistry of the Earth, Parts A/B/C*, 32(8-14):896–906.

Sato, H., Ono, K., Johnston, C. T., and Yamagishi, A. (2005). First-principles studies on the elastic constants of a 1: 1 layered kaolinite mineral. *American Mineralogist*, 90(11-12):1824–1826.

Schmidt, S. R., Katti, D. R., Ghosh, P., and Katti, K. S. (2005). Evolution of mechanical response of sodium montmorillonite interlayer with increasing hydration by molecular dynamics. *Langmuir*, 21(17):8069–8076.

Scholtzová, E. and Tunega, D. (2020). Prediction of mechanical properties of grafted kaolinite–a dft study. *Applied Clay Science*, 193:105692.

Schramm, L. L. and Kwak, J. C. (1982). Influence of exchangeable cation composition on the size and shape of montmorillonite particles in dilute suspension. *Clays and Clay Minerals*, 30(1):40–48.

Sellan, D. P., Landry, E. S., Turney, J., McGaughey, A. J., and Amon, C. H. (2010). Size effects in molecular dynamics thermal conductivity predictions. *Physical Review B*, 81(21):214305.

SEO, Y.-S., Ichikawa, Y., and Kawamura, K. (1999). Stress-strain response of rock-forming minerals by molecular dynamics simulation. *Journal of the Society of Materials Science, Japan*, 48(3Appendix):13–20.

Shao, J.-F., Jia, Y., Kondo, D., and Chiarelli, A.-S. (2006). A coupled elastoplastic damage model for semi-brittle materials and extension to unsaturated conditions. *Mechanics of materials*, 38(3):218–232.

Shen, W., Kondo, D., Dormieux, L., and Shao, J. (2013). A closed-form three scale model for ductile rocks with a plastically compressible porous matrix. *Mechanics of Materials*, 59:73–86.

Shen, W. and Shao, J.-F. (2015). A micromechanical model of inherently anisotropic rocks. *Computers and Geotechnics*, 65:73–79.

Shi, H., Hosdez, J., Rougelot, T., Xie, S., Shao, J., and Talandier, J. (2021). Influences of structural anisotropy and heterogeneity on three-dimensional strain fields and cracking patterns of a clay-rich rock. *Acta Geotechnica*, pages 1–13.

Shomer, I. and Mingelgrin, U. (1978). A direct procedure for determining the number of plates in tactoids of smectites. the na/ca-montmorillonite case. *CLAYS CLAY MINER. Clays Clay Miner.*, 26(2):135.

Shroll, R. M. and Smith, D. E. (1999). Molecular dynamics simulations in the grand canonical ensemble: Application to clay mineral swelling. *The Journal of chemical physics*, 111(19):9025–9033.

Song, Y., Davy, C. A., Bertier, P., Skoczylas, F., and Talandier, J. (2017). On the porosity of cox claystone by gas injection. *Microporous and Mesoporous Materials*, 239:272–286.

Sp r angberg, D. and Hermansson, K. (2004). Many-body potentials for aqueous li+, na+, mg 2+, and al 3+: comparison of effective three-body potentials and polarizable models. *The Journal of chemical physics*, 120(10):4829–4843.

Strauss, I., Chan, H., and Kral, P. (2014). Ultralong polarization chains induced by ions solvated in confined water monolayers. *Journal of the American Chemical Society*, 136(4):1170–1173.

Subramanian, N., Whittaker, M. L., Ophus, C., and Lammers, L. N. (2020). Structural implications of interfacial hydrogen bonding in hydrated wyoming-montmorillonite clay. *The Journal of Physical Chemistry C*, 124(16):8697–8705.

Suter, J. L., Coveney, P. V., Greenwell, H. C., and Thyveetil, M.-A. (2007). Large-scale molecular dynamics study of montmorillonite clay: emergence of undulatory fluctuations and determination of material properties. *The Journal of Physical Chemistry C*, 111(23):8248–8259.

Swope, W. C., Andersen, H. C., Berens, P. H., and Wilson, K. R. (1982). A computer simulation method for the calculation of equilibrium constants for the formation of physical clusters of molecules: Application to small water clusters. *The Journal of chemical physics*, 76(1):637–649.

Tambach, T. J., Bolhuis, P. G., Hensen, E. J., and Smit, B. (2006). Hysteresis in clay swelling induced by hydrogen bonding: accurate prediction of swelling states. *Langmuir*, 22(3):1223–1234.

Teich-McGoldrick, S. L., Greathouse, J. A., and Cygan, R. T. (2012). Molecular dynamics simulations of structural and mechanical properties of muscovite: Pressure and temperature effects. *The Journal of Physical Chemistry C*, 116(28):15099–15107.

Teich-McGoldrick, S. L., Greathouse, J. A., Jove-Colon, C. F., and Cygan, R. T. (2015). Swelling properties of montmorillonite and beidellite clay minerals from molecular simulation: comparison of temperature, interlayer cation, and charge location effects. *The Journal of Physical Chemistry C*, 119(36):20880–20891.

Thapa, K. B., Katti, K. S., and Katti, D. R. (2020). Compression of na–montmorillonite swelling clay interlayer is influenced by fluid polarity: A steered molecular dynamics study. *Langmuir*, 36(40):11742–11753.

Tian, H., Ziegler, M., and Kempka, T. (2014). Physical and mechanical behavior of claystone exposed to temperatures up to 1000 c. *International Journal of Rock Mechanics and Mining Sciences*, 70:144–153.

Tongraar, A., Liedl, K. R., and Rode, B. M. (1998). Born- oppenheimer ab initio qm/mm dynamics simulations of na+ and k+ in water: From structure making to structure breaking effects. *The Journal of Physical Chemistry A*, 102(50):10340–10347.

Tournassat, C., Bourg, I. C., Steefel, C. I., and Bergaya, F. (2015). Surface properties of clay minerals. In *Developments in clay science*, volume 6, pages 5–31. Elsevier.

Tournassat, C., Chapron, Y., Leroy, P., Bizi, M., and Boulahya, F. (2009). Comparison of molecular dynamics simulations with triple layer and modified gouy–chapman models in a 0.1 m nacl–montmorillonite system. *Journal of Colloid and Interface Science*, 339(2):533–541.

Tuckerman, M., Berne, B. J., and Martyna, G. J. (1992). Reversible multiple time scale molecular dynamics. *The Journal of chemical physics*, 97(3):1990–2001.

Tunega, D. and Zaoui, A. (2020). Mechanical and bonding behaviors behind the bending mechanism of kaolinite clay layers. *The Journal of Physical Chemistry C*, 124(13):7432–7440.

Underwood, T. R. and Bourg, I. C. (2020). Large-scale molecular dynamics simulation of the dehydration of a suspension of smectite clay nanoparticles. *The Journal of Physical Chemistry C*, 124(6):3702–3714.

Vales, F., Berest, P., and Gharbi, H. (2002). Interaction between creep, swelling and pressure-solution during indentation tests.

Vales, F., Nguyen, M. D., Hakim, G., and Rejeb, A. (2004). Experimental study of the influence of the degree of saturation on physical and mechanical properties in tournemire shale (france). *Applied Clay Science*, 26(1-4):197–207.

Van Gunsteren, W. F. and Berendsen, H. J. (1988). A leap-frog algorithm for stochastic dynamics. *Molecular Simulation*, 1(3):173–185.

Vanorio, T., Prasad, M., and Nur, A. (2003). Elastic properties of dry clay mineral aggregates, suspensions and sandstones. *Geophysical Journal International*, 155(1):319–326.

Vasconcelos, I. F., Bunker, B. A., and Cygan, R. T. (2007). Molecular dynamics modeling of ion adsorption to the basal surfaces of kaolinite. *The Journal of Physical Chemistry C*, 111(18):6753–6762.

Verlet, L. (1967). Computer" experiments" on classical fluids. i. thermodynamical properties of lennard-jones molecules. *Physical review*, 159(1):98.

Wang, J., Kalinichev, A. G., and Kirkpatrick, R. J. (2005). Structure and decompression melting of a novel, high-pressure nanoconfined 2-d ice. *The Journal of Physical Chemistry B*, 109(30):14308–14313.

Wang, L. L., Bornert, M., Heripre, E., Chanchole, S., Pouya, A., and Halphen, B. (2015a). The mechanisms of deformation and damage of mudstones: a micro-scale study combining esem and dic. *Rock Mechanics and Rock Engineering*, 48:1913–1926.

Wang, P., Qiao, G., Guo, Y., Zhang, Y., Hou, D., Jin, Z., Zhang, J., Wang, M., and Hu, X. (2020). Molecular dynamics simulation of the interfacial bonding properties between graphene oxide and calcium silicate hydrate. *Construction and Building Materials*, 260:119927.

Wang, Y., Wohlert, J., Bergenstrahle-Wohlert, M., Kochumalayil, J. J., Berglund, L. A., Tu, Y., and r Agren, H. (2015b). Molecular adhesion at clay nanocomposite interfaces depends on counterion hydration–molecular dynamics simulation of montmorillonite/xyloglucan. *Biomacromolecules*, 16(1):257–265.

Wang, Y., Wohlert, J., Berglund, L. A., Tu, Y., and r Agren, H. (2014). Molecular dynamics simulation of strong interaction mechanisms at wet interfaces in clay–polysaccharide nanocomposites. *Journal of Materials Chemistry A*, 2(25):9541–9547.

Wang, Z., Wang, H., and Cates, M. E. (2001). Effective elastic properties of solid clays. *Geophysics*, 66(2):428–440.

Weaver, C. E. (1955). The distribution and identification of mixed-layer clays in sedimentary rocks1. *Clays and Clay Minerals*, 4(1):385–386.

Weck, P. F., Kim, E., and Jove-Colon, C. F. (2015). Relationship between crystal structure and thermo-mechanical properties of kaolinite clay: beyond standard density functional theory. *Dalton Transactions*, 44(28):12550–12560.

Wei, P.-C., Zhang, L.-L., Zheng, Y.-Y., Diao, Q.-F., Zhuang, D.-Y., and Yin, Z.-Y. (2021). Nanoscale friction characteristics of hydrated montmorillonites using molecular dynamics. *Applied Clay Science*, 210:106155.

Wileveau, Y. and Bernier, F. (2008). Similarities in the hydromechanical response of callovo-oxfordian clay and boom clay during gallery excavation. *Physics and Chemistry of the Earth, Parts A/B/C*, 33:S343–S349.

Willemsen, J. A. and Bourg, I. C. (2021). Molecular dynamics simulation of the adsorption of per-and polyfluoroalkyl substances (pfass) on smectite clay. *Journal of Colloid and Interface Science*, 585:337–346.

Willemsen, J. A., Myneni, S. C., and Bourg, I. C. (2019). Molecular dynamics simulations of the adsorption of phthalate esters on smectite clay surfaces. *The Journal of Physical Chemistry C*, 123(22):13624–13636.

Wong, T.-f., David, C., and Zhu, W. (1997). The transition from brittle faulting to cataclastic flow in porous sandstones: Mechanical deformation. *Journal of Geophysical Research: Solid Earth*, 102(B2):3009–3025.

Wu, T. and Firoozabadi, A. (2020). Mechanical properties and failure envelope of kerogen matrix by molecular dynamics simulations. *The Journal of Physical Chemistry C*.

Yang, D., Bornert, M., Chanchole, S., Wang, L., Valli, P., and Gatmiri, B. (2011). Experimental investigation of the delayed behavior of unsaturated argillaceous rocks by means of digital image correlation techniques. *Applied clay science*, 54(1):53–62.

Yang, D., Chanchole, S., Valli, P., and Chen, L. (2013a). Study of the anisotropic properties of argillite under moisture and mechanical loads. *Rock mechanics and rock engineering*, 46(2):247–257.

Yang, F., Wang, M., and Wang, Z. (2013b). Sorption behavior of 17 phthalic acid esters on three soils: effects of ph and dissolved organic matter, sorption coefficient measurement and qspr study. *Chemosphere*, 93(1):82–89.

Yang, G., Neretnieks, I., and Holmboe, M. (2017). Atomistic simulations of cation hydration in sodium and calcium montmorillonite nanopores. *The Journal of chemical physics*, 147(8):084705.

Yang, H., He, M., Lu, C., and Gong, W. (2019). Deformation and failure processes of kaolinite under tension: Insights from molecular dynamics simulations. *SCIENCE CHINA Physics, Mechanics & Astronomy*, 62(6):64612.

Yeh, I.-C. and Hummer, G. (2004). System-size dependence of diffusion coefficients and viscosities from molecular dynamics simulations with periodic boundary conditions. *The Journal of Physical Chemistry B*, 108(40):15873–15879.

Yu, L., Weetjens, E., Sillen, X., Vietor, T., Li, X., Delage, P., Labiouse, V., and Charlier, R. (2014). Consequences of the thermal transient on the evolution of the damaged zone around a repository for heat-emitting high-level radioactive waste in a clay formation: a performance assessment perspective. *Rock mechanics and rock engineering*, 47(1):3–19.

Yue, D.-C., Ma, T.-B., Hu, Y.-Z., Yeon, J., van Duin, A. C., Wang, H., and Luo, J. (2013). Tribochemistry of phosphoric acid sheared between quartz surfaces: A reactive molecular dynamics study. *The Journal of Physical Chemistry C*, 117(48):25604–25614.

Zartman, G. D., Liu, H., Akdim, B., Pachter, R., and Heinz, H. (2010). Nanoscale tensile, shear, and failure properties of layered silicates as a function of cation density and stress. *The Journal of Physical Chemistry C*, 114(4):1763–1772.

Zeng, Z. X., Cui, Y. J., Zhang, F., Conil, N., and Talandier, J. (2019). Investigation of swelling pressure of bentonite/claystone mixture in the full range of bentonite fraction. *Applied Clay Science*, 178:105–137.

Zhang, C. and Rothfuchs, T. (2004). Experimental study of the hydro-mechanical behaviour of the callovo-oxfordian argillite. *Applied Clay Science*, 26(1-4):325–336.

Zhang, C.-L. (2018). Thermo-hydro-mechanical behavior of clay rock for deep geological disposal of high-level radioactive waste. *Journal of Rock Mechanics and Geotechnical Engineering*, 10(5):992–1008.

Zhang, C.-L., Armand, G., Conil, N., and Laurich, B. (2019). Investigation on anisotropy of mechanical properties of callovo-oxfordian claystone. *Engineering Geology*, 251:128–145.

Zhang, C.-L., Conil, N., and Armand, G. (2017). Thermal effects on clay rocks for deep disposal of high-level radioactive waste. *Journal of Rock Mechanics and Geotechnical Engineering*, 9(3):463–478.

Zhang, C.-L. and Laurich, B. (2020). Mechanical behavior of sandy facies of opalinus clay under different load conditions. *Journal of Rock Mechanics and Geotechnical Engineering*, 12(2):223–241.

Zhang, C.-L., Rothfuchs, T., and Su, K. (2013). Laboratory experiments on thermal effects on clay rocks. In *Thermo-Hydromechanical and Chemical Coupling in Geomaterials and Applications: Proceedings of the 3rd International Symposium GeoProc'2008*, pages 239–249. Wiley Online Library.

Zhang, C.-L., Rothfuchs, T., Su, K., and Hoteit, N. (2007). Experimental study of the thermo-hydro-mechanical behaviour of indurated clays. *Physics and Chemistry of the Earth, Parts A/B/C*, 32(8-14):957–965.

Zhang, F., Cui, Y.-J., Conil, N., and Talandier, J. (2021a). Effect of fracture voids on the swelling behaviour of callovo-oxfordian claystone. *Engineering Geology*, 280:105935.

Zhang, F., Guo, H., Hu, D., and Shao, J.-F. (2018). Characterization of the mechanical properties of a claystone by nano-indentation and homogenization. *Acta Geotechnica*, 13(6):1395–1404.

Zhang, F., Hu, D., Xie, S., and Shao, J.-F. (2014a). Influences of temperature and water content on mechanical property of argillite. *European journal of environmental and civil engineering*, 18(2):173–189.

Zhang, F., Xie, S. Y., Hu, D. W., Shao, J. F., and Gatmiri, B. (2012). Effect of water content and structural anisotropy on mechanical property of claystone. *Applied Clay Science*, 69:79–86.

Zhang, L., Lu, X., Liu, X., Zhou, J., and Zhou, H. (2014b). Hydration and mobility of interlayer ions of (na x, ca y)-montmorillonite: a molecular dynamics study. *The Journal of Physical Chemistry C*, 118(51):29811–29821.

Zhang, L.-L., Zheng, Y.-Y., Wei, P.-C., Diao, Q.-F., and Yin, Z.-Y. (2021b). Nanoscale mechanical behavior of kaolinite under uniaxial strain conditions. *Applied Clay Science*, 201:105961.

Zhang, W., Hu, H., Li, X., and Fang, Z. (2015). Interplay of montmorillonite–h2o–scco2 system between mechanical behavior and adsorption: molecular dynamics. *The Journal of Physical Chemistry C*, 119(38):21959–21968.

Zhao, J., Qin, X., Wang, J., and He, M. (2020). Effect of mg (ii) and na (i) doping on the electronic structure and mechanical properties of kaolinite. *Minerals*, 10(4):368.

Zhao, X.-K., Yang, G.-P., and Wang, Y.-J. (2004). Adsorption of dimethyl phthalate on marine sediments. *Water, air, and soil pollution*, 157(1):179–192.

Zheng, Y. (2009). *Modélisation et simulation à l'échelle nanométrique de l'effet de température, de pression et des polluants sur l'argile hydratée de type montmorillonite.* PhD thesis, INSA de Rennes (France.

Zhu, L., Shen, W., Shao, J., and He, M. (2021). Insight of molecular simulation to better assess deformation and failure of clay-rich rocks in compression and extension. *International Journal of Rock Mechanics and Mining Sciences*, 138:104589.